STUDIES OF NEUTRON INELASTIC SCATTERING

IN

CRYSTAL AND LIQUID SCINTILLATORS

BY

C.A.R. BAIN B.Sc. (Hons.)

SUPERVISOR : PROFESSOR F.D. BROOKS

A thesis submitted in partial fulfilment

of the requirements for the

Degree of Master of Science at the

University of Cape Town

MAY 1967.

ABSTRACT

An investigation has been made of the feasibility of using crystal, liquid and gel scintillators for the study of neutron inelastic scattering from elements, contained or loaded in the scintillators. The nuclides included those of iodine, cesium, lanthanum, holmium, praseodymium and bismuth. Investigations showed that the technique was feasible for crystal and liquid scintillators, and indicated the study of ^{127}I in sodium iodide crystal to be the most suitable for further investigation.

A study was then made of inelastic scattering to the 59 keV level of ^{127}I for incident neutrons in the energy range 60 to 360 keV. Cross section data obtained were compared with inelastic scattering cross sections calculated using a Hauser-Feshbach model of Auerbach and Moore. Experimental data were found to be in reasonable agreement with the calculated cross sections based on neutron transmission coefficients given by Auerbach and Perey.

1. INTRODUCTION

Neutron inelastic scattering is a useful tool for experiments in fields relating to nuclear spectroscopy (Cr63a) and nuclear reaction theory. The neutron being uncharged its reactions are not complicated by Coulomb field interactions. Because of this, relatively low energy neutrons can be used to study the structure of nuclei and the part played by the compound nucleus in inelastic scattering. Reaction modes can be studied by comparing angular distributions and excitation functions with theoretical predictions, such as those of Hauser and Feshbach (Ha52) and Satchler (Sa56).

The study of neutron inelastic scattering is also of great practical importance particularly in the field of reactor physics.

Methods of measuring neutron inelastic scattering cross sections include,

1) Observation of scattered neutrons as a function of energy and angle
2) Observation of de-excitation gamma rays, internal conversion electrons etc. from levels populated by inelastic scattering.

Time-of-flight techniques have been employed in measurements by both of these general methods. (Kl59,Da63a)

The object of the research described in this thesis was to investigate and apply a specific technique for measuring neutron inelastic scattering cross sections. The technique consists of observing de-excitation radiations, in a scintillator, from

a nucleus which is a constituent of the scintillator (loaded scintillator method). It will readily be seen that such a technique may be particularly suitable for the study of nuclear levels which decay predominantly by internal conversion or by the emission of low energy ($\lesssim$ 100 keV) gamma-rays. Even a small (volume $\lesssim$ 5 ml) scintillator can be used to detect such de-excitation radiations with an efficiency $\gtrsim$ 80%. The use of a small scintillator (and hence also small target) has, in turn, a number of advantages, for example:

i) multiple neutron scattering, a well-known complication in a neutron inelastic scattering experiments (Se54, Su54), can be reduced to a tolerable level.

ii) the sensitivity to neutron and high energy gamma-ray backgrounds is kept small

iii) the efficiency for detecting inelastic scattering, being close to unity, can be determined accurately. This is particularly useful for absolute cross section measurements.

In common with other techniques which fall into category 2 this technique can in principle be used to study the inelastic cross section near to threshold. By virtue of advantage (ii) above, it would appear particularly suitable for such studies. The technique itself is not a new one, but has been used for example with sodium iodide scintillators, e.g. by Guernsey and Wattenburg (Gu56).

However the potential advantages of the tecnhique in the threshold region do not appear to have been fully exploited

either by this author or by others (Va56). A particular aim of the present work has been to press these advantages to their full extent. The steps to achieve this include the use of the time-of-flight method to further reduce backgrounds.

1.1 The Choice of Nuclides for Study.

An obvious limitation to the choice of a nuclide is whether it can be loaded into the scintillator or not. This is usually a chemical problem. In addition nuclei with a low lying level or a level with a high internal conversion coefficient (α) would be essential to make the most of the technique. The use of monoisotopic elements furthermore has the advantage that possible overlapping of different nuclear level spectra is avoided.

The choice eventually fell on the following readily available scintillators

1) Inorganic solids - thalluim activated Sodium Iodide and Cesium Iodide crystals (thin)
2) Liquids loaded with (i) Praseodymium
   (ii) Lanthanum
   (iii) Holmium

supplied by Nuclear Enterprises in $1\frac{1}{2}$" diameter × $\frac{1}{2}$" cells. In addition a third type of scintillation medium was chosen, namely a gel, wherein the nucleus of interest (in this case La)

was loaded in the form of a fine powder.

The sodium iodide crystal is particularly suitable; not only is it a good scintillator in itself but also the 59 keV level of ^{127}I fulfils the above requirements by being of low energy with a high internal conversion coefficient of 3.7 (Be65a,Si65). In fact the method proved quite a success with this crystal and a fuller investigation was carried out on the ^{127}I 59 keV level.

Cesium Iodide is also a good scintillator and the levels of cesium are low lying and have reasonably large values of α. Level schemes for ^{127}I and ^{132}Cs are shown in Figs. 1.1a and 1.1b respectively.

Although liquid scintillators have somewhat lower pulse height response than the solids above, the loaded elements have interesting level schemes and an investigation was therefore carried out using them. Both ^{141}Pr and ^{139}La have a low lying 1st level with the 2nd level well separated in energy, thus allowing the excitation function for the low lying level to be studied without complications, over a relatively large energy range. ^{165}Ho on the other hand has a number of low lying levels; with some interest being associated with the lifetimes of the states. Level diagrams for the above three nuclei are given in Figs. 1.2 a,b,c, respectively.

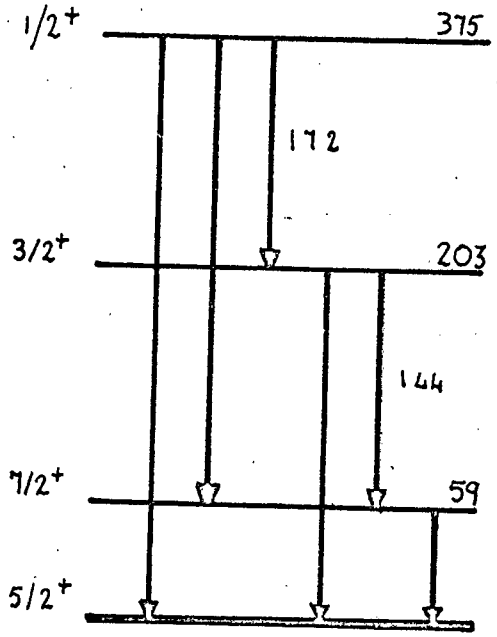

Fig 1·1 a) Stable $^{127}_{53}I_{74}$

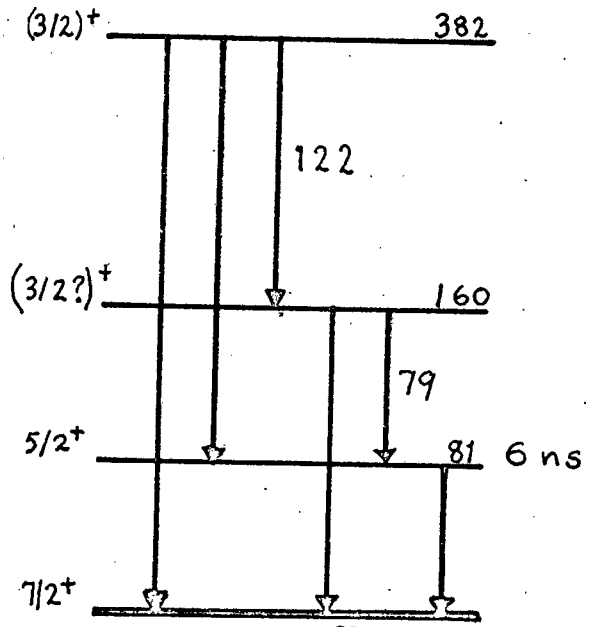

Fig 1·1 b) Stable $^{133}_{55}Cs_{78}$

Data from K. Way. Nuclear data sheets (Wa61)

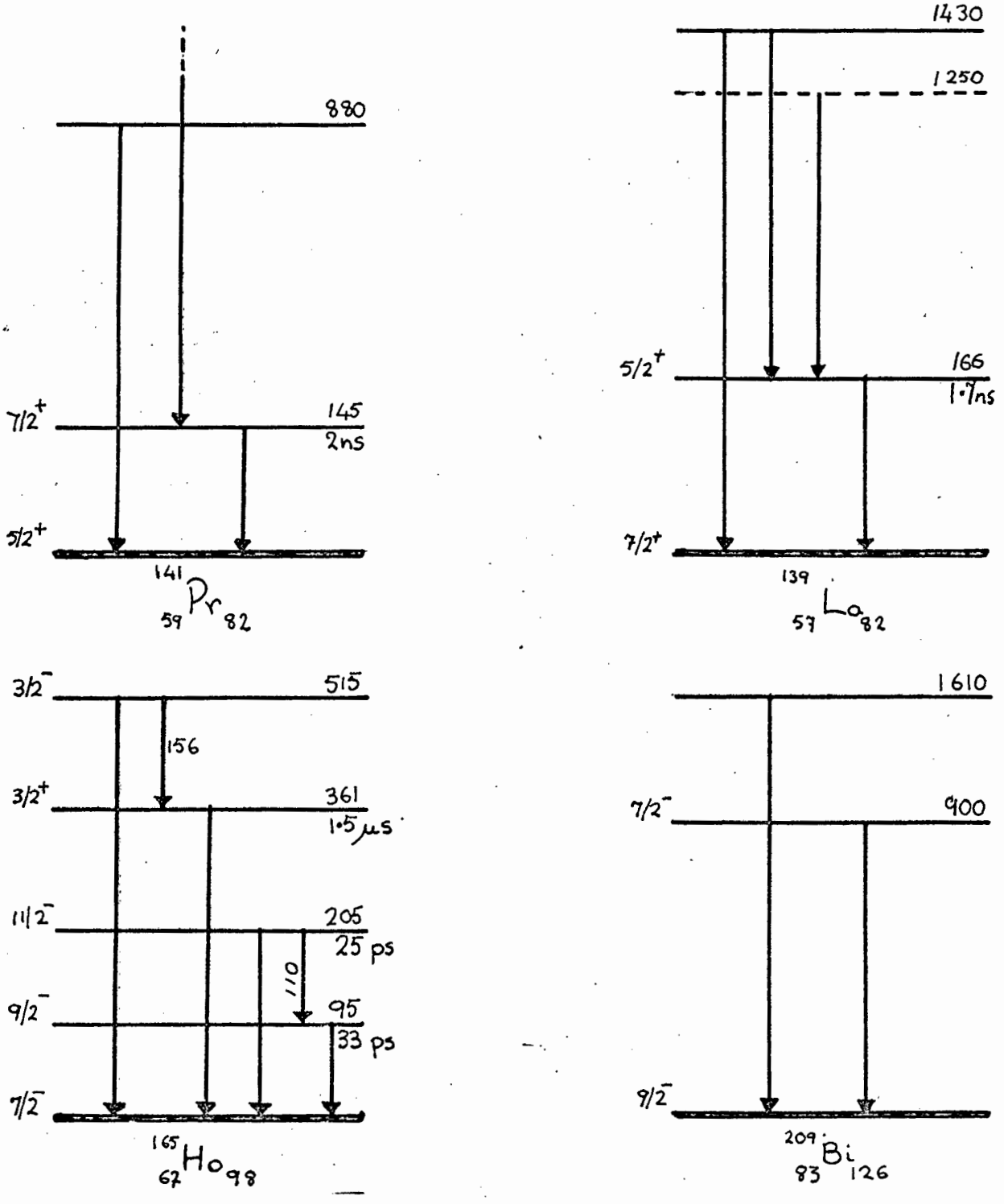

Fig 1·2 Level schemes for Pr, La, Ho and Bi (Wa 61)

1.2 Objects of Inelastic Scattering Studies

The object of doing such studies was firstly merely to obtain neutron inelastic scattering cross section data as a function of energy and secondly to interpret such data obtained. In principle various facts concerning the spins and parities of levels can be derived from such measurements when comparisons are made with theoretical predictions. Chief among these theories for inelastic scattering is that due to Hauser and Feshbach (Ha52) (subsequently referred to as HF theory). Excitation functions for various J^{π} values can be calculated; the one giving the best fit to experimental data indicates the spin parity value. A number of modifications exist to HF theory; notably that due to Moldauer (Mo61,63). Although the theories all yield similar curves for the excitation function there are some discrepancies between them, especially near threshold. (Da63b). Since the experimental method proposed here is particularly suited to measure values near threshold, it might be expected to lead to interesting and useful results.

We can therefore sum up the objects of the present research to be as follows:

1) to test the suitability of various scintillators (with loading) for the method outlined. It will be seen that these tests focussed attention on the sodium iodide crystal.
2) measurements of the neutron inelastic scattering cross section for the 59 keV level of ^{127}I.
3) comparison of the inelastic cross section data obtained with HF theory.

2. PRELIMINARY LOADED SCINTILLATOR INVESTIGATIONS.

2.1 Introduction

In this section we discuss experiments undertaken using loaded scintillators with the properties outlined in Chapter I. These preliminary investigations were carried out to determine which scintillator warranted further study of the loaded scintillator method for neutron inelastic scattering.

The source of neutrons was the $^{7}Li(p,n)$ reaction; (Gi59), the protons being provided by a 5.5 MeV Van de Graaff accelerator. The target was made by vacuum evaporation of lithium metal onto a tantalum backing. The thickness is dependent on the current used for heating and the length of evaporation time. To prevent oxidation the target was transported in an argon atmosphere to the accelerator flight line.

The variation of neutron energy with proton energy, with angle as a parameter, is shown in Fig. 2.1. In practice the finite thickness of the Li target introduces a spread in neutron energy. The threshold for the reaction is calibrated using a yield curve measured at 0° with a Long Counter Fig. 2.2. The thickness of the target may also be estimated from this yield curve. Gibbons et al. (Gi59) have shown that target thickness is approximately equal to the energy increment for a neutron flux increment from 10 to 90 percent of the maximum flux measured. For a given target thickness, ΔE_p, the average neutron energy $\bar{E}_n$ and its spread ΔE_n can therefore be expressed as a function of the proton beam energy, E_p, and θ

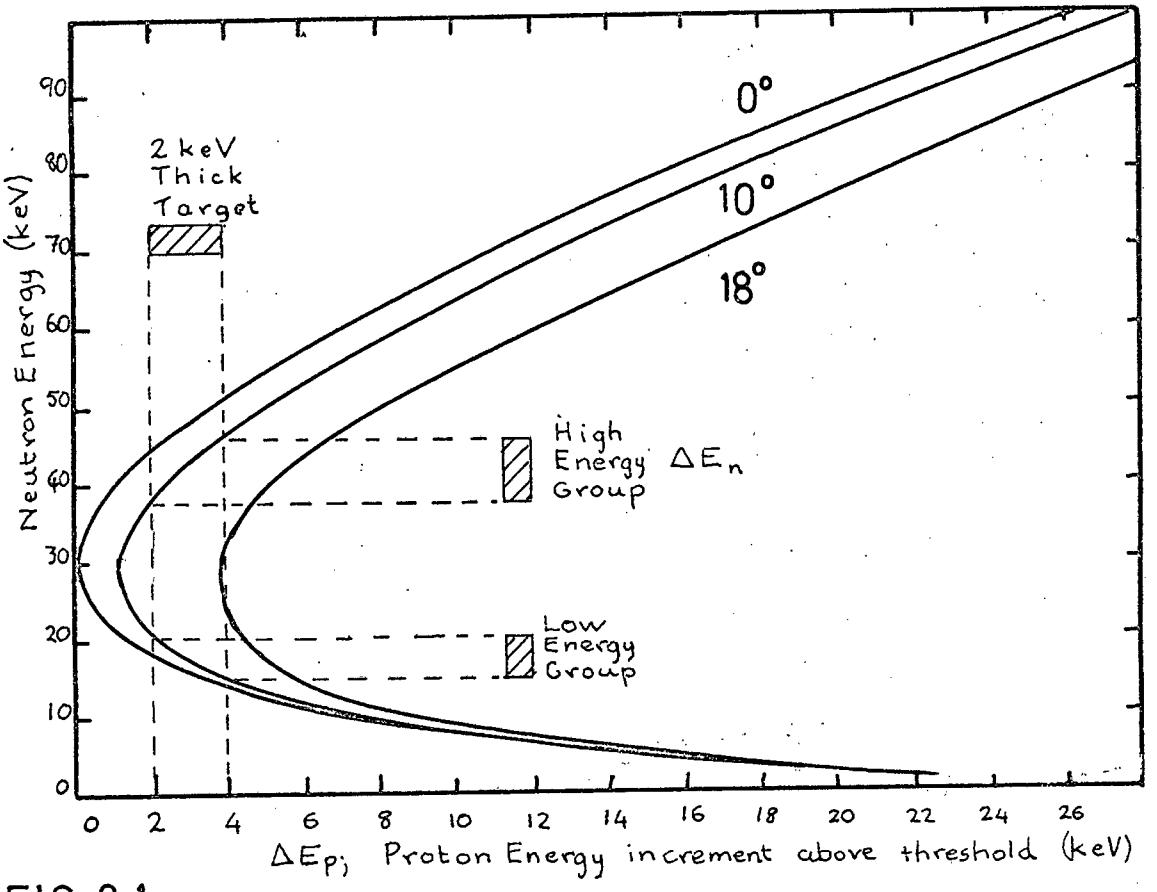

FIG 2·1 Neutron energy from a thin lithium target as a function of proton energy and angle of emission.

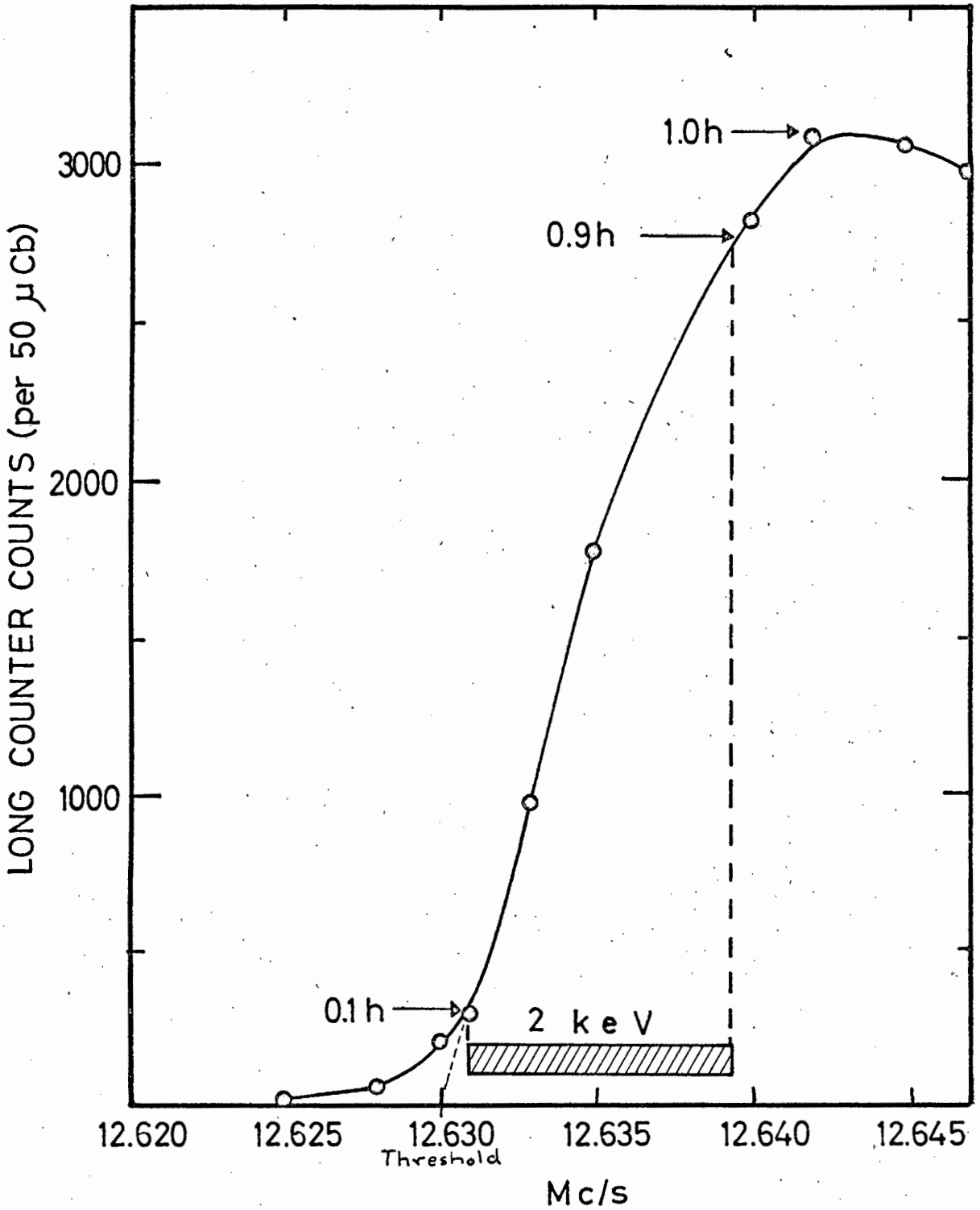

FIG 2·2 Neutron yield curve from Lithium target measured at 0°

the angle the detector makes with the proton beam direction and $\Delta\theta$ the experimental error in measuring θ. The spread in neutron energy ΔE_n can also be expressed as a function of the average neutron energy. This function is shown in Fig. 2.3 for a measurement at $10^\circ \pm 2^\circ$.

The time-of-flight method used in these experiments permits separation of neutrons from target gamma rays and other background effects and can also be used for the measurement of neutron energy. A block diagram of the time-of-flight system is shown in Fig. 2.4. The fast output pulse from the photomultiplier tube was fed via 200 Mc distributed amplifiers to a synchronising discriminator. The discriminator output was fed to the start input of a time-to-amplitude converter (T.A.C.). A typical time-of-flight spectrum obtained using a Lithium target of thickness approximately 2 keV is shown in Fig. 2.5. We define the timing resolution, Δt, as the full width at half maximum (F.W.H.M.) of the 'prompt' gamma peak. Δt is compounded from spreads introduced in beam pulsing and detector electronics.

The neutron flight time in nanoseconds is given by:

$$T = \frac{72.3D}{\sqrt{E_n}}$$

where: D is the flight path in meters.

E_n is the neutron energy in MeV.

The neutron energy resolution is determined by the uncertainties in the distance, ΔD, and time, Δt, measurements. In these

experiments the contribution of distance uncertainty (±1cm) was negligible for neutron energies exceeding one keV, hence the energy uncertainty was defined by the following equation

$$\frac{\Delta E_n}{E_n} = \frac{2v\Delta t}{D} \simeq \frac{2\Delta t}{t}$$

where v is the neutron velocity.

In Fig. 2.3 ΔE_n is plotted as a function of neutron energy E_n for a flight path of 0.22 m and Δt = 18 ns, these being the conditions used in some of the measurements described in Chapter 3. The figure also gives this function as calculated using target thickness and Fig. 2.1. In Fig. 2.3. it is seen that optimum energy resolution is obtained using thin targets.

2.2 Tests with Various Scintillators

We shall now describe investigations carried out using various scintillators. Scintillators studied were

i) Thallium activated Sodium Iodide and Cesium Iodide crystals,

ii) Holmium, Lanthanum Praseodymium and Bismuth Loaded liquid scintillators, and

iii) Lanthanum Chloride and Lanthanum oxide loaded Gel scintillators.

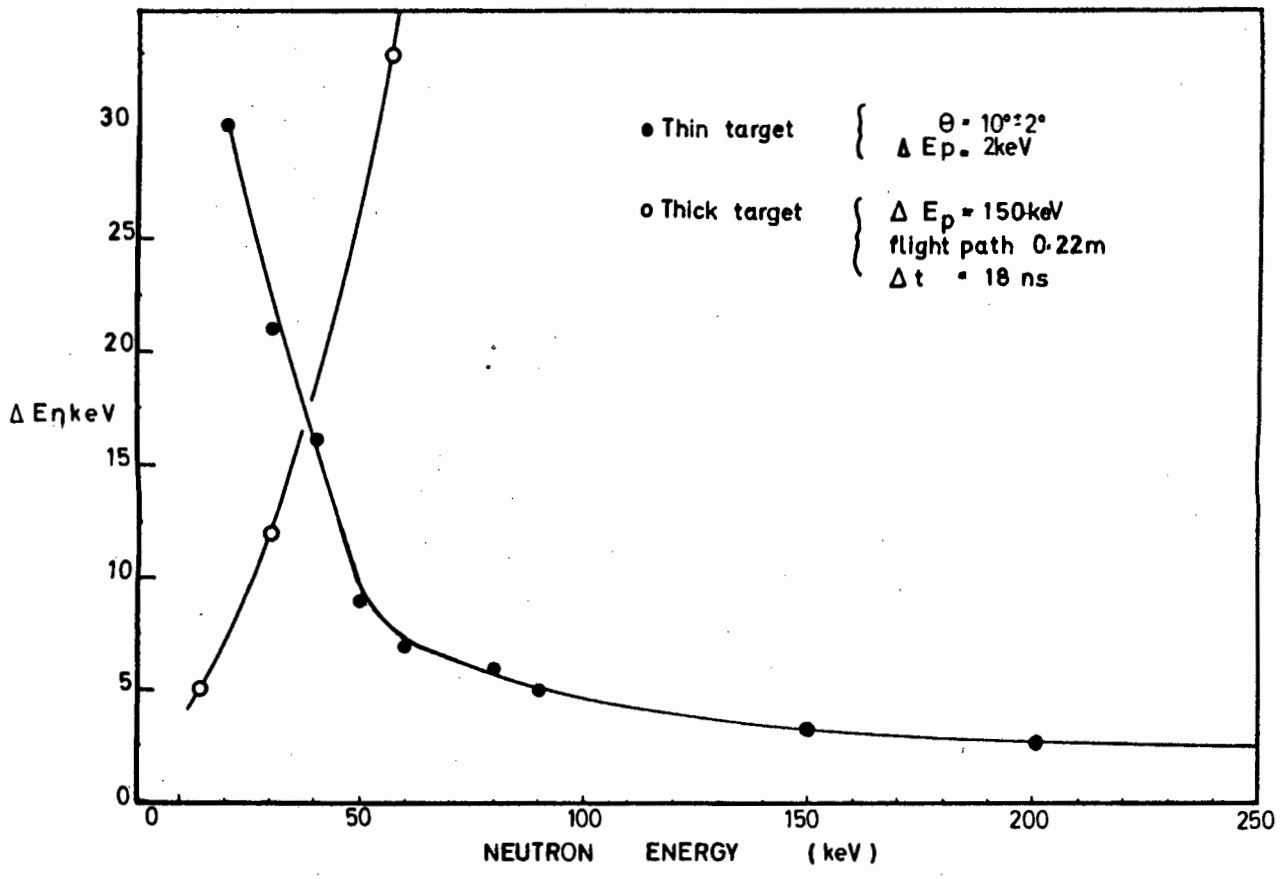

FIG 2·3 Variation of neutron energy resolution with neutron energy

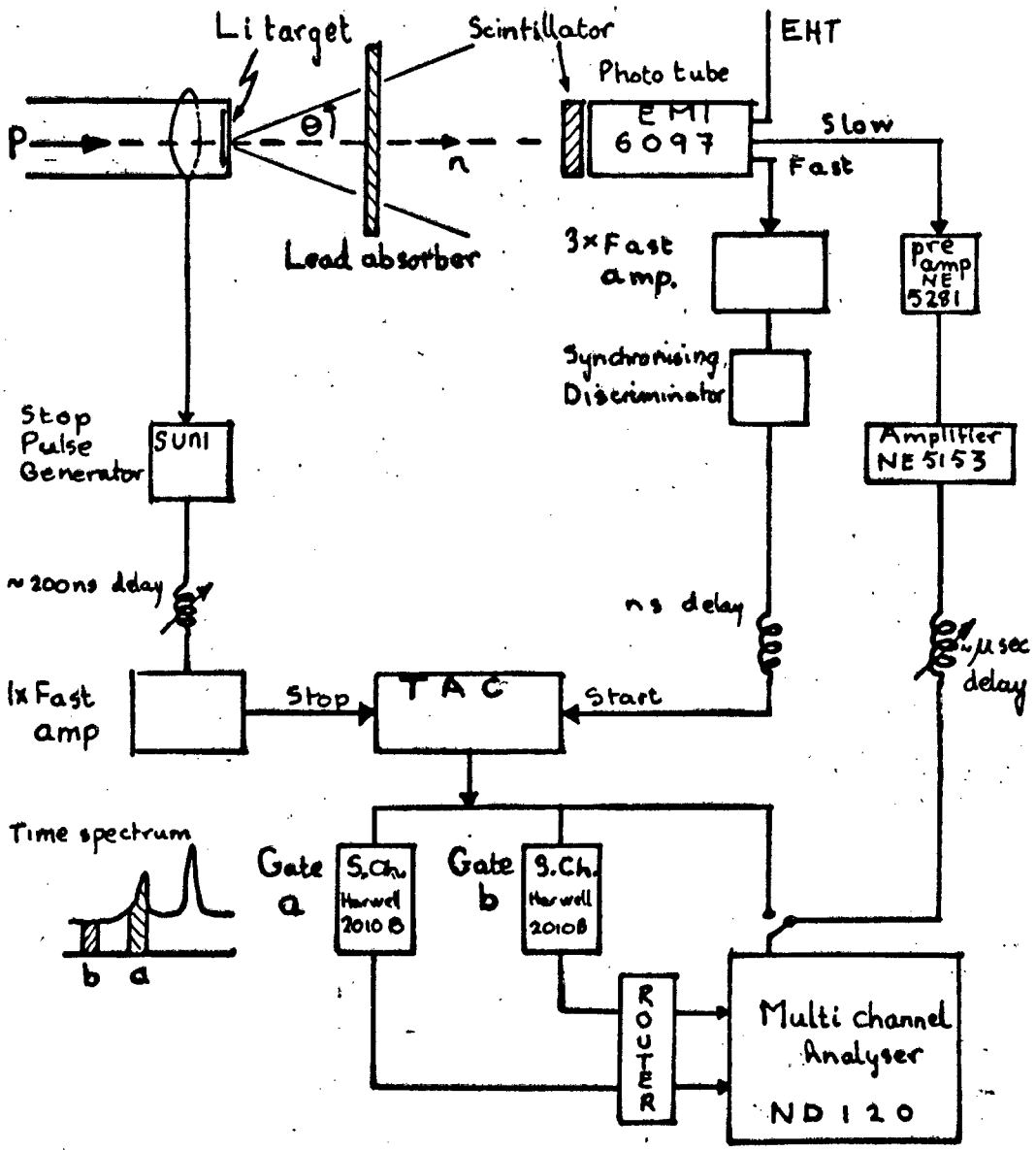

FIG 2·4·1 Block diagram of electronics used in preliminary investigations

2.2.1 Investigation using Sodium Iodide Crystal

The levels of interest in these studies were those of ^{127}I at 59 and 203 keV respectively. The NaI(Tℓ) crystal (31.8 mm diameter × 1.6 mm thick) was cut from "off-cuts" supplied by Nuclear Enterprises. The crystal was prepared following the procedure described by Bell (Be65b) and was sealed together with ∿ 2 gm P_2O_5 dessicant in an aluminium container. The pulse height response of this crystal to 60 keV gamma rays from an ^{241}Am source and 122 and 136 keV gammas (from ^{57}Co) is shown in Fig. 2.6. The pulse height resolution defined with respect to full width half maximum for the 60 keV peak was observed to be 32%.

In these initial tests the scintillator was placed at an angle of 0° to the proton beam direction, 30 cm from the Li target and was bombarded with a pulsed neutron beam. The time-of-flight spectrum obtained is shown in Fig. 2.5(a). Two timing gates were set; one so as to select for pulse height analysis only those pulses which correspond to the neutron time-of-flight between target and crystal; the other to select pulses corresponding to average background associated with the time spectrum. This is indicated in Fig. 2.5. The sodium iodide pulse height spectrum observed at different energies is shown in Fig. 2.7. As the neutron energy is increased above 59 keV a peak appears in the spectrum at a pulse height corresponding to an electron energy of 59 keV. This peak is

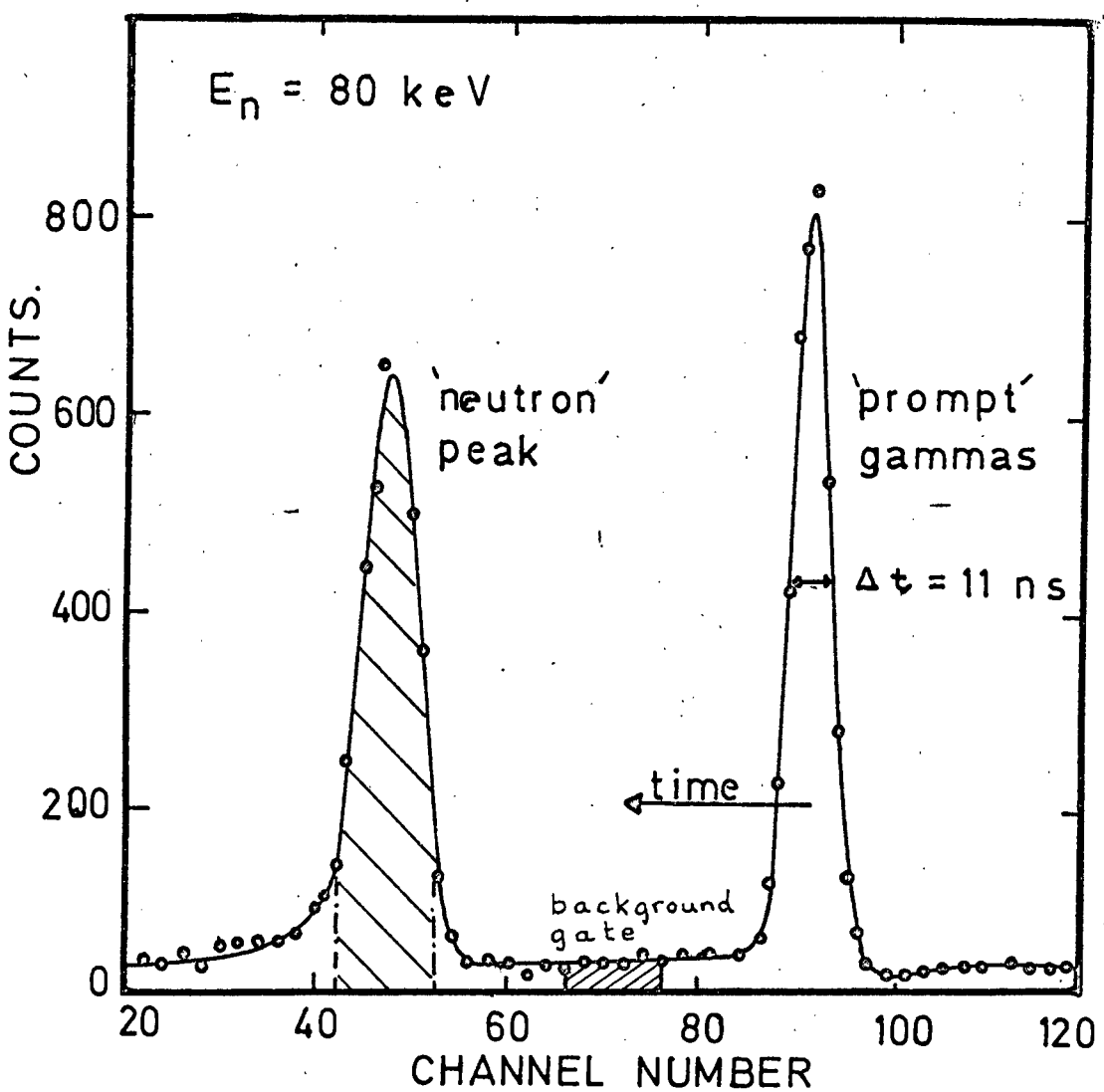

Fig. 2.5. Time Spectrum of NaI crystal using thin Li target (2.5 keV).

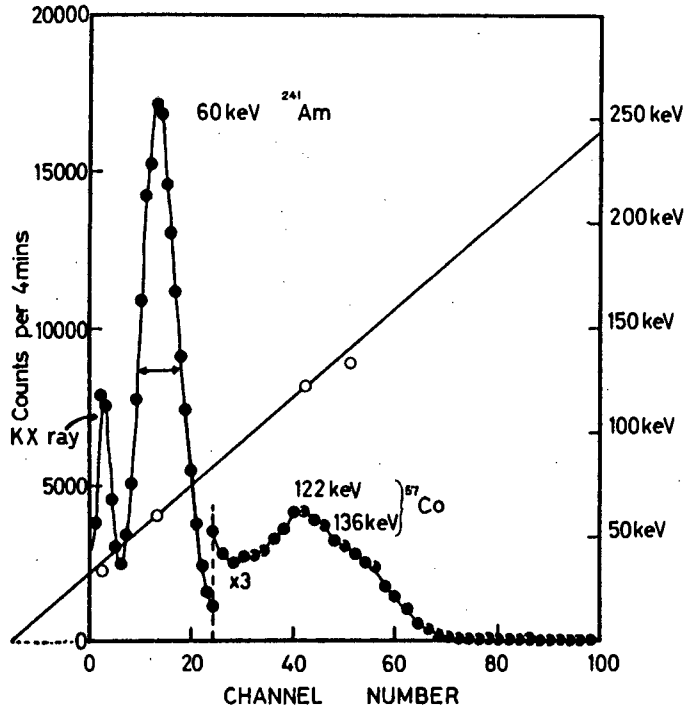

FIG 2·6 NaI pulse height spectrum showing energy calibration

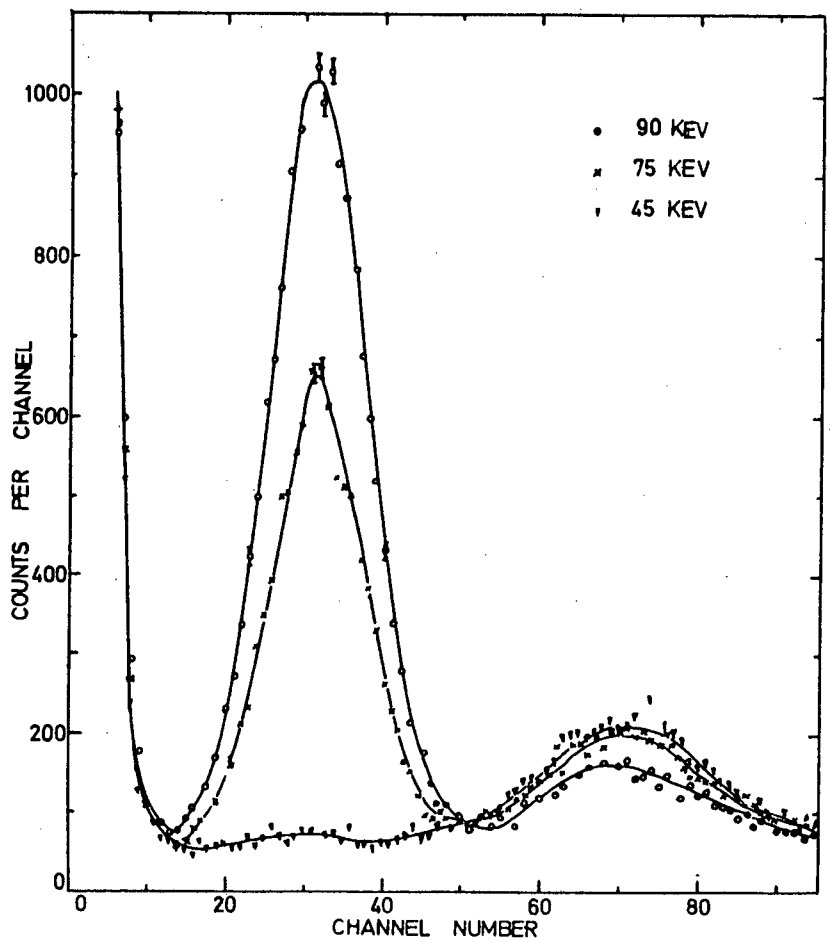

FIG 2·7 Pulse height spectra observed when a NaI crystal (38mm diam x 1·8mm) is bombarded by neutrons

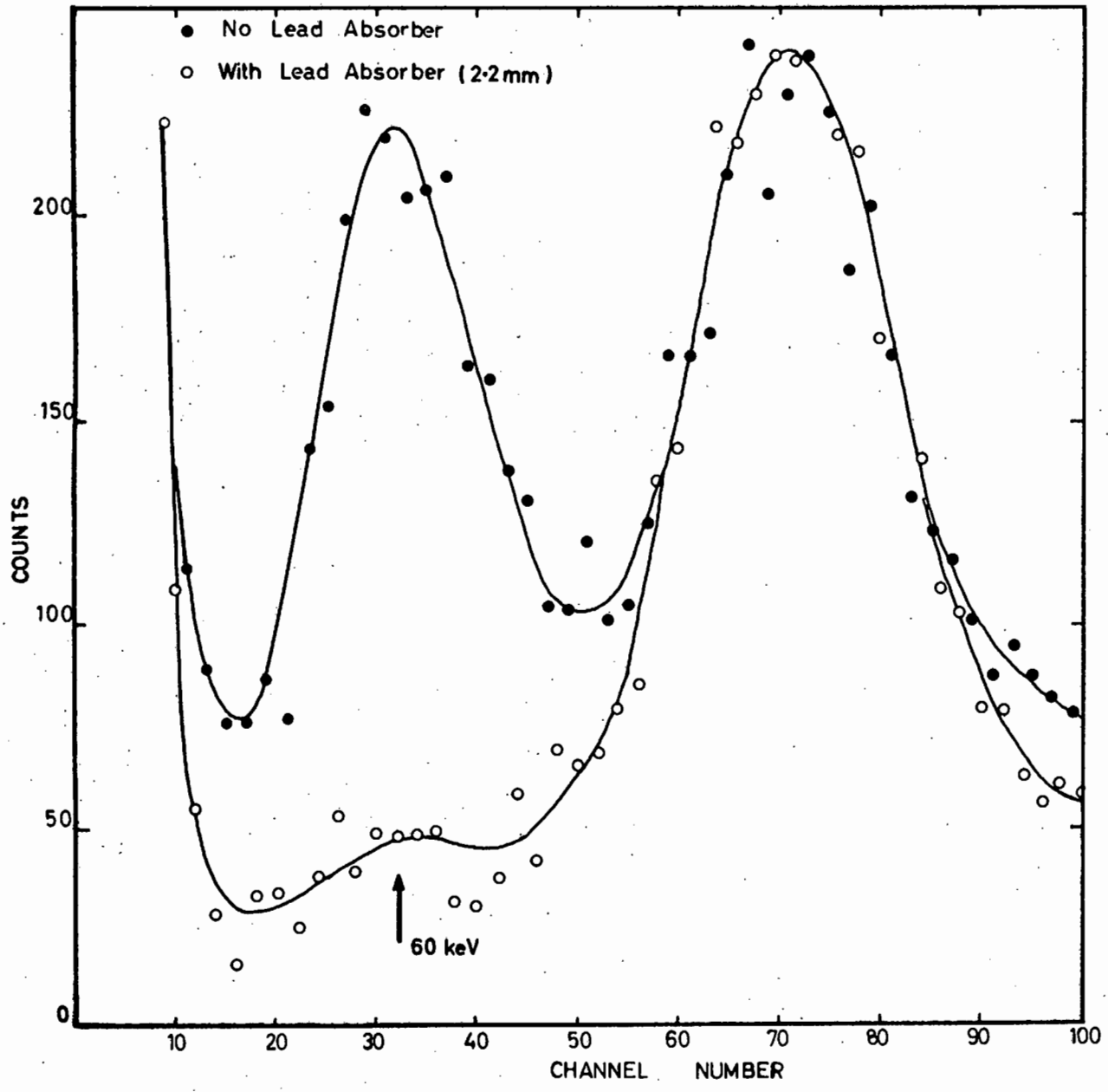

FIG 2·8 NaI pulse height spectrum showing effect of lead absorber on 60 keV radiation from tantalum backing

attributed to decay of the 59 keV state in ^{127}I following population of this state by inelastic neutron scattering. The area of the peak for a given neutron energy and flux is proportional to the cross section for the 59 keV level at that energy.

At this point we note the significance of the 2.2 mm thick lead shield between the target and detector. In early runs a strong beam dependent peak was observed at about 60 keV. The yield of this peak was about the same in both the background and neutron peak gate. The peak was also present when a tantalum blank was used. This suggested that the peak was due to 60 keV gamma or X-rays originating from activity built up in the tantalum by proton bombardment. The fact that the peak was due to such radiations was confirmed when a lead absorber placed between target and detector effectively removed the peak from the pulse height spectrum. Fig. 2.8. The 60 keV peaks observed in Fig. 2.7 can therefore confidently be attributed to de-excitation of the 59 keV state of ^{127}I following inelastic neutron scattering. Fig. 2.7 therefore clearly demonstrates the feasibility of the loaded scintillator method for the further study of this state.

A search was also made for de-excitation radiation from the 203 keV level of ^{127}I. In these tests the pulse height spectra obtained from neutron energies of 183 keV and 278 keV were compared. The decay of the 203 keV state might be expected to lead to peaks at 59, 144 and 203 keV in the pulse

height spectrum; the detection efficiency of the crystal being ∿20% for 144 keV gammas and ∿5% for 203 keV gamma rays respectively. Figures 2.9b and a show the spectra obtained at neutron energies E_n = 183 keV and E_n = 278 keV respectively. No evidence can be seen of photopeaks at 145 or 203 keV. The position might perhaps be improved if the background could be reduced or better statistical accuracy obtained.

We conclude therefore that tests on the sodium iodide crystal have shown that measurement of the 59 keV state could readily be made but that measurements for the 203 keV state do not confirm the method in this case.

2.2.2 Investigation of Cesium Iodide Crystal

The cesium levels at 81 and 160 keV are of particular interest for investigating this method. The Iodine levels at 59 and 203 keV might of course also be studied. A thallium activated cesium iodide crystal (25 mm diameter × 2 mm thickness) obtained from Nuclear Enterprises was used. The pulse height resolution defined with respect to the full width at half maximum for the 60 keV peak was observed to be 45% (Fig. 2.10). The time resolution using a similar system to that used for sodium iodide investigation was ∿30 nanoseconds. Fig. 2.11.

The experimental method employed for the investigation of

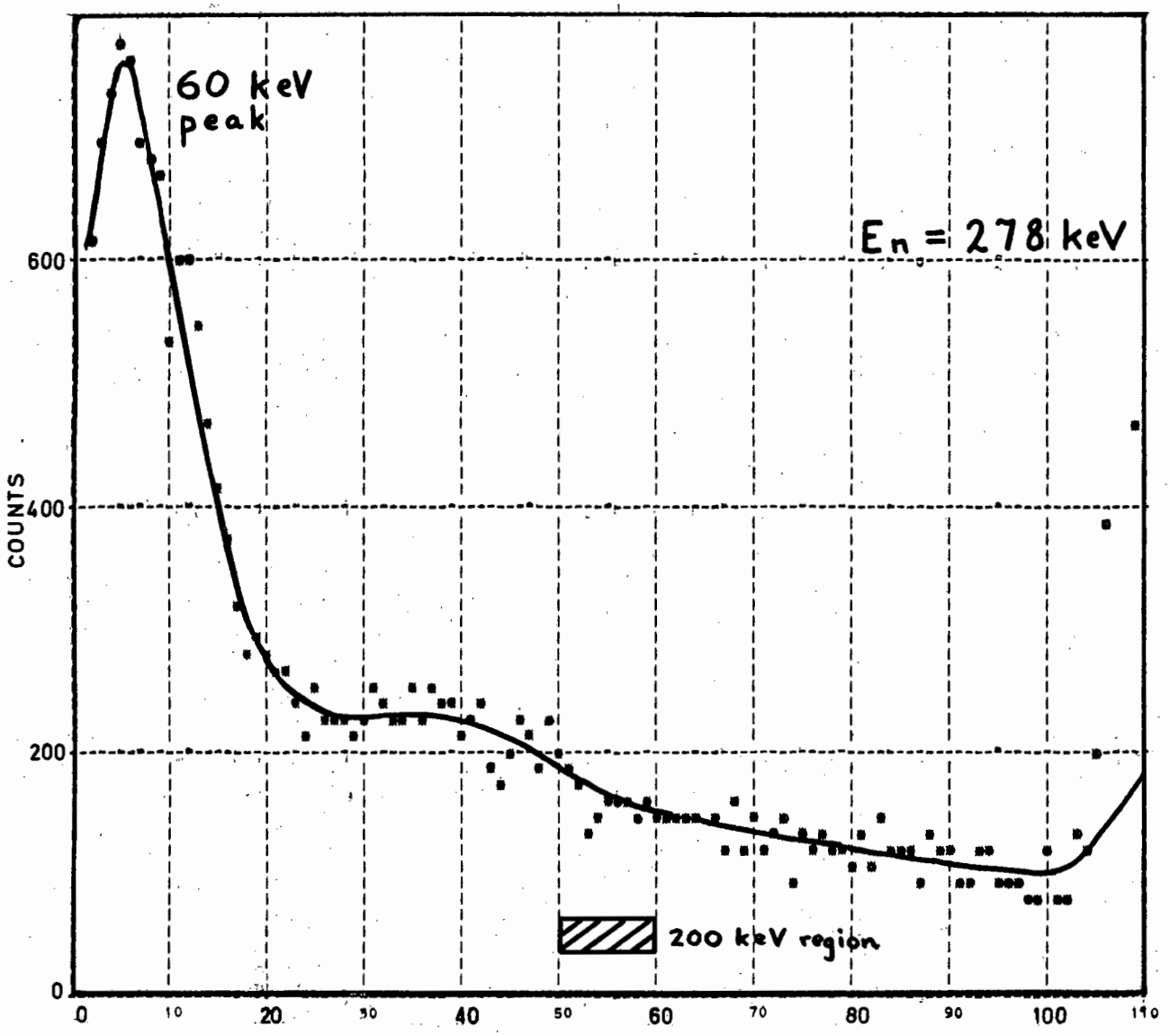

Fig 2·9(a) NaI pulse height spectrum for neutron energy >203 keV no evidence of 203 keV electron peak.

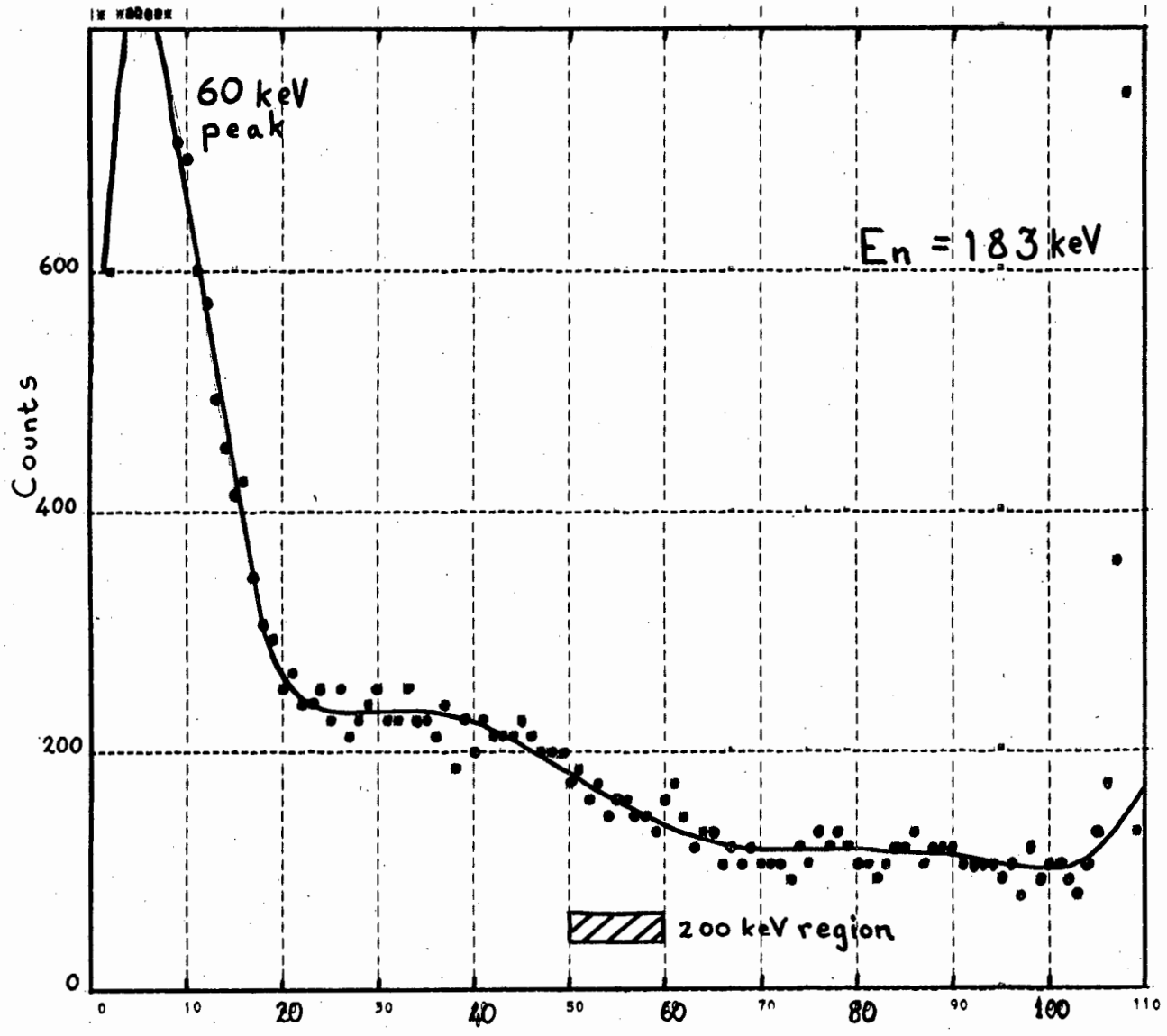

Fig 2·9(b) As for (a) but neutron energy < 203 keV. Note similar structure to that of (a).

the cesium iodide crystal was similar to that used for the sodium iodide. Pulsed neutron bombardment of the crystal gave peaks at 60, 81 and 180 keV in the pulse height spectrum. (Fig. 2.12.) The 180 keV was not due to inelastic scattering but was thought to be due to neutron capture in ^{133}Cs. The pulse height resolution for the Cesium Iodide, quoted above, is poor and any peak at 160 keV would be obscured by the observed 180 keV peak. Similarly the yield of any one level would be complicated by contributions from other nearby levels. The timing resolution is also poor. This, together with the fact that the background in the time spectrum was high, led to very low peak to background ratios. The pulse height response of the cesium iodide crystal for 60 keV gammas (^{241}Am source) was one quarter that for the sodium iodide crystal used. The above factors coupled with a low yield led to the abandonment of the investigation of CsI. Improvement of timing characteristics, e.g. by working at liquid nitrogen temperatures might enhance the possibility of worthwhile experiments with cesium iodide.

2.2.3 Investigations with Liquid Scintillators

Liquid scintillators were the second type of scintillator investigated, the first being solids, NaI and CsI. In liquid scintillators problems arise from their high hydrogen content, together with the large neutron-proton scattering cross section

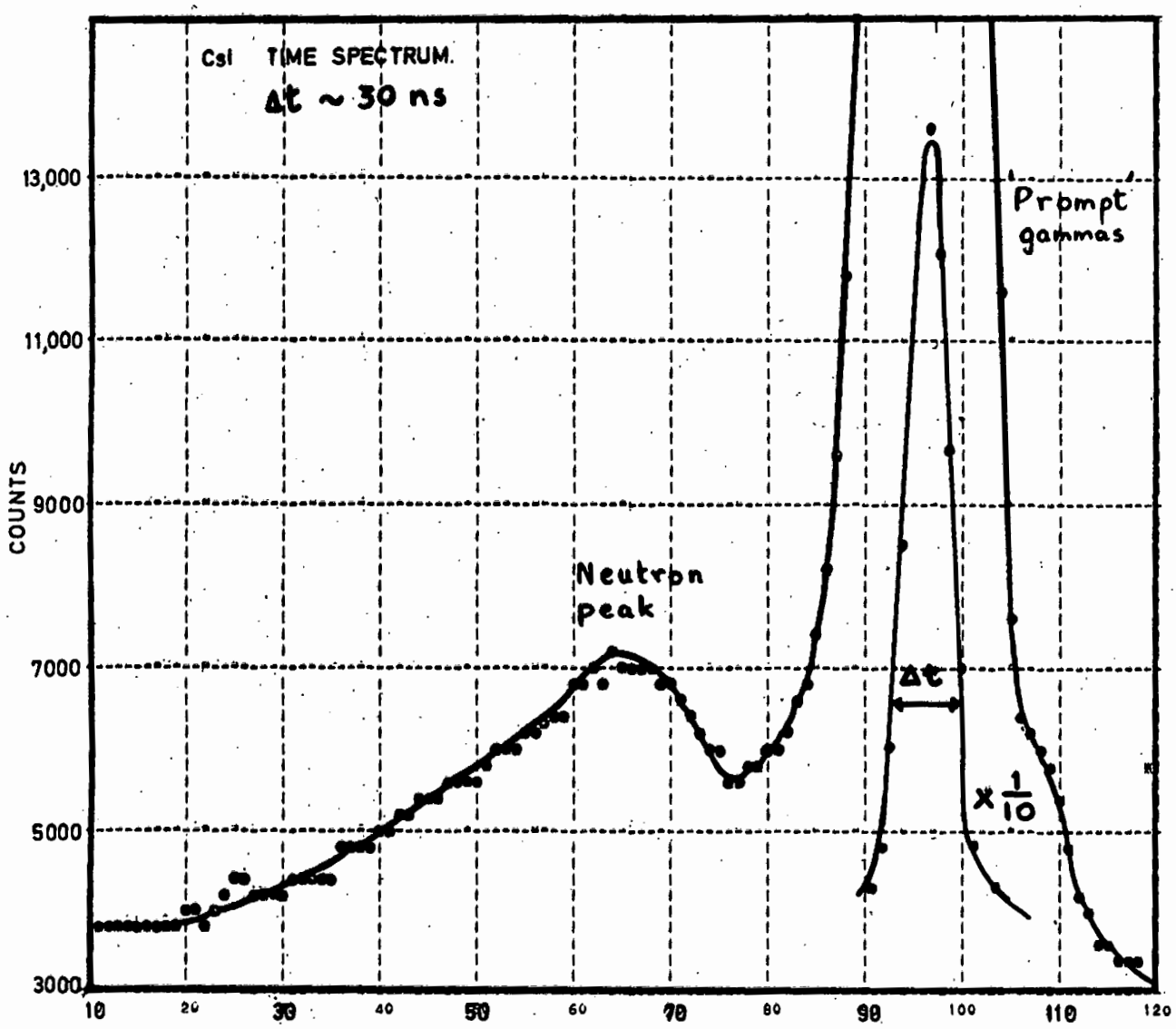

FIG 211 CsI crystal time spectrum, showing poor resolution with respect to NaI crystal fig 2·5

incident neutron energy 120 kev.

* Relative Pulse Height Response to a 1" diameter × ½ stilbene crystal.

A typical pulse height spectrum obtained using a liquid scintillator and a ^{241}Am 60 keV gamma ray source is given in Fig. 2.13. A time spectrum observed using liquid scintillator (Pr) is given in Fig. 2.14.

Fig. 2.15 a) shows the pulse height distribution obtained using a pulsed neutron beam of energy 1.304 MeV and a Bi-loaded scintillator. The edge and plateau below channel 30 are due to proton recoils, while the shoulder at about channel 40 is due to gamma rays following inelastic neutron scattering to the 0.90 MeV level of ^{209}Bi. As shown in Fig. 2.15 b the shoulder disappears when the neutron energy is dropped to 0.85 MeV. In the case of Praseodymium the internal conversion coefficient, α for the 145 keV level is 0.43. Calculations showed that 90% of the decays from this state should deposit the full 145 keV decay energy via electrons in the scintillator and that this should lead to a peak of 65% full width at half maximum in the pulse height spectrum. Figure 2.16 shows the pulse height spectrum observed over a bombarding time of approximately 120 mins. using 300 keV neutrons. This is the resultant pulse height spectrum after subtraction of the pulse height spectrum given by the background gate. Fig. 2.14. There is evidence of the expected peak but as can be seen in Fig. 2.16 the statistical spread of the counts is large. It is also evident that neutron energies exceeding 300 keV could not be used without increasing the neutron-proton recoil background to an intolerable level.

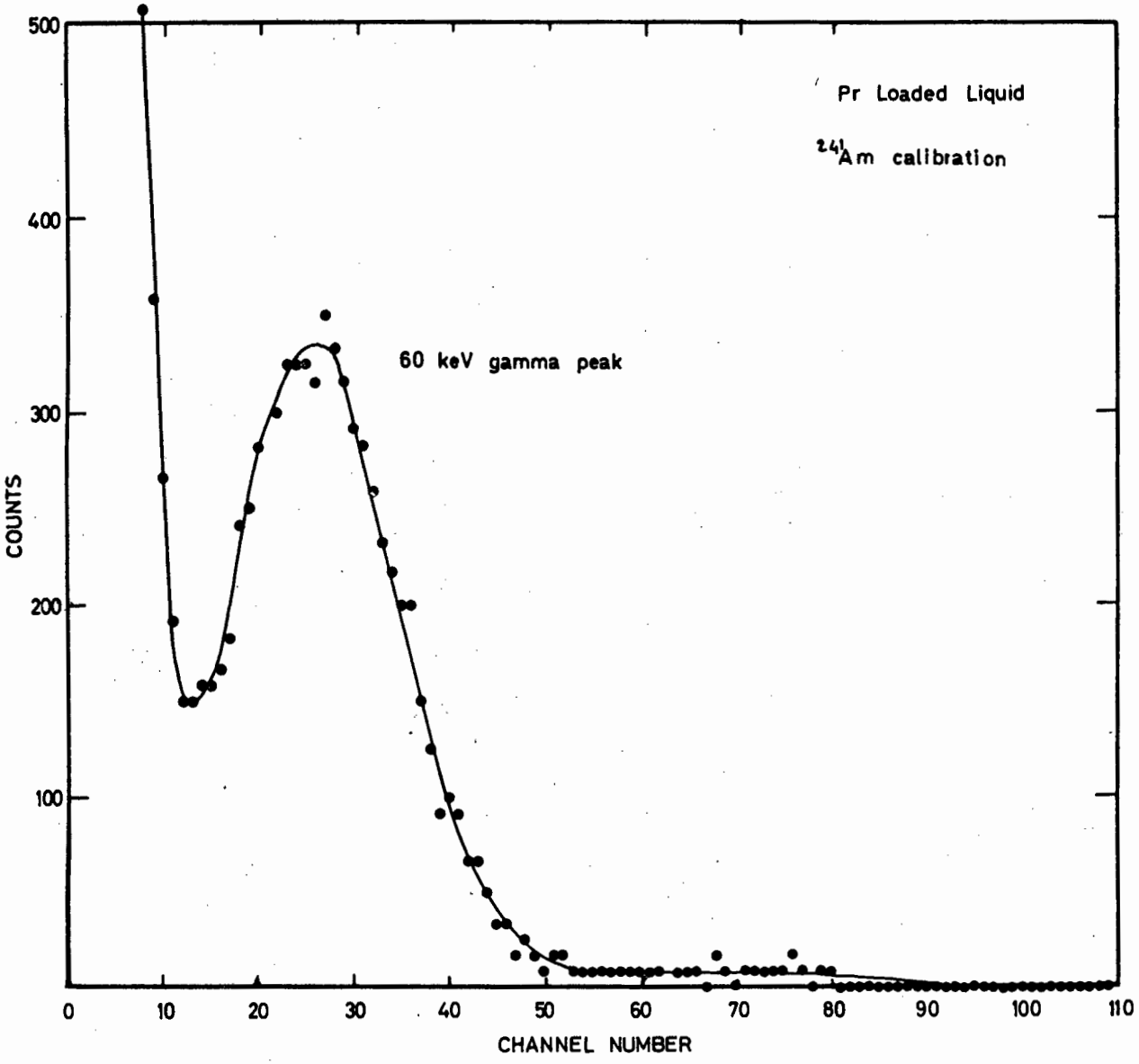

FIG 2·13 Calibration pulse height spectrum of Praseodymium loaded liquid scintillator

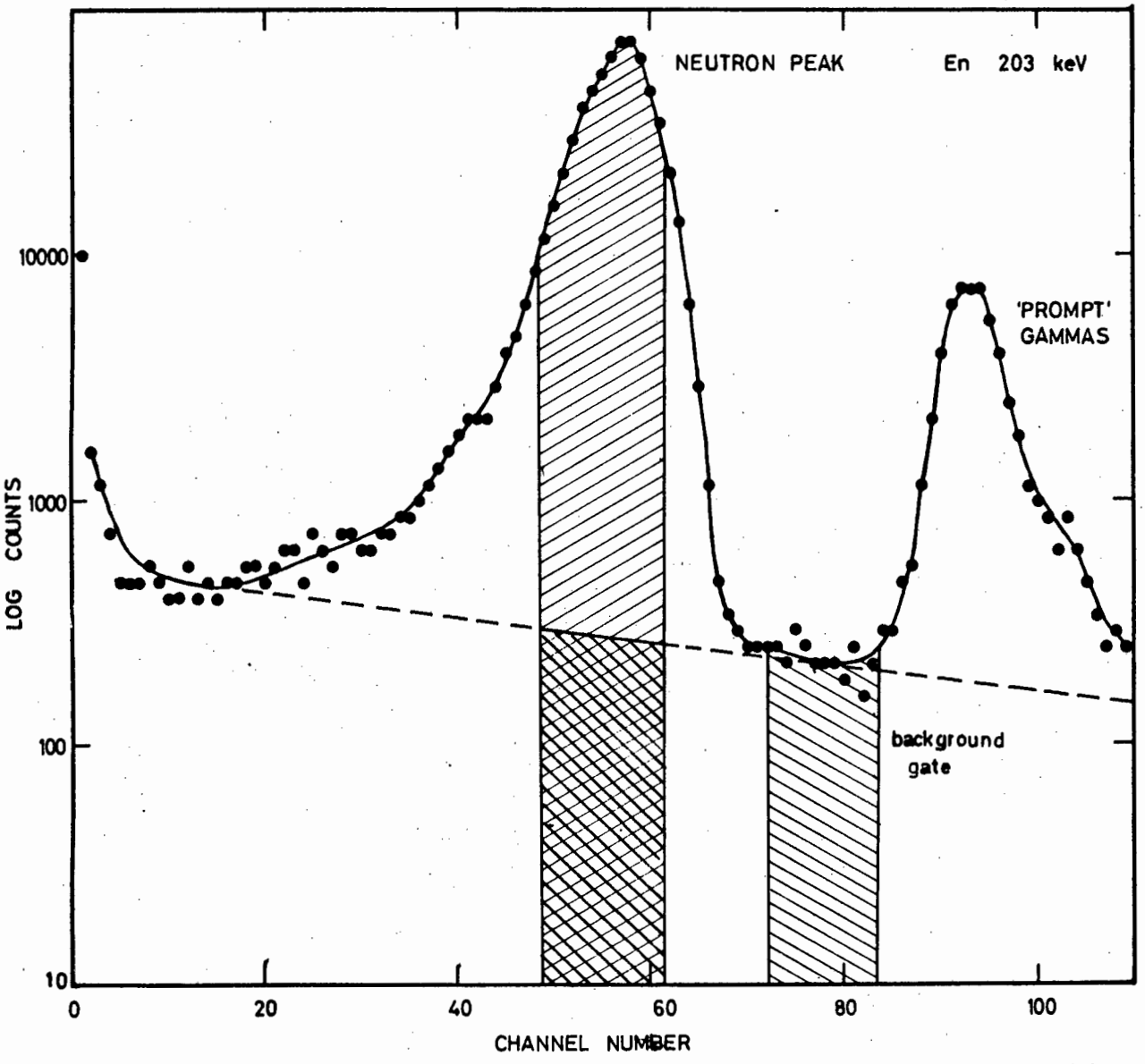

FIG 2·14 Praseodymium loaded liquid scintillator time spectrum, showing position of neutron peak gate and background gate.

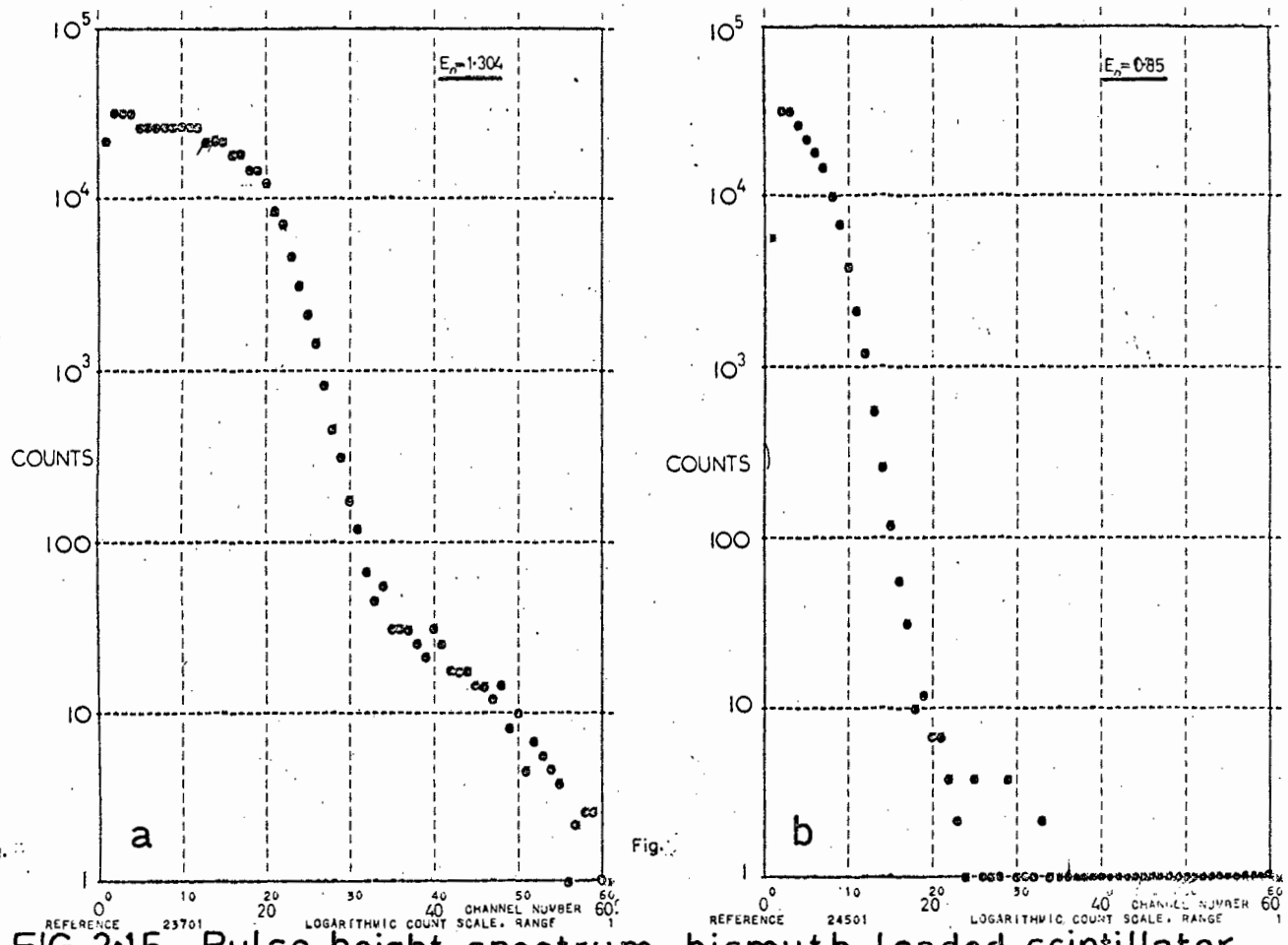

Fig. Fig.

FIG 2·15 Pulse height spectrum, bismuth loaded scintillator

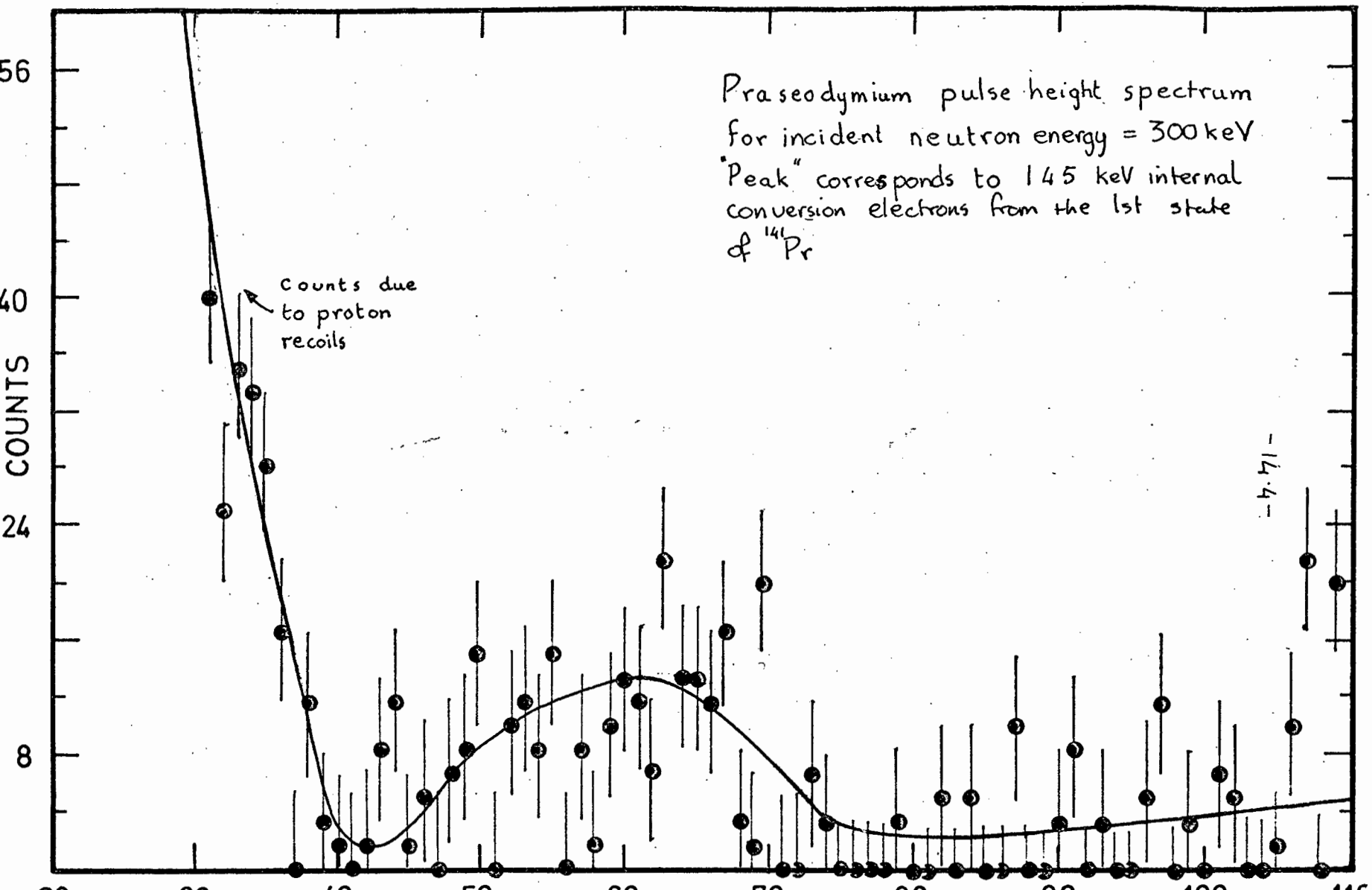
Praseodymium pulse height spectrum
for incident neutron energy = 300 keV
"Peak" corresponds to 145 keV internal
conversion electrons from the 1st state
of ^{141}Pr
Counts due
to proton
recoils
56
40
24
8
COUNTS
20
30
40
50
60
70
80
90
100
110
CHANNEL NUMBER

FIG 2·16

In the experiments with the Lanthanum and Holmium loaded liquids the results were even less encouraging. Long runs of the order of ninety mins with a beam current of 0.6 micro-amps did not yield any definite internal conversion electron peaks in the pulse height spectra. As before, counts due to proton recoils obscured possible peaks.

In general it is seen for liquid scintillators that the analysis of results is complicated by the inherent proton recoil background. A way out of this difficulty is to use pulse shape discrimination (P.S.D.) methods. Such methods enable gamma contribution in the pulse height spectrum to be counted separately from the neutrons. A P.S.D. system (Br59) was set up and a photograph of the resultant display shown in Fig. 2.17. It is seen that the neutrons occuring at the higher locus are well separated from gamma rays lower down. Clearly, using such an arrangement higher neutron energies can be used and the associated higher cross section for the various levels in the loaded element will enable the peaks to stand out more prominently.

In conclusion it can be said that the Bismuth and Praseodymium loaded liquid scintillators show definite signs of yielding results by this method. The applicability of these loaded scintillators and the others i.e. Holmium and Lanthanum for this method should be enhanced by the use of pulse shape discrimination methods.

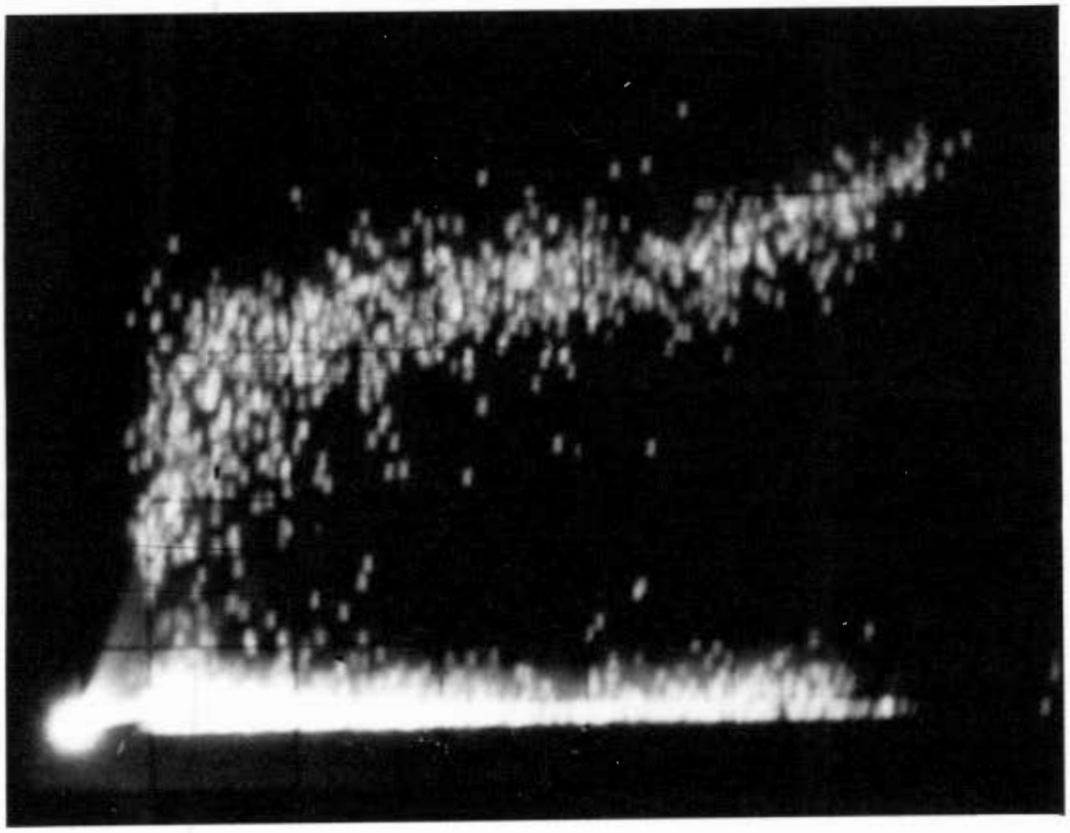

Fig 2.17 PSD display, Pr loaded liquid. Neutrons above, gammas below.

2.2.4 The Investigations of Gel Scintillators.

The gel method has been used by a number of authors (Ot59, Mo61,He60) mainly for detection of beta rays. The present investigations were aimed at testing the suitability of Lanthanum loaded gels for neutron inelastic scattering measurements by detecting the de-excitation internal conversion electrons.

The basic scintillator used was liquid Ne213 which was gelled by mixing directly with 4% to 6% by weight of Cab O Sil, a SiO_2 thioxotropic agent. Although the gel appears somewhat cloudy its light transmitting properties are virtually the same as that of pure Ne213 liquid at the depth used; maximum of 1 cm.

The loaded element was in the form of a powder with a particle size of approximately 1 micron to keep self absorption effects of the conversion electrons in the particle to less than 20%. At first La_2Cl_3 was powdered by hand and used as the load but proved unsatisfactory as clumping occured due to its hydroscopic nature. La_2O_3 which was already finely powdered was subsequently used. The load was varied between 1% to 5% and the depth of the gel from 0.1 cm to 1 cm to obtain the best Compton edge from a ^{241}Am 60 keV gamma source. Fig. 2.18. A loading of 2% and depth of 0.2 cm proved optimum.

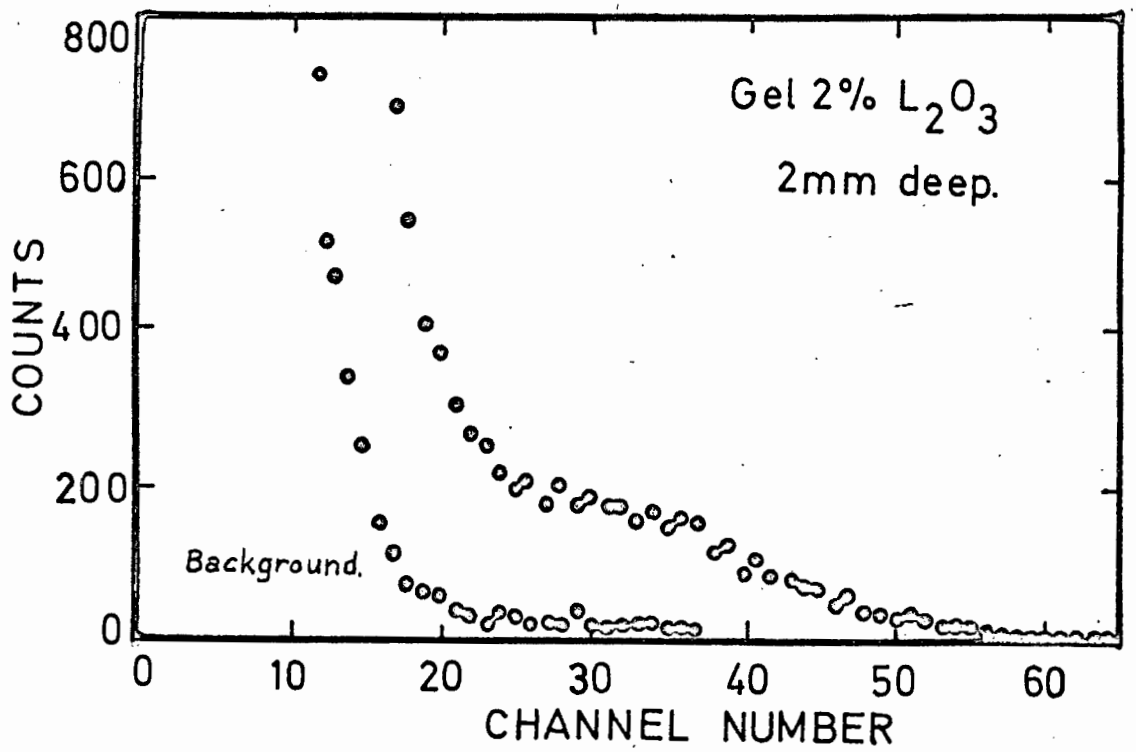

Fig. 2.18. Am 60 keV pulse height spectrum.

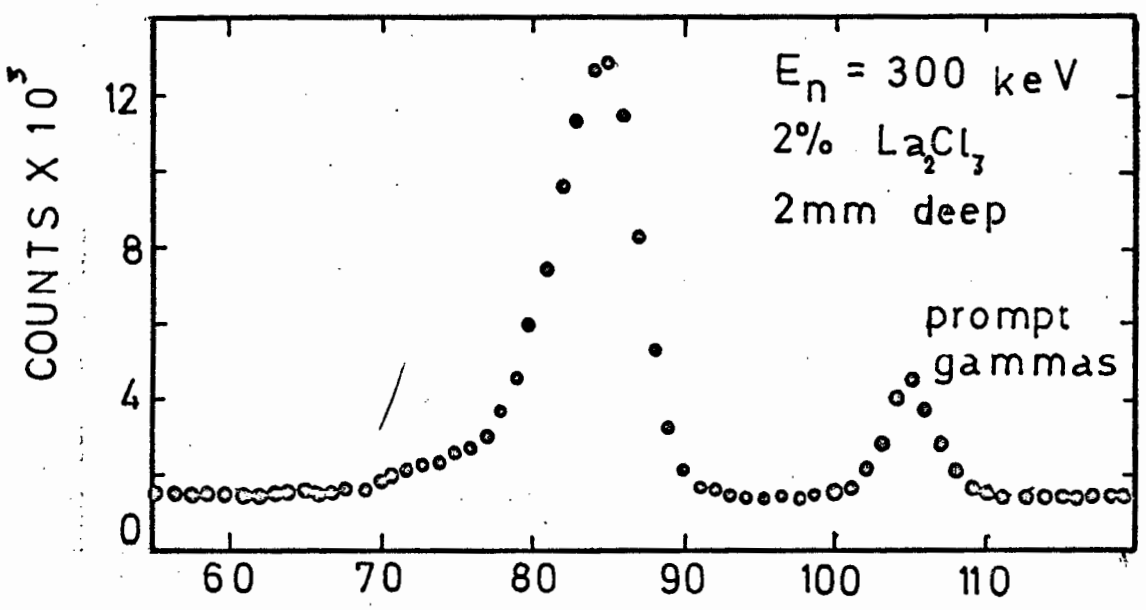

FIG 2·19 Time spectrum for La_2Cl_3 loaded gel

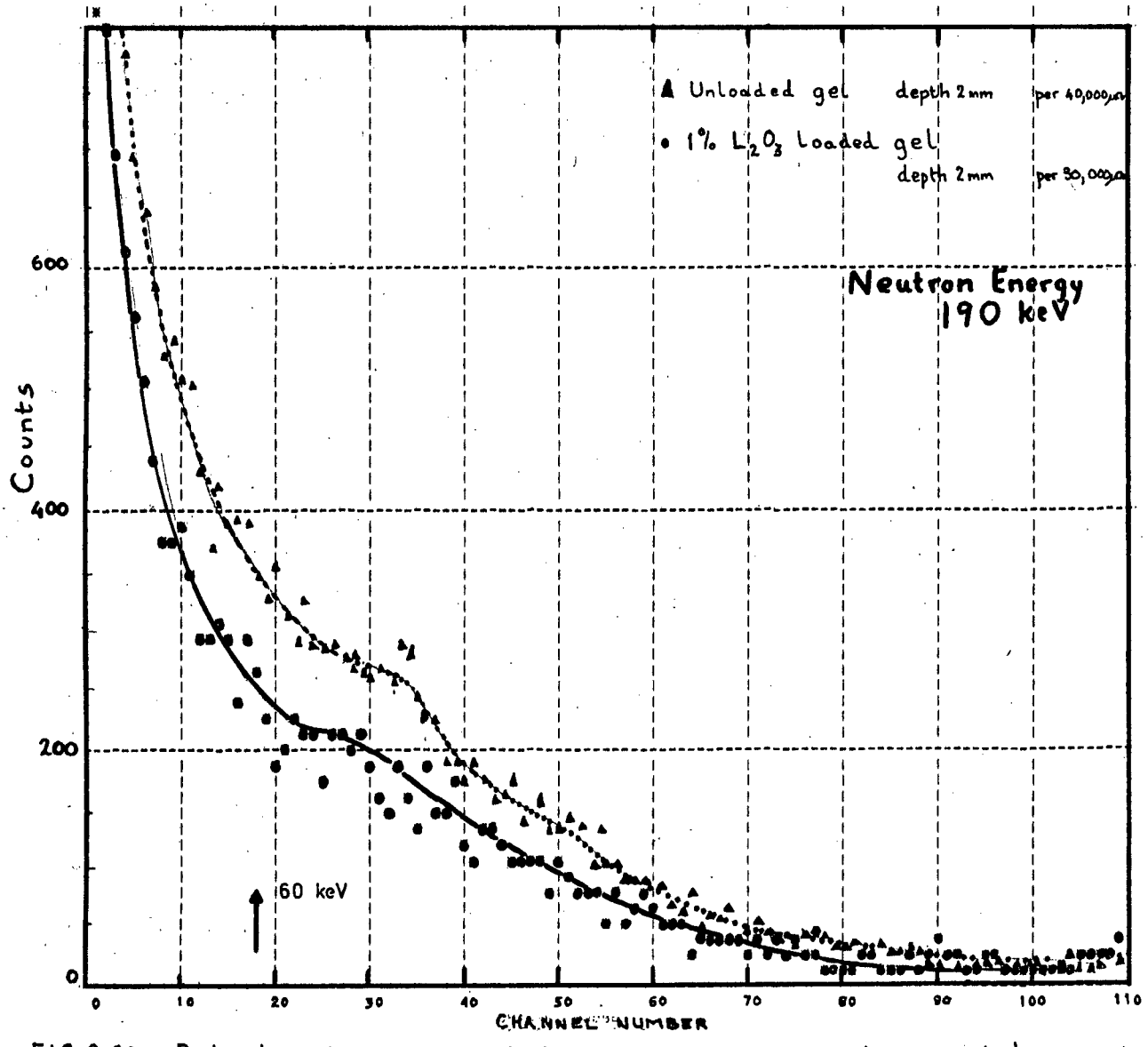

FIG 2·20 Pulse height spectrum at 190 keV neutron energy, showing similar structure for unloaded gel (dashed curve) and loaded Gel. Note that former is yield due to 40,000 μCb (proton beam current) and Latter is yield due to 30,000 μCb.

Fig. 2.19 shows a time spectrum obtained using a 2% Lathanum Chloride loaded gel for a neutron energy of 300 keV. Although a shoulder was observed in pulse height spectra at approximately 100 keV it was found that the same structure also occured for unloaded gels. Fig. 2.20. As with liquid scintillators proton recoils contribute greatly to the pulse height spectra. No peaks due to internal conversion electrons were observed. Investigations with Gels were therefore abandoned. It might be possible to improve the performance of gels by using (i) P.S.D. methods (ii) finer grain size in the gel to further reduce self absorption of the conversion electrons and (iii) optimization of the constituents and physical nature of the gel such as homogeneous mixing of the load, and depth.

2.3. Conclusions.

By far the most promising scintillator investigated was the sodium iodide crystal. Although cesium iodide gave pulse height spectra showing peaks at 60 and 81 keV Fig. 2.12 the pulse height and timing resolution were rather poor and did not merit any serious investigations of inelastic scattering to these levels.

Neither the liquid nor the gel scintillators yielded good results. However the Bismuth and Praseodymium loaded liquids show indications of yielding results; especially if pulse shape

discrimination methods are used. The suggested improvements mentioned for the gel scintillators would enhance the possibility of using the gels in inelastic studies; such improvements were not carried out.

Because results with the sodium iodide crystal were so promising, it was decided to investigate in detail inelastic scattering to the 59 keV state of ^{127}I. The following section describes experiments aimed at determining the cross section data for the excitation of the 59 keV level.

3. INELASTIC SCATTERING TO THE 59 keV LEVEL OF ^{127}I.

3.1 Introduction

The following investigation was undertaken after the promising results obtained in Chapter 2.

The 59 keV level of ^{127}I was populated by inelastic neutron scattering in a NaI crystal (1.6 mm thick x 32 mm.diameter). The resultant pulse height spectrum is shown Fig 2.7. The inelastic scattering cross section was determined by measuring the yield of de-excitation radiations from the 59 keV level for a known incident neutron flux. The neutron flux was measured by means of a 7.5% ^{6}Li-loaded glass scintillator NE905, $1\frac{1}{2}$" diam. x $\frac{1}{2}$". An60. The NaI and Li-glass detectors were placed Fig. 3.1 with axes aligned symmetrically ($\theta \sim 10^{o}$) about the proton beam direction ($\theta = 0^{o}$). The incident neutron flux per unit area at the two detectors was therefore the same.

The operation of the Li glass detector in a time-of-flight system is similar to that for NaI crystal as described in section 2.2.1.

In the case of the glass the pulse height spectrum shows a peak corresponding to products of reactions Li $(n,\alpha)T$. Fig.3.2. shows pulse height spectrum using 60 keV neutrons. Fig. 3.3a shows a typical time-of-flight spectrum obtained with a gate set on the peak seen in Fig. 3.2.

Time-of-flight spectra and/or pulse height spectra from the two detectors were recorded simultaneously. Most of the

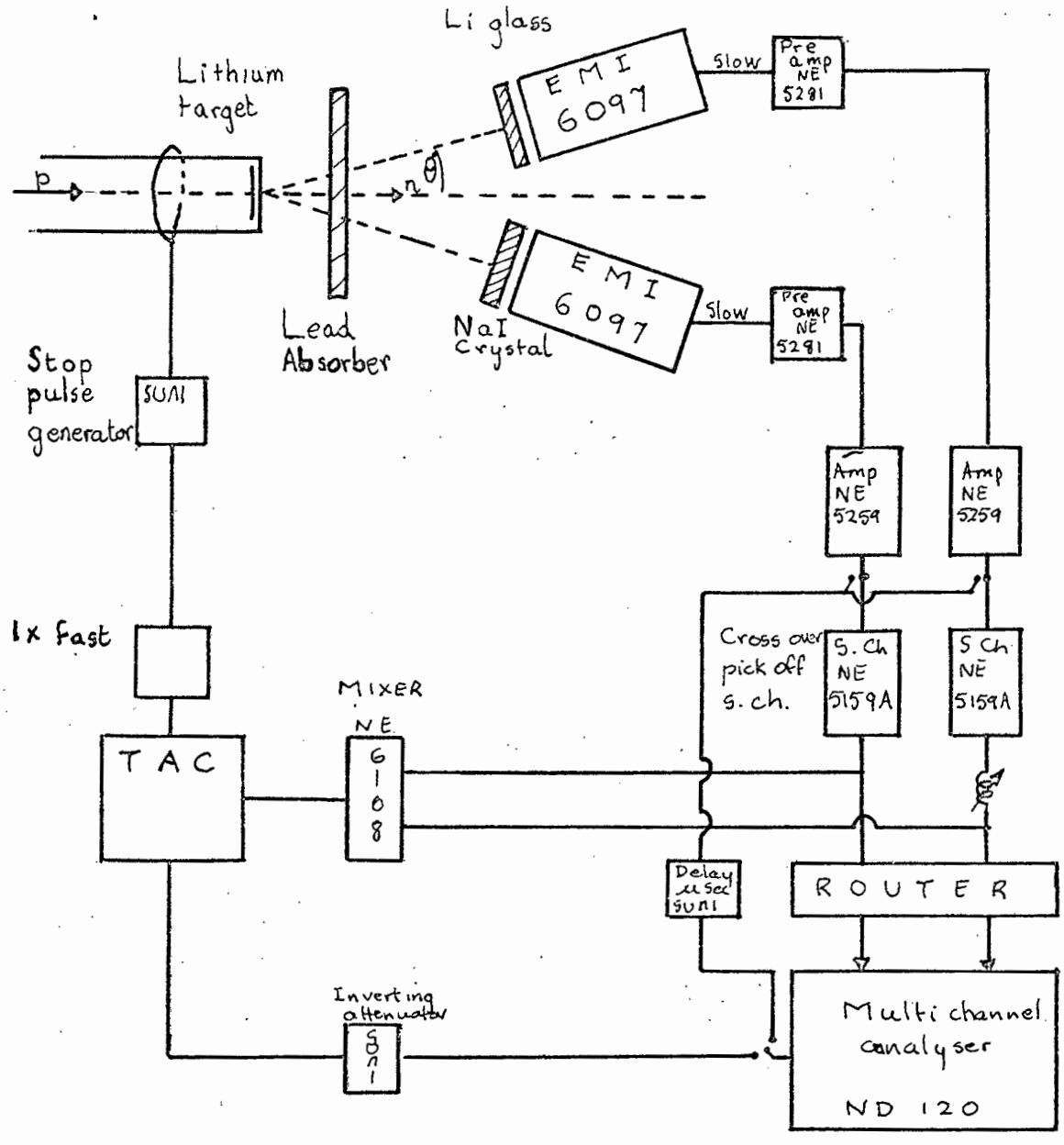

FIG 3·1 Block diagram of electronics used for NaI crystal studies

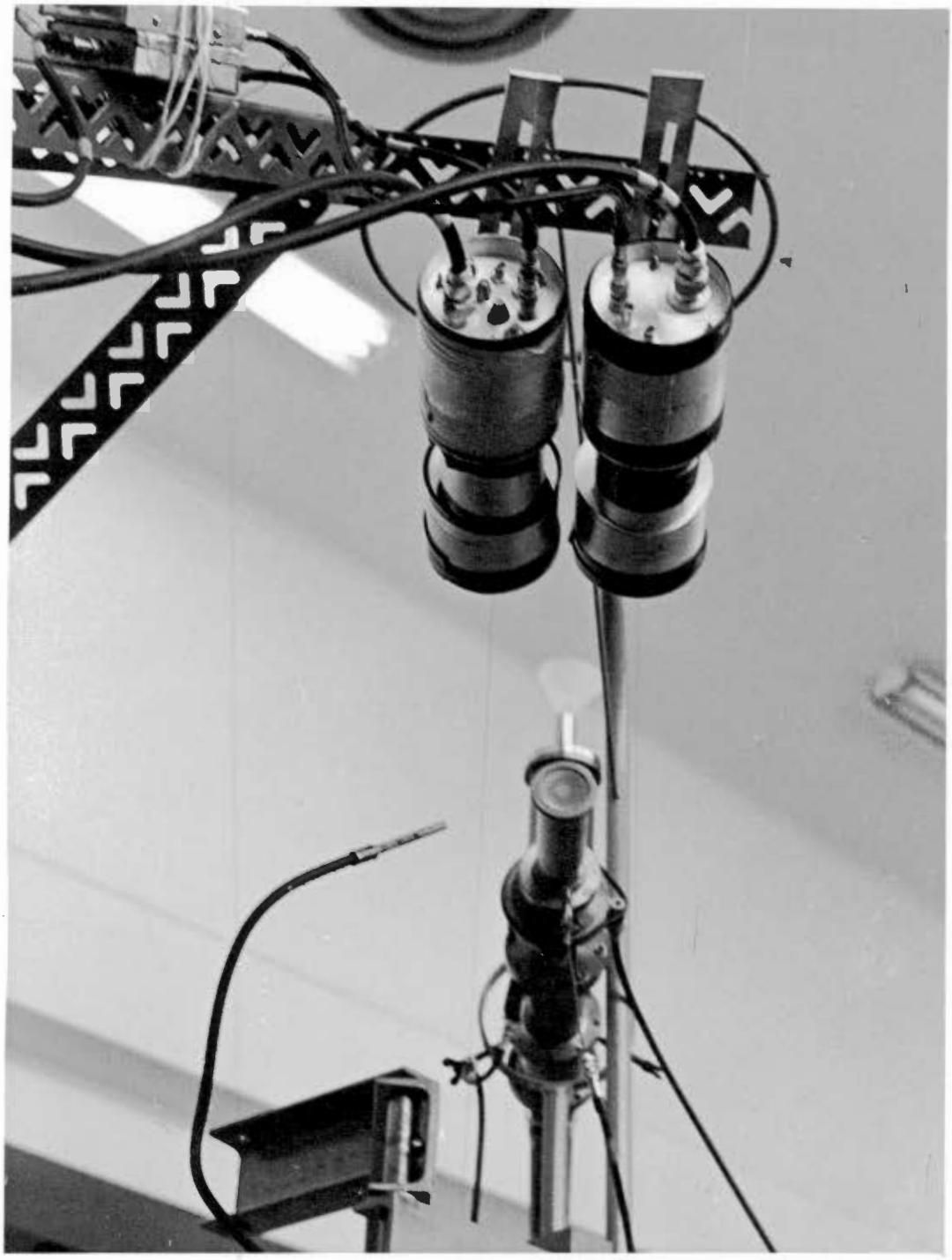

Fig 3.1b Laboratory arrangement.

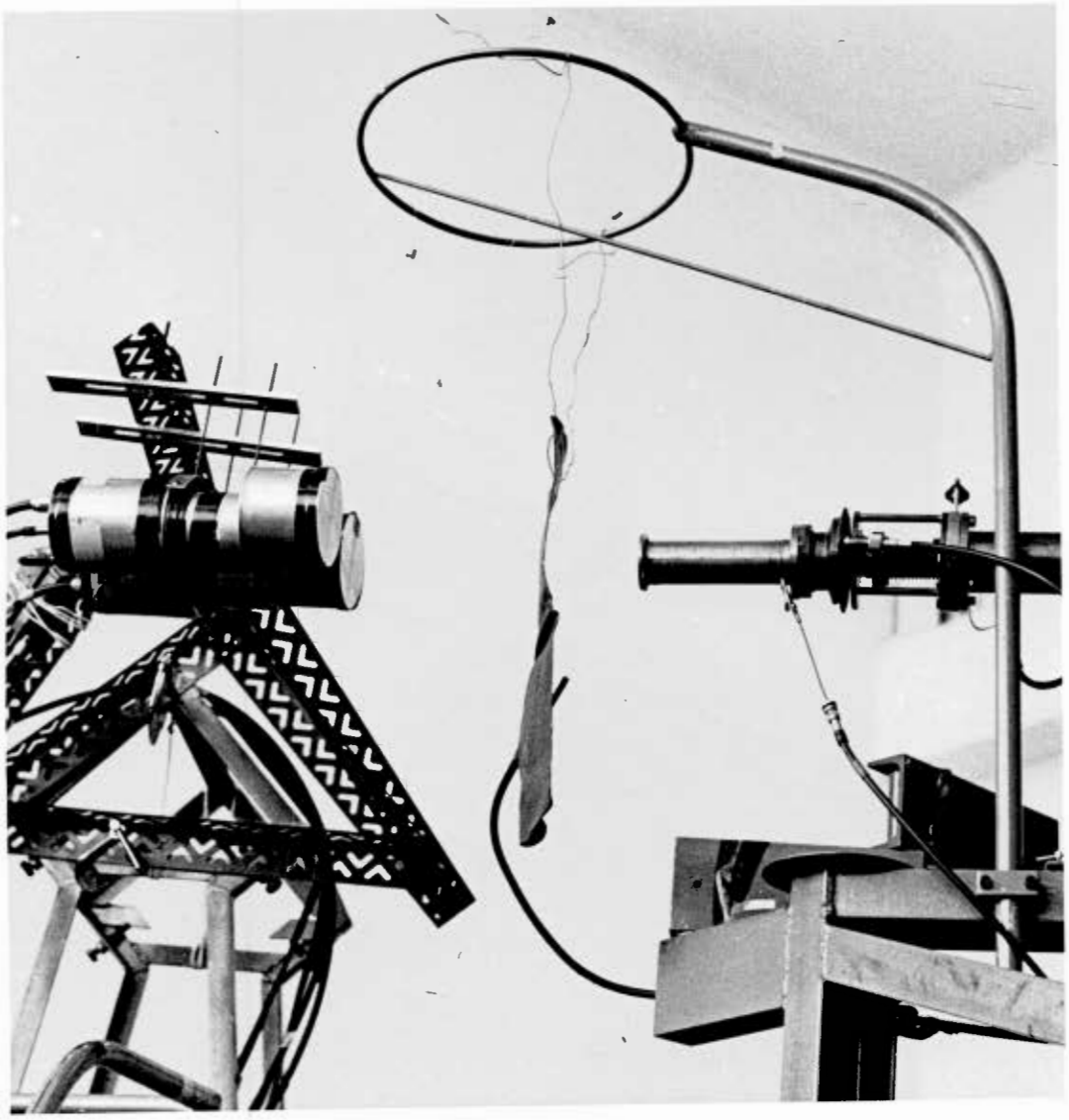

Fig 3.1c Laboratory arrangement.

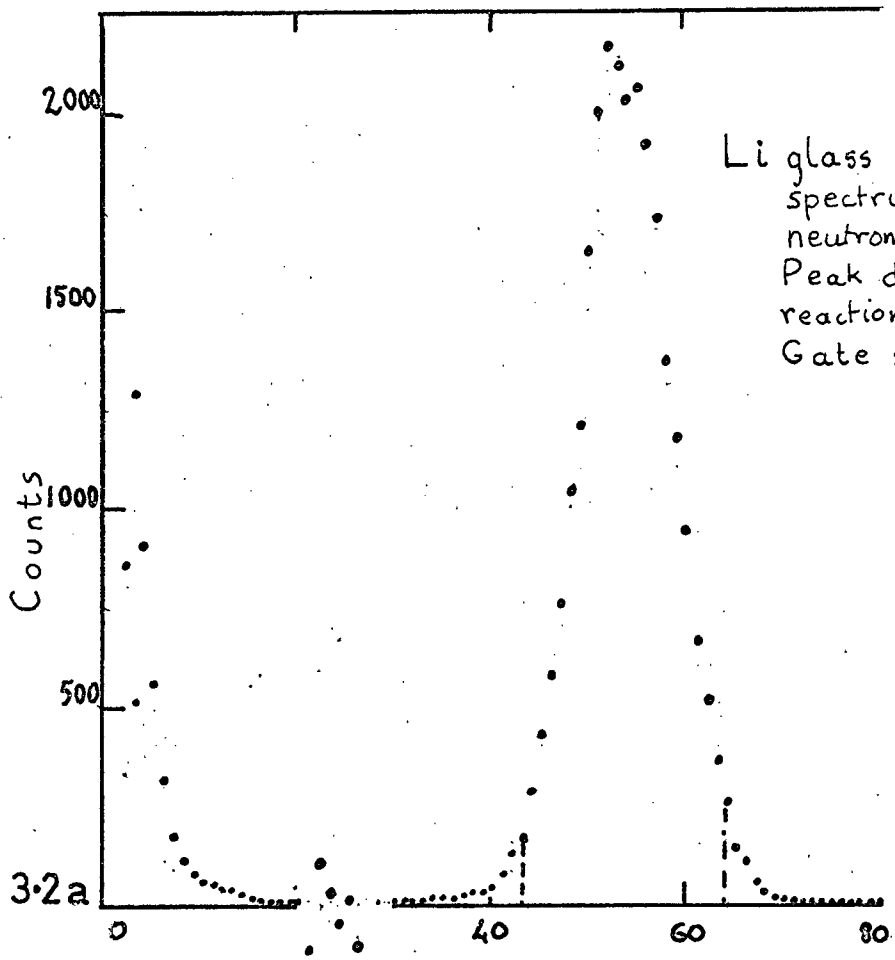

Li glass pulse height spectrum for 60keV neutrons
Peak due to (n, α) reaction.
Gate set on peak.

FIG 3·2a

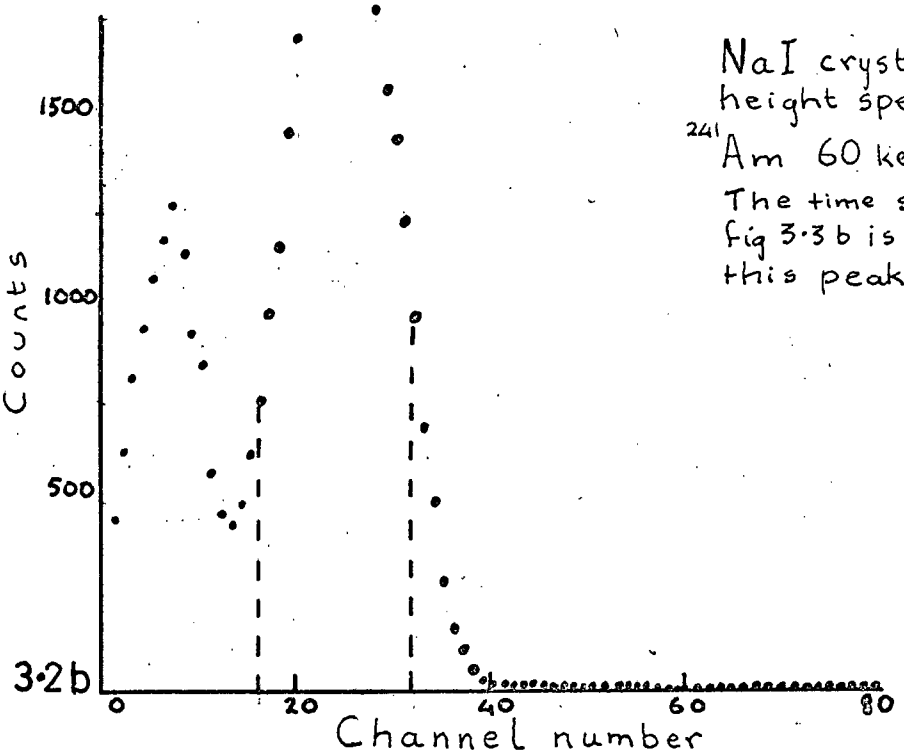

NaI crystal pulse height spectrum with ^{241}Am 60 kev gammas.
The time spectrum fig 3·3 b is gated on this peak.

FIG 3·2b

data were obtained using monoenergetic neutrons i.e. ^{7}Li targets of less than 5 keV thick. In this work neutron energy was calculated from proton energy and kinematics of ^{7}Li (p,n) reaction as outlined in Chapter 2. c.f. Fig.2.1.

Some work was carried out using a thick (> 30 keV) target, which produced neutrons having a wide range of energies. This led to measurement of $\sigma_{n'}$ as a function of time-of-flight (i.e. neutron energy).

Before dealing with measurements of excitation function we note the importance of experimental symmetry about 0^{o} and indicate how $\theta = 0^{o}$ was calibrated.

3.2 Measurements for obtaining Cross Section Data.

3.2.1 Calibration of the $\theta = 0^{o}$ Line

The Li glass detector was placed (Fig. 2.4) at $+\theta^{o}$ and then $-\theta^{o}$ to the nominal 0^{o} line of the S.U.N.I. Van de Graaff "neutron line". In each case the neutron time-of-flight spectrum was obtained. For the energy used the angle of divergence from the Li target of the neutron beam was 16^{o} (Fig. 2.1) and the energy ranged from 30 to 45 keV. Any errors in angular measurements would be noticed as a difference in the time-of-flight between the spectra taken at the two angles. Within experimental resolution no such difference was detected and the nominal zero line was therefore assumed to be correct.

3.2.2 Thin Target Method.

From experimental symmetry we know that the incident neutron flux per unit solid angle is the same at both the glass and NaI detectors. Since these solid angles are small and approximately equal, we assume that the fluxes incident on the glass and crystal respectively will be proportional to the front face areas, α_1 and α_2 of the respective scintillators. Using a thin target therefore let $\alpha_1 N_o$ be the number of neutrons per sec. of mean energy E incident on the Li glass. The number of (n,α) events per sec. N_1 is given by

$$N_1 = \alpha_1 N_o \phi_1 n_1 \sigma_\alpha \qquad (3.1)$$

where n_1 is the number of ^6Li nuclei per cm^2 in the glass. σ_α is the cross section for ^6Li (n,α) reaction at energy E, and ϕ_1 is a factor introduced to correct for the effects of self screening (flux attenuation) and multiple scattering in the glass scintillator.

In the case of the NaI crystal a completely analogous expression is obtained for $\omega_2 N_2$ the rate at which the 59 keV level is populated by inelastic neutron scattering.

$$N_2 = \alpha_2 N_o \phi_2 n_2 \sigma_{n'} \qquad (3.2)$$

where n_2 is the number of iodine nuclei per cm^2 in the NaI crystal, ϕ_2 is a correction factor analogous to ϕ_1 and $\sigma_{n'}$ is the cross section for those inelastic neutron scatterings

which lead to the 59 keV level being populated. We defer further discussion of the correction factors ϕ_1 and ϕ_2 to section 3.3, noting only that in the desirable limit of thin scintillators they will approach the value unity.

From equations 3.1 and 3.2 we are able to express $\sigma_{n'}$ in terms of σ_α as follows:-

$$\sigma_{n'} = \frac{\alpha_1}{\alpha_2} \frac{\phi_1}{\phi_2} \frac{N_1}{N_2} \frac{n_1}{n_2} \sigma_\alpha \qquad (3.3)$$

Thus we can determine $\sigma_{n'}$ from measurements of N_1 and N_2, provided we know σ_α and can calculate ϕ_1 and ϕ_2. This is the basis of the method used in these experiments.

Now N_1 can obviously be measured directly since the efficiency of the glass for detecting (n,α) events within it is very close to unity. With a pulse height analyser set on the neutron peak in the pulse height spectrum as in Fig. 3.2a, the time spectrum gated by this analyser is observed. (Fig. 3.3a). N_1 is then obtained by integrating the area under the "neutron peak" after subtraction of background as shown in Fig. 3.3a.

A similar procedure is followed for the NaI crystal. The pulse height analyser in this case is set to cover the observed 59 keV peak (Fig.2.7) in the NaI pulse height spectrum. In practice this gate is set on the Am calibration peak Fig. 2.6. N_2 is measured by taking a time spectrum Fig. 3.3b gated by the 59 keV pulse height window. The area N_2 can be attributed

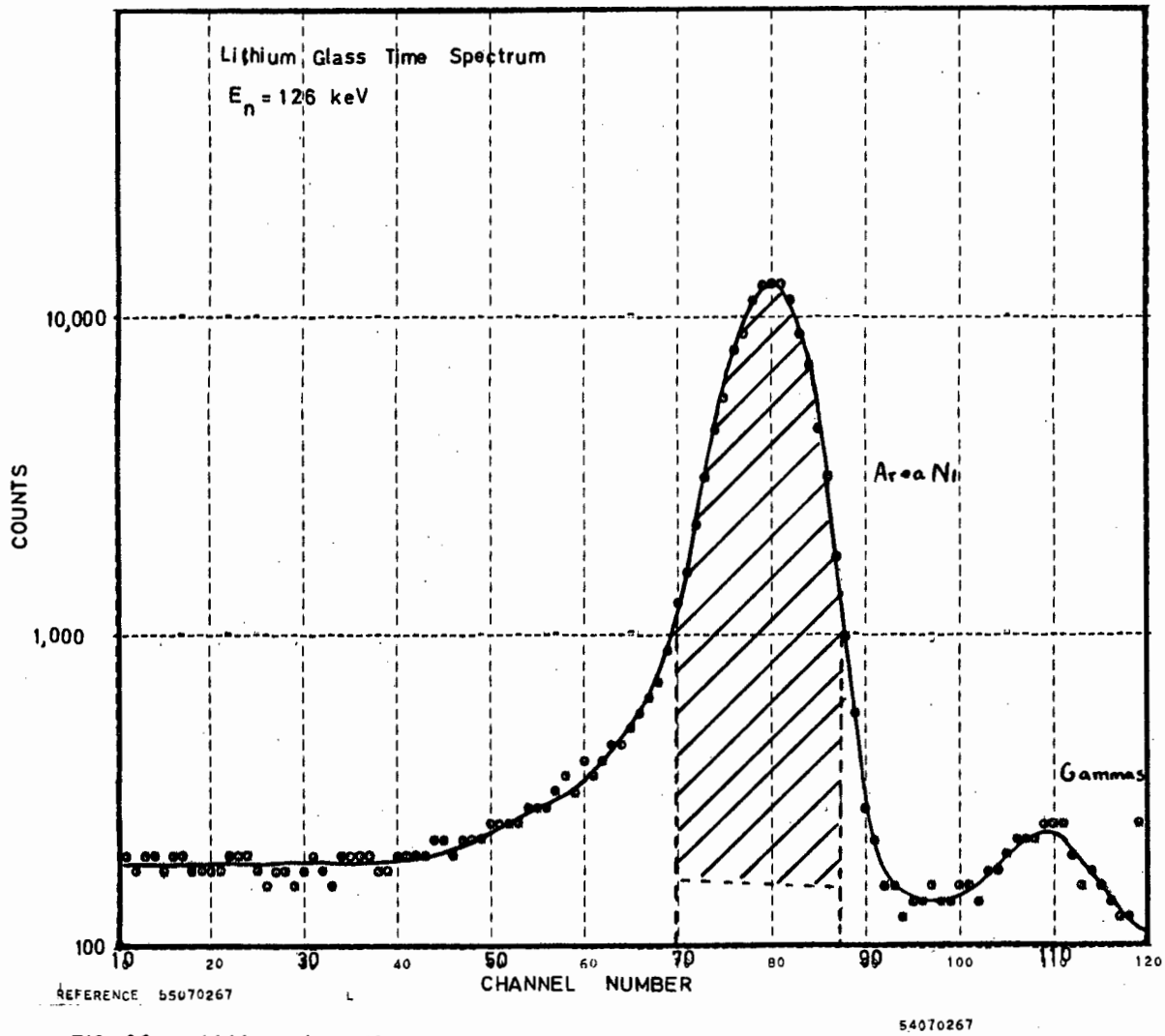

FIG 3·3 a Lithium glass time spectrum thin target.

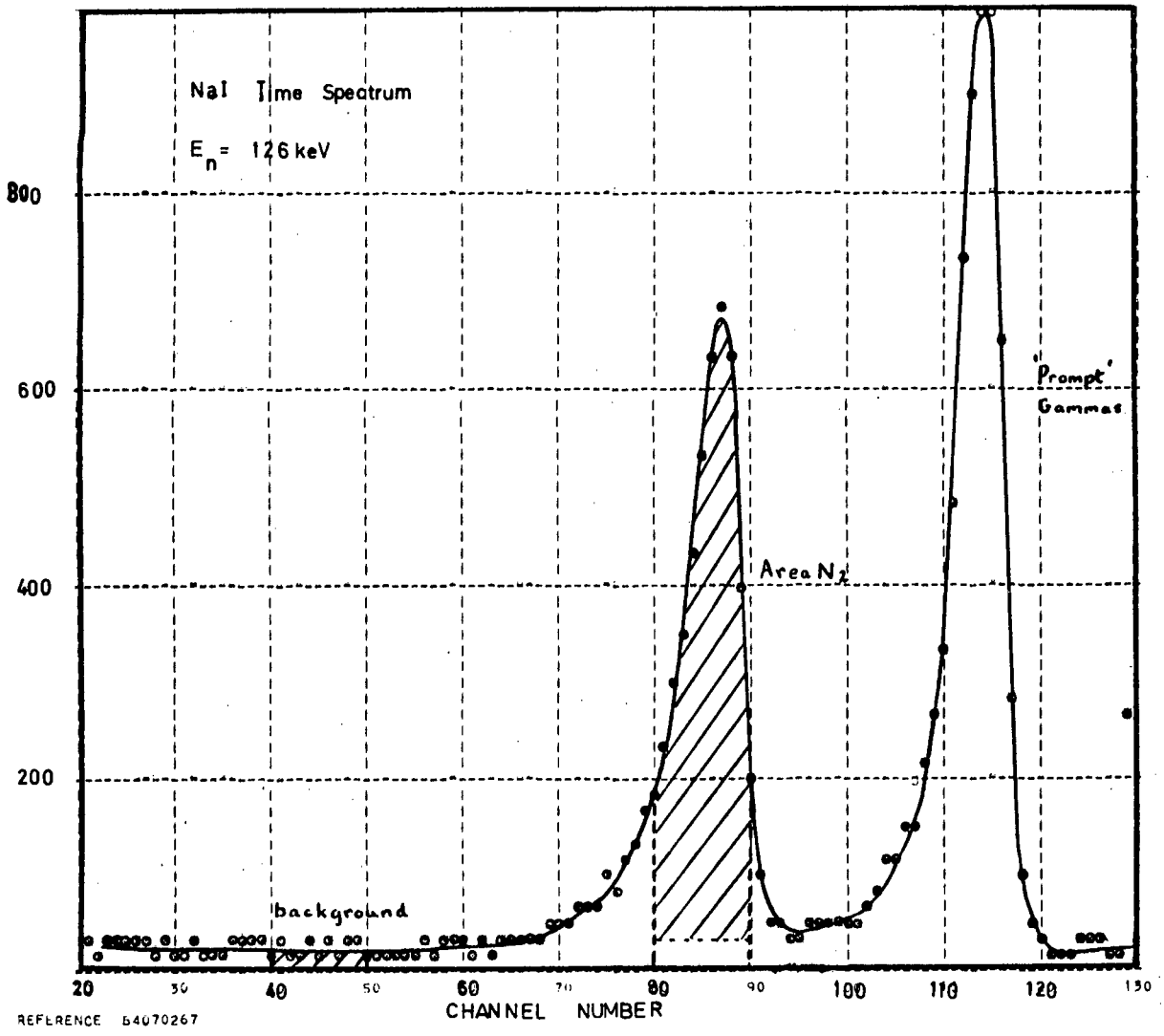

REFERENCE B4070267

FIG 3·3 b NaI time spectrum, thin target 2 keV

to internal conversion electron counts and gamma counts. The contribution of each is given by a function of α the internal conversion coefficient and the detection efficiency for electrons and gamma rays i.e.

$$f = \varepsilon_e \frac{\alpha}{1+\alpha} + \varepsilon_\gamma \frac{1}{1+\alpha} \qquad (3.4)$$

where ε_e is electron detection efficiency,

ε_γ is gamma detection efficiency

and α is internal conversion coefficient.

The detection efficiency for electrons at 60 keV is virtually unity. An estimation of gamma detection efficiency at 60 keV gives a value better than 0.9. This is based on the value for absorption of 60 keV gamma rays in sodium iodide (Be65b) for a path length $\sim$ 0.1 cm. With $\varepsilon_e = 1$ and $\alpha = 1.95$ (Kn56) expression (3.4) reduces to $f = 0.97$.

If we now redefine N_2 as the counting rate in the 59 keV peak then we must rewrite equation 3.3 as follows:-

$$\sigma_{n'} = \frac{\alpha_1}{\alpha_2} \cdot \frac{\phi}{f} \cdot \frac{N_1}{N_2} \cdot \frac{n_1}{n_2} \cdot \sigma_\alpha \qquad (3.5)$$

where $\phi = \frac{\phi_1}{\phi_2}$

The time-of-flight spectra (Figures 3.3a and 3.3b) are obtained simultaneously, hence the ratio N_2/N_1 is then equal to the ratio of the "neutron peak" areas in the respective spectra.

A block diagram of the electronics used for measuring time-of-flight spectra is shown in Fig. 3.1. The signals from the two scintillation detectors were fed via NE 5259 amplifiers (operating in bipolar mode) to NE 5159A "cross-over-pickoff" pulse height analysers. The outputs from the analysers were coupled together (through a NE 6108 mixer) to provide a common start pulse to the time-to-amplitude converter. The analyser outputs were also used individually to route time-of-flight spectra corresponding to the two detectors each to a different segment of the Nuclear Data ND-128 multichannel analyser. In passing it may be noted that the use of this arrangement avoided, the need to apply corrections for dead time losses in the multichannel analyser, since the corrections would be the same for each detector and therefore cancel out in taking the ratio N_2/N_1 in equation 3.4.

The cross section $\sigma_{n'}(E)$ was thus measured as a function of neutron energy E_n, by observing a series of time spectra at different proton energies. Photographic records depicting an oscilloscope spectrum display of the multichannel analyser were obtained for each run; some of these are shown in Fig. 3.4. Average length of runs were 20 minutes. In each case the neutron energy was calculated from the proton energy as outlined

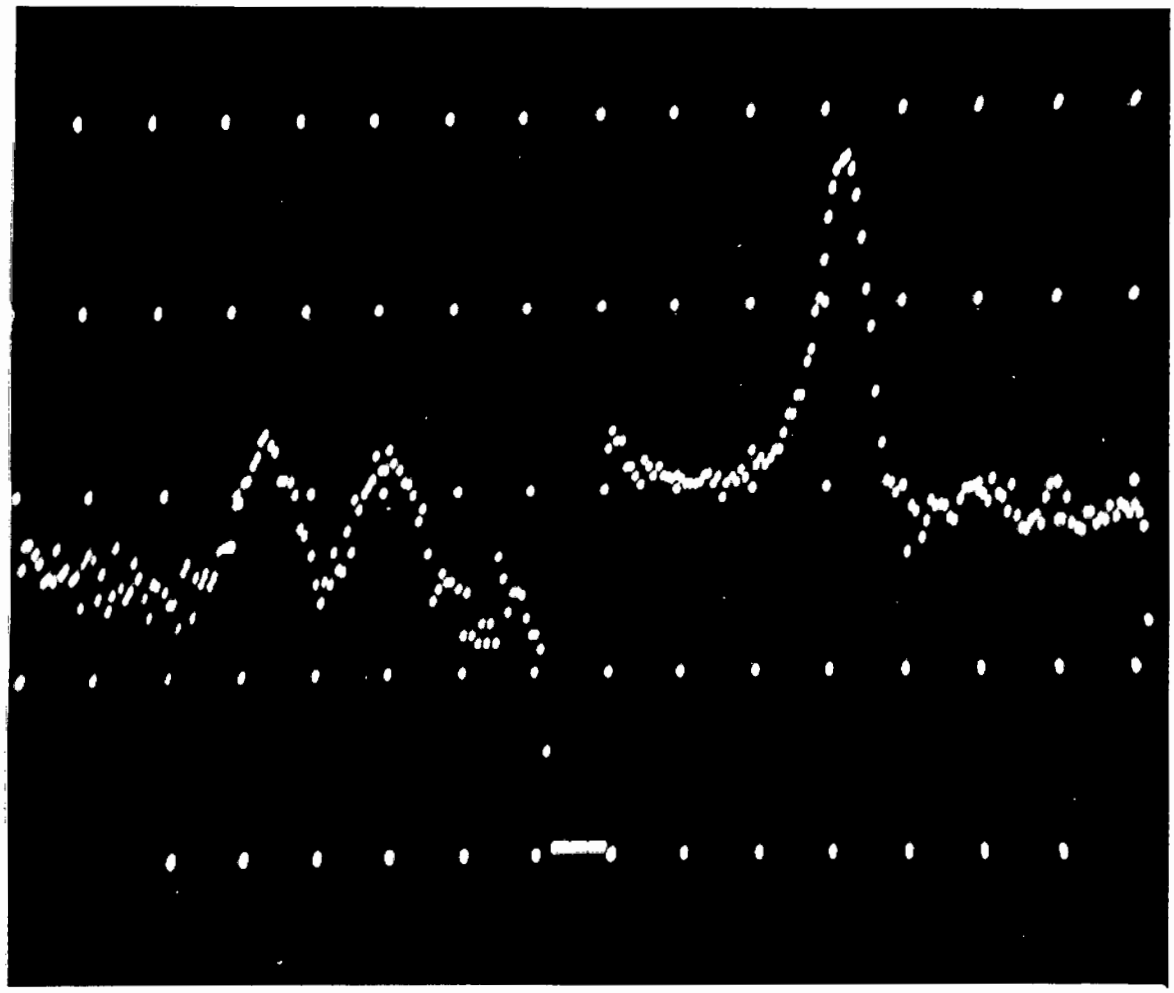

Fig 3.4 Multichannel analyser display of time spectra

NaI on left, Li glass on right. E_n 152 keV

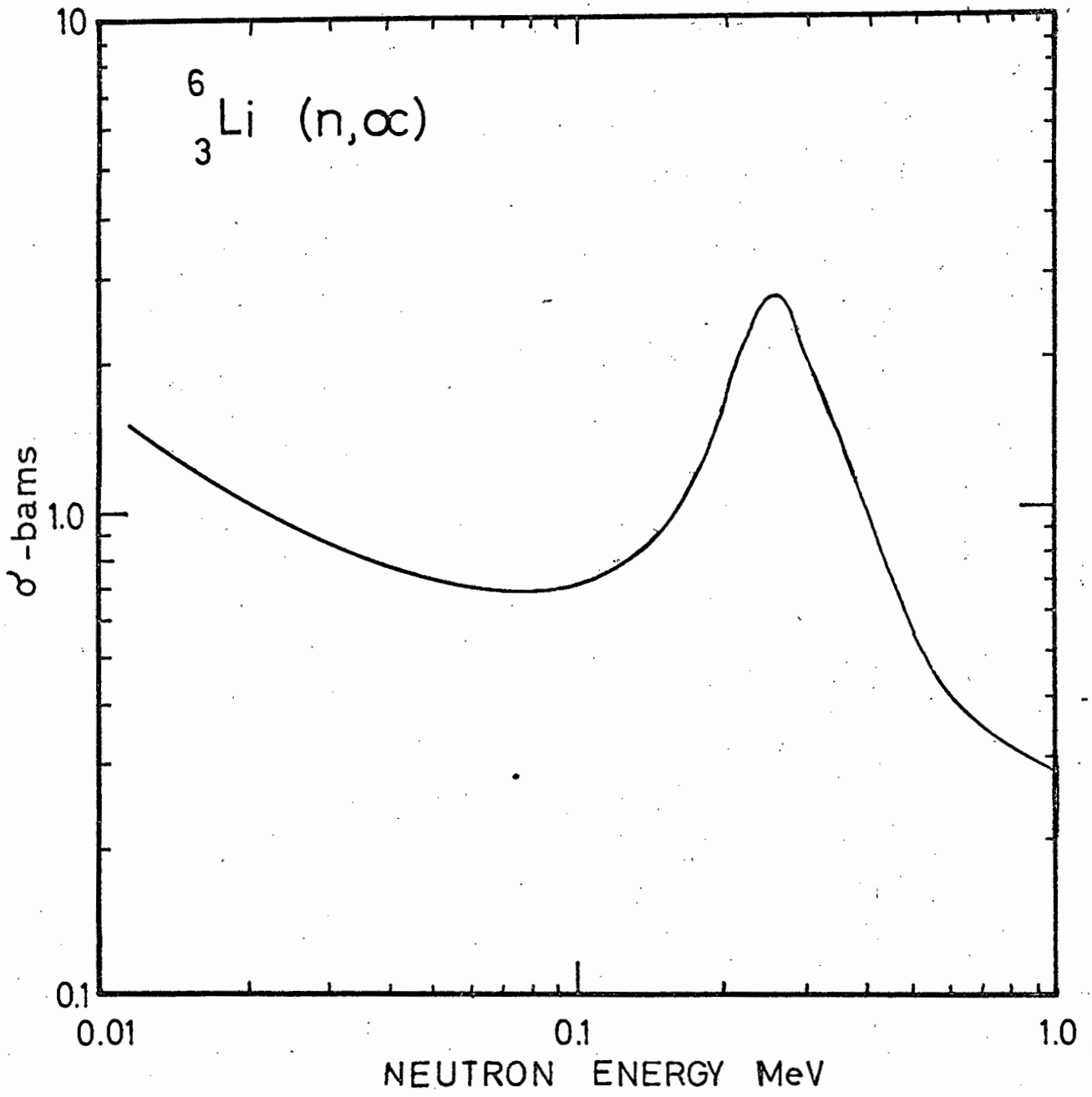

FIG 3·5 Cross section for (n,α) reaction in ^{6}Li glass

in Chapter 2.1. Values for the ^{6}Li (n,α) cross section, $\sigma_{\alpha}(E)$ were taken from BNL 325 (Fig. 3.5). The cross section data, $\sigma_{n'}(E)$, were obtained by applying equation 3.4. as described in section 3.3.

3.2.3 Thick Target Method

In this method the proton energy and lithium target thickness were chosen to give neutrons with an energy spectrum varying smoothly from 10 to 150 keV. The detector configuration and the electronics were the same as was used for the thin target work (Fig. 3.1). Flight paths varied from 20 to 50 cm. The time-of-flight spectra obtained for the ^{6}Li-glass and the NaI crystal are shown in figures 3.6a and b respectively. A problem associated with the thick target method was estimating the background contribution in the time spectra. Estimates of "background" time spectra were made (i) with a window set off the peak in Li glass and NaI pulse height spectra respectively, and (ii) using a "black filter"technique with aluminium (5.2 cm thick) and sulphur (14.0 cm thick) respectively as absorbers in the neutron beam. Both have resonances in the energy region of interest but this method proved unsuccessful because of poor energy resolution. See Fig. 3.6a.

The thick target method allows the determination of a set of ratios, N_2/N_1 defined in the previous section as a function of the neutron time-of-flight, from a single pair of spectra.

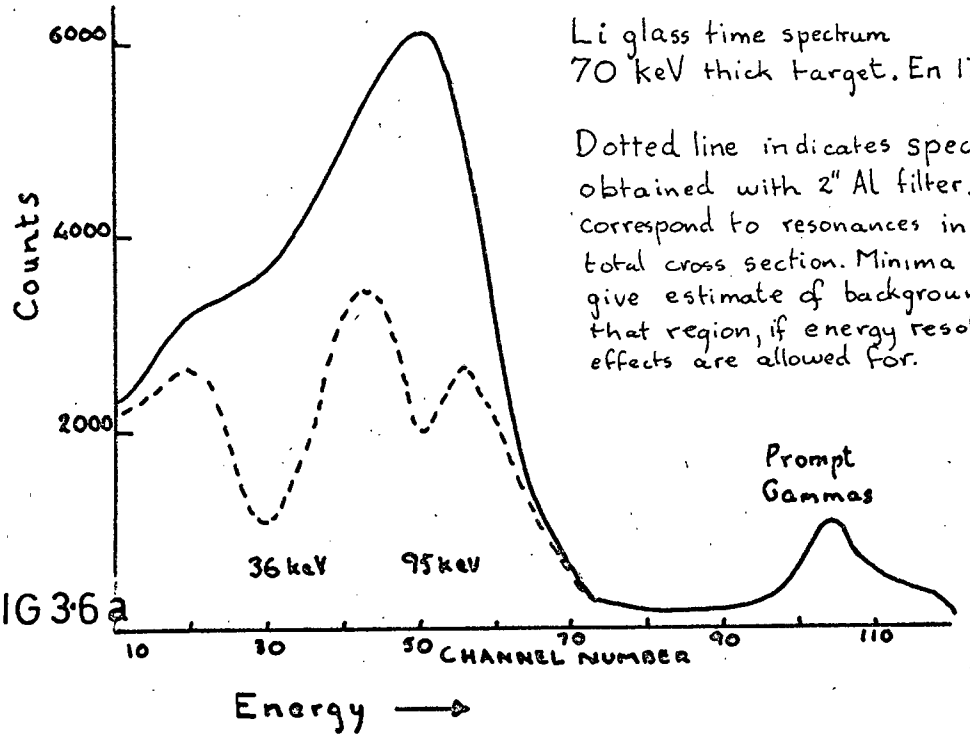

Li glass time spectrum
70 keV thick target. En 130kev(max)

Dotted line indicates spectrum obtained with 2" Al filter. The dips correspond to resonances in Al neutron total cross section. Minima of dips give estimate of background in that region, if energy resolution effects are allowed for.

FIG 3·6a

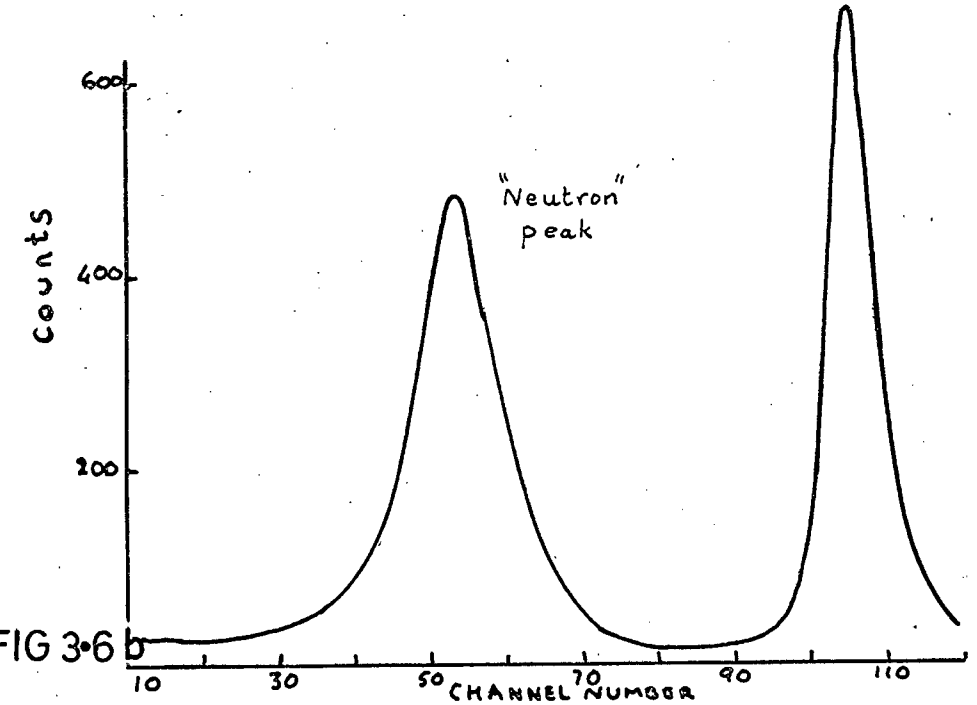

FIG 3·6b

NaI crystal time spectrum; thick target.

By applying equation 3.5 and in addition converting time-of-flight to energy $\sigma_{n'}(E)$ may in principle be determined in one run over the neutron energy range defined by the target thickness. (Fig. 2.1.)

In the present measurements however background problems and neutron energy resolution constituted a serious limitation. The energy resolution ΔE_n is given as a function of neutron energy E in Fig. 2.3. This is also indicated in the relative cross section data obtained using a thick target. (Fig. 3.7) Because of this limitation the thick target method was abandoned in favour of the thin target method.

3.3 Reduction of Data

3.3.1 Area Measurements

Determination of the area N_1 for the Li glass is straightforward; as is N_2 for NaI at intermediate energies. In both cases the background subtracted is that shown in Fig. 3.3a and b. For the NaI time spectrum at higher energies ($\geq$ 200 keV) the "neutron" peak and prompt gamma peak tended to overlap because of the inadequate time resolution of the system. (Fig. 2.3). At first, calculations were undertaken, assuming symmetry for the two peaks, using their half areas. The equations used were

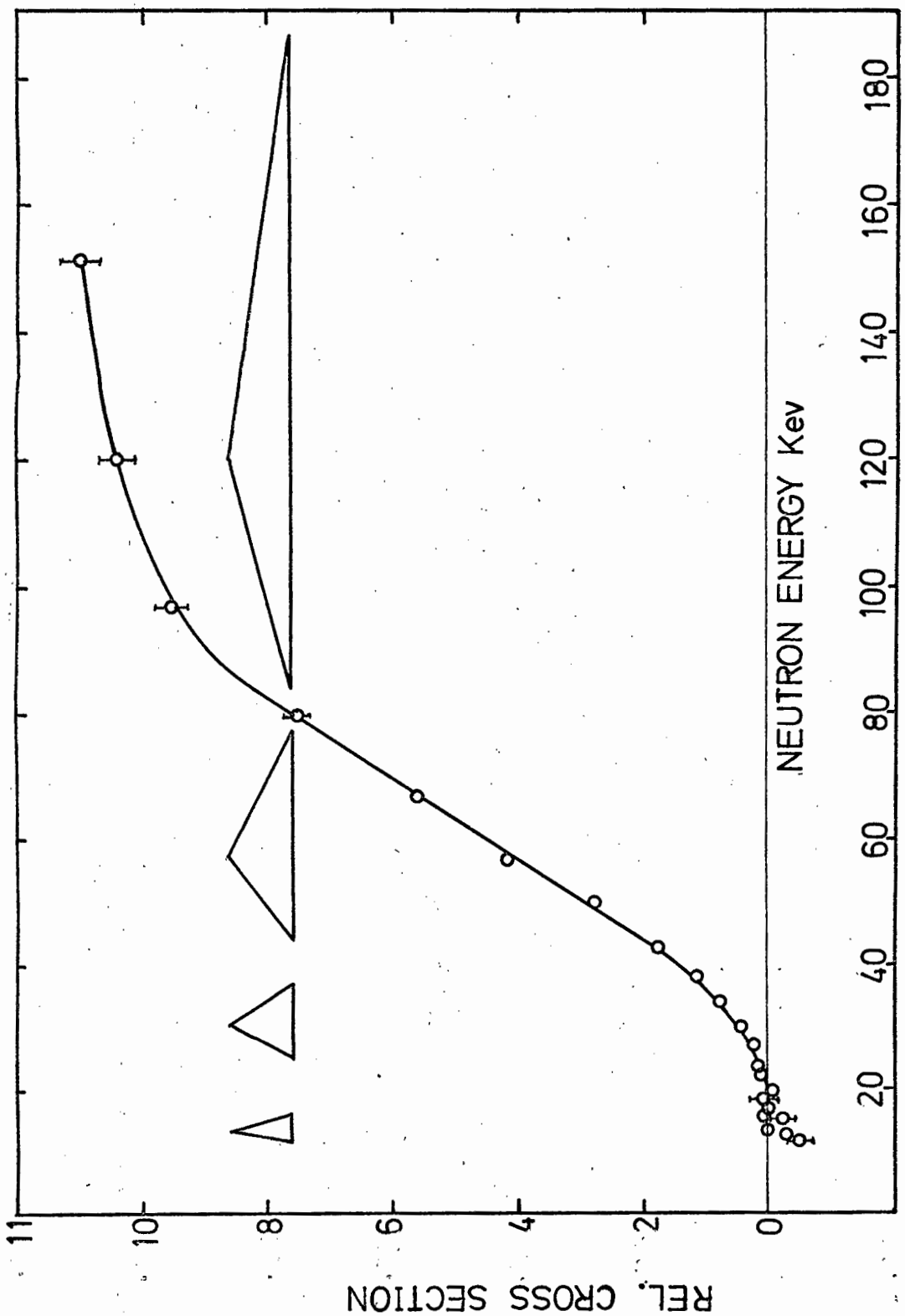

FIG 3·7 Results of measurements on 59keV level of ^{127}I using the thick target method.

$$\Delta = A_T - 2(A_1 + A_2) \qquad (3.6a)$$

and

$$A_1' = 2A_1 + \Delta/2 \qquad (3.6b)$$

where Δ is an assymmetry factor. See Fig. 3.8 for details. It was found however that the area defined as A_3 in Fig.3.8 had approximately the same value as that from calculations and equation 3.6a and b were therefore bypassed in determination of N_2. ie $A_3 = N_2$

3.3.2 Corrections

(a) Correction for Neutron Capture Effects.

For any neutron energy, radiative capture can lead to pulses appearing in the gate set on the 59 keV peak in the NaI pulse height spectrum. For high neutron energies the effect of this will be small compared with contribution from inelastic scattering because (i) capture cross section is less than inelastic cross section; (ii) efficiency for detecting high energy capture gamma rays will be small in the thin scintillator used; and (iii) very few gammas thus detected will produce pulses in the 59 keV gate.

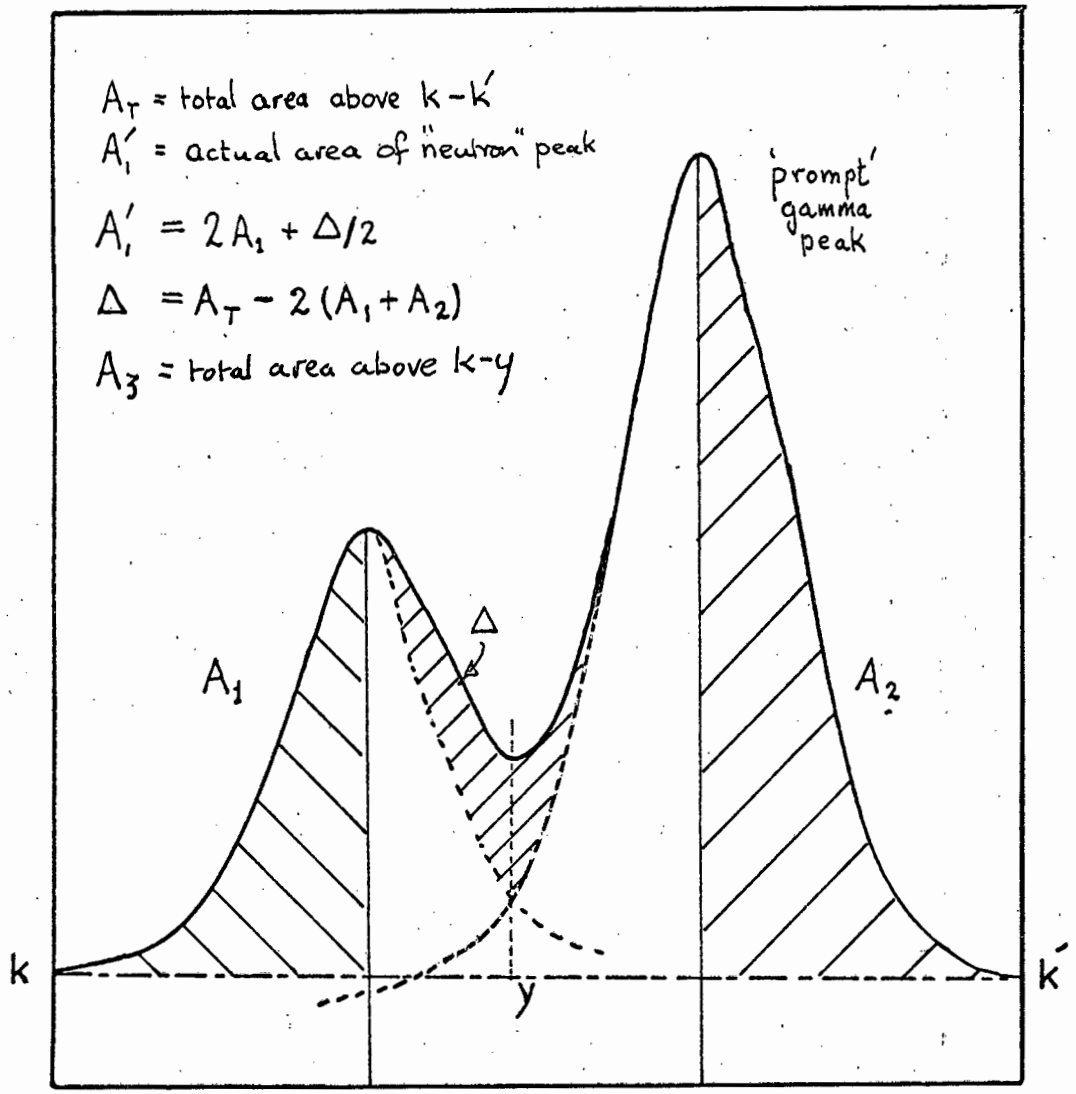

FIG 3·8 Area determination in NaI time spectrum at high energies

$N_2 = A_1' \simeq A_3$

As the energy decreases, to the inelastic scattering threshold however the effect can be appreciable because:-

(i) inelastic scattering cross section decreases whereas capture cross section increases

(ii) the energy resolution for "thin target" measurements deteriorates (see Fig. 2.3) so that it becomes more difficult to resolve contributions from the high and low energy neutron groups characteristic of the $^{7}Li(p,n)$ source (see Fig. 2.1).

A correction has therefore been made for the contribution of neutron capture to the "apparent inelastic scattering cross sections" measured in this experiment. In making these corrections it is assumed

(a) that the apparent inelastic cross section observed at energies less than the inelastic threshold (59 keV) represents the capture contribution at these energies.

(b) that the capture contribution is proportional to the neutron capture cross section (Go66) at higher energies.

As can be deduced from table III, showing the inelastic scattering results the capture correction is about 30% at 70 keV and drops off rapidly with increasing neutron energy to about 1% at 360 keV.

(b) Correction, ϕ, for self-screening and multiple scattering.

In section 3.2.2 we noted that a factor ϕ must be included in equation 3.5 (for the cross section, $\sigma_{n'}$) to account for the effects of multiple scattering and self-screening of the incident neutrons in both the glass and sodium iodide scintillators. In this section we consider both these corrections.

In its passage through either the glass or the sodium iodide scintillator, the incident neutron intensity is reduced as nuclear reactions remove neutrons from the incident beam. In other words, nuclei in the front of each scintillator "screen" the nuclei behind them, and N_1 and N_2 are reduced below the values they would have if there were no screening. On the other hand some of the incident neutrons may be scattered once, twice or many times in the scintillators so that their paths within the scintillator are longer than the scintillator thickness. For these neutrons the chance of causing an (n,α) or $(n\ n')$ reaction (in the glass or NaI respectively) is larger, hence N_1 and N_2 are increased relative to the value they would have if there were no scattering.

In order to take approximate account of these effects as they apply in the lithium glass and sodium iodide we express the factors ϕ_1 and ϕ_2 in equations 3.1 and 3.2 respectively as follows:

$$\phi_1 = \frac{\phi_1'}{\phi_1''} \qquad (3.7)$$

$$\phi_2 = \frac{\phi_2'}{\phi_2''} \qquad (3.8)$$

where ϕ_1' and ϕ_2' are the self-screening correction factors and ϕ_1'' and ϕ_2'' are the multiple-scattering correction factors. Details as to how these factors have been calculated are given in appendix 1A. The results of the calculation for the lithium-glass are shown in figure A.3. The sodium iodide crystal approximately fulfilled the "thin scintillator condition" (of section 3.2.2), leading as shown in appendix 1A to a value $\phi_2 = 1.04 \pm 0.01$ over the full energy range (60 to 360 keV) of these measurements.

Thus in the calculation of σ_n' from equation 3.5 the final correction, ϕ, for self-screening and multiple scattering was taken to be given by:

$$\phi = 0.96\ \phi_1 \qquad (3.9)$$

where ϕ_1 was read from figure A.3.

3.3.3 Results

In the evaluation of the apparent (i.e. excluding capture correction) inelastic scattering cross section, σ_n', from equation 3.5 the following data have been used:

$$\phi_2 = \frac{\phi_2'}{\phi_2''} \qquad (3.8)$$

where ϕ_1' and ϕ_2' are the self-screening correction factors and ϕ_1'' and ϕ_2'' are the multiple-scattering correction factors. Details as to how these factors have been calculated are given in appendix 1A. The results of the calculation for the lithium-glass are shown in figure A.3. The sodium iodide crystal approximately fulfilled the "thin scintillator condition" (of section 3.2.2), leading as shown in appendix 1A to a value $\phi_2 = 1.04 \pm 0.01$ over the full energy range (60 to 360 keV) of these measurements.

Thus in the calculation of $\sigma_{n'}$ from equation 3.5 the final correction, ϕ, for self-screening and multiple scattering was taken to be given by:

$$\phi = 0.96\ \phi_1 \qquad (3.9)$$

where ϕ_1 was read from figure A.3.

3.3.3 Results

In the evaluation of the apparent (i.e. excluding capture correction) inelastic scattering cross section, $\sigma_{n'}$, from equation 3.5 the following data have been used:

(a) the constants

$\alpha_1 = 11.44\ cm^2$

$\alpha_2 = 7.93\ cm^2$

$n_1 = 0.023$ atoms/barn

$n_2 = 0.0024$ atoms/barn

$f = 0.97$

Thus $\frac{\alpha_1 n_1}{\alpha_2 f n_2} = 14.24$

(b) the experimental values of N_2/N_1

(c) the multiple scattering factor ϕ.

(d) values of the cross section for $^6Li(n\alpha)$ reaction obtained from BNL-325 (Hu58), fig. 3.5.

Data (b), (c) and (d) are listed in Table III-1 in columns 2, 3 and 4 respectively for each neutron energy (column 1) studied. Column 5 shows the apparent inelastic scattering cross section calculated from equation 3.5.

The assumed neutron capture contributions to the apparent inelastic cross section data calculation as described in section 3.3.2(a), are listed in column 6 and the final cross section data are given in column 7.

The errors quoted in the observed cross section in column 7, include contributions from the following:

1) Statistical errors which are larger $\sim$ 10% near threshold because of the smaller peak to background ratio in that region, and falling to an average of 4% at higher energies.

Table III-1 Corrections and Final Cross Section Data.

Neutron Energy keV	$\frac{N_2}{N_1}$	ϕ	Cross Section (mb)			
			σ_α	Appt. inel.	n,γ contrib.	$\sigma_{n'}$
46±12	0.0030	1.300	760	40	40	0 ± 7
61±7	0.0036	1.290	700	43	33	10 ± 8
61±7	0.0048	1.290	700	58	33	25 ± 8
70±6	0.0101	1.285	690	120	31	89 ± 25
77±6	0.0158	1.280	680	184	29	155 ± 35
85±5	0.0266	1.280	680	309	27	282 ± 43
96±5	0.0298	1.280	700	366	25	341 ± 50
106±5	0.0327	1.280	720	402	23	379 ± 54
121±4	0.0427	1.290	770	566	21	545 ± 63
121±4	0.0428	1.290	770	567	21	546 ± 63
152±4	0.0436	1.320	930	714	18	696 ± 75
152±4	0.0411	1.320	930	673	18	655 ± 75
180±3	0.0326	1.420	1200	741	16	723 ± 85
205±3	0.0215	1.490	1750	748	15	733 ± 92
218±3	0.0184	1.460	2100	753	14	767 ± 96
230±3	0.0172	1.430	2400	787	14	773 ±100
268±2	0.0168	1.385	2750	854	13	841 ±110
293±2	0.0196	1.375	2340	841	12	829 ±115
340±2	0.0383	1.380	1550	1093	11	1082 ±125
362±2	0.0419	1.400	1340	1049	11	1038 ±130

2) the (n,α) cross section, error ∿ 5%

3) self screening, multiple scattering correction factor, estimated error ∿10%.

4) the "capture" cross section correction ∿10% error in assumed contribution.

Strictly speaking error contributions from the following should be included, but they were considered to be negligibly small, compared with the other errors; angle subtended by the two detectors about the $\theta = 0^{o}$ line, drifts in the electronics associated with individual detectors, and the efficiency of the sodium iodide detector.

3.4 Discussion

The cross section data, $\sigma_{n'}(E)$, (Table III-1) are plotted versus energy in figure 3.10. Data obtained by Guernsey and Wattenburg (Gu56) and van Loef and Lind (Va56) are also shown in this figure. These data were obtained by the same method as used in this work i.e. sodium iodide crystal as both sample and detector, but without the aid of time-of-flight. Guernsey (Gu56) used a small (∿ 1 mm thick) crystal while van Loef and Lind (Va56) used a crystal 4.4 cm diameter × 5 cm thick.

It will be seen from Fig. 3.10 that the three sets of data are in approximate qualitative agreement with respect to the shape of the excitation function. However the present data are higher than other two sets by a factor of about 5. We

should note in particular that the detection efficiency for 59 keV de-excitation radiations is about unity in all the measurements, hence this cannot be the cause of the discrepancy. The neutron flux measurement appears to be the most likely cause for this discrepancy. Guernsey (Gu56) used a long counter for the flux measurement assuming Hansen and McKibben (Ha47) values for the efficiency calibration. van Loef and Lind used a ZnS-Lucite button, which, in turn, was calibrated with respect to a long counter. In their case the long counter efficiency was determined with respect to a calibrated Ra-Be source. In the present measurements we note that the flux calibration is based on ^{6}Li (n,α) cross section data (Hu58) and on calculations of self-screening and multiple scattering corrections, as outlined in section 3.3.2b.

The large discrepancy in Fig. 3.10 is disturbing and it might be useful to add other independent data to the comparison in order to investigate it further. It should be noted at this point that this experiment measures the total cross section for population of the 59 keV state by inelastic scattering. For neutron energies up to 203 keV this cross section corresponds to the cross section for inelastic scattering to the 59 keV state. At higher energies the observed cross section may be enhanced by inelastic scattering to the 203 keV or higher states which may decay via 59 keV state.

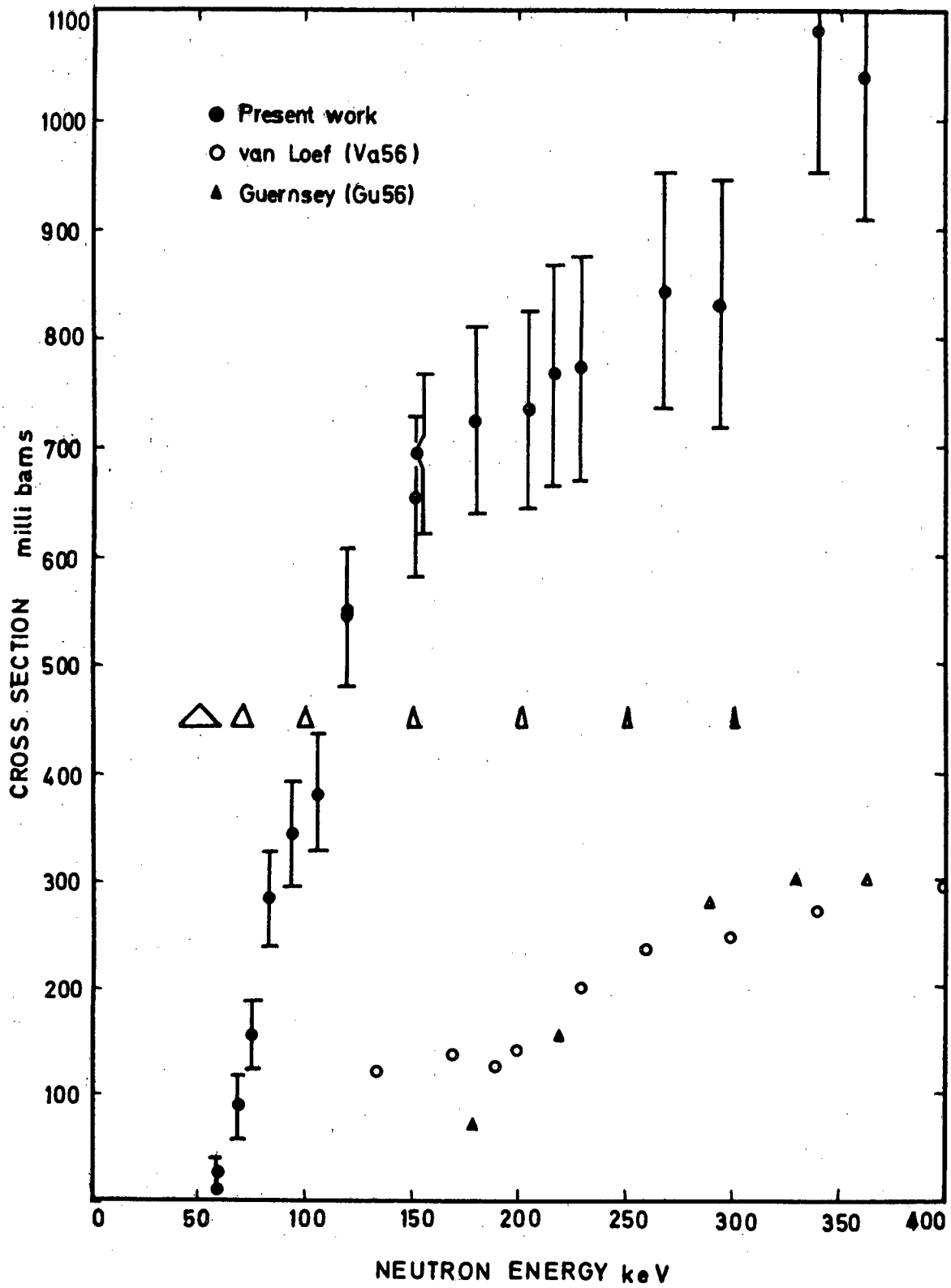

FIG 3·10 Data obtained for Inelastic excitation of ^{127}I 59 keV level

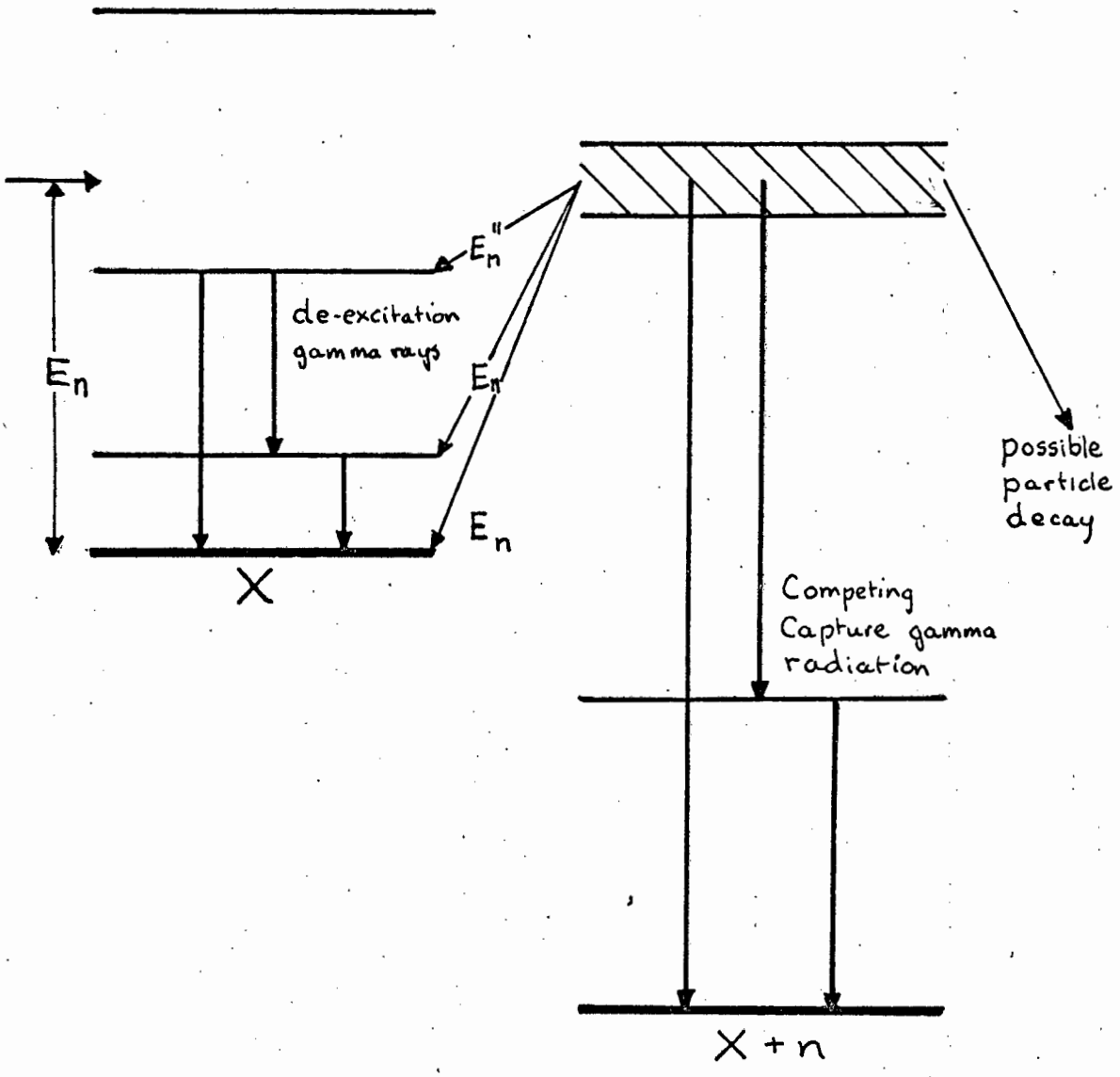

Fig 4·1 Compound nucleus model for neutron inelastic scattering

4. HAUSER-FESHBACH CALCULATIONS

There is much good evidence (e.g. Bl52,Cr63b) in support of the interpretation that neutron inelastic scattering occurs predominantly by way of a compound nucleus mechanism. Hauser and Feshbach (Ha52) developed a statistical model for the calculation of inelastic scattering cross sections on this basis. Various sophistications and elaborations (e.g. Mo61, Mo63,Sa63) of the Hauser-Feshbach model have been suggested from time to time. A fairly recent example is that of Auerbach and Moore (Au64) who have used a local, spherical, spin-dependent optical potential in their calculations. In this chapter we describe the methods we have used to calculate theoretical total inelastic scattering cross sections for the 59 and 203 keV levels of ^{127}I. These calculations have been made with a view to interpreting the data measured as described in Chapter 3. The methods used are essentially a direct adaptation of those suggested by Auerbach and Moore. (Au64).

4.1 Calculation of Total Inelastic Cross Sections

Auerbach and Moore (Au64) have given the following equation for $\sigma(E,E')$, the inelastic scattering cross section for neutrons of incident energy E, and emergent energy E'. (see Fig. 4.1)

$$\sigma(E,E') = \frac{\pi\lambda\!\!\!^{-2}}{2(2I_o+1)} \sum_{j\ell} T_{\ell j}(E) \times \sum_{J}(2J+1) \cdot \frac{\sum_{j'\ell'} T_{\ell' j'}(E')}{\sum_{pj''\ell''} T_{\ell'' j''}(E'')} \qquad (4.1)$$

where λ is the wavelength of the incident neutron in the neutron nucleus system; $\lambda\!\!\!^{-} = \lambda/2\pi$

I_o is the total angular momentum (spin) of the target nucleus;

j, j' and j'' are channel spins for ingoing or outgoing neutrons of energies E, E' and E'' respectively.

ℓ, ℓ' and ℓ'' are orbital angular momentum quantum numbers which satisfy relations of the type

$$\ell = j \pm \tfrac{1}{2} \qquad (4.2)$$

$T_{\ell j}(E)$ is the transmission coefficient for neutrons of spins, ℓj, and energy, E, and likewise for $T_{\ell' j'}(E')$ etc.

J is the spin of the compound nucleus state which forms and decays in the process of inelastic scattering.

J takes on all values consistent with the conservation of angular momentum hence J, j, j' and j'' satisfy the relations:-

$$\begin{aligned} |I_o - j| &\leq J \leq (I_o + j), \\ |J - I_q| &\leq j' \leq (J + I_q), \\ |J - I_p| &\leq j'' \leq (J + I_p) \end{aligned} \qquad (4.3)$$

where I_q is the spin of the state E_q, reached by outgoing neutrons of energy E' and channel spin j' and I_p is the spin of the state E_p, reached by outgoing neutrons of energy E" and channel spin j".

In addition, to conserve parity, ℓ, ℓ' and ℓ'' satisfy the relations:-

$$\begin{aligned} (-1)^{\ell'}\pi_q &= (-1)^{\ell}\pi_o \\ (-1)^{\ell''}\pi_p &= (-1)^{\ell}\pi_o \end{aligned} \qquad (4.4)$$

where π_o, π_q and π_p are the parities of the target nucleus ground state and the excited states at E_q and E_p respectively.

In equation 4.1 the total inelastic cross section $\sigma(E,E')$ is expressed as the sum of the cross sections for all allowed modes of compound nucleus formation, with the cross section for each mode reduced by the probability of compound nucleus decay by the channel j', leading to the final state, E_q, I_q, π_q. In calculating the latter probabilities the sum term in the denominator of equation 4.1 must be summed over all final states, p, which are energetically accessible (including both E_q and the ground state of the final (i.e. target) nucleus.

The calculation of $\sigma(E,E')$ therefore depends on:

(a) the energies, spins and parities assumed for the relevant states of the target nucleus;

and (b) the transmission coefficients $T_{\ell j}(E)$, $T_{\ell' j'}(E')$, $T_{\ell'' j''}(E'')$.

4.2 Transmission Coefficients

The transmission coefficients used in Hauser-Feshbach calculations are defined by the equation:-

$$T_{\ell j}(E) = 1 - |\eta_{\ell j}(E)|^2 \qquad (4.5)$$

where

$$\eta_{\ell j}(E) = \exp.(2i\delta_{\ell j}(E)) \qquad (4.6)$$

and $\delta_{\ell j}(E)$ is the phase shift obtained by solution of the Schrödinger Equation with appropriate complex optical potential.

The procedure often adopted in Hauser-Feshbach calculations (see e.g. Au64) is to determine optical model parameters, and by adjustment to obtain a fit to total elastic and differential elastic scattering cross section data. Solution of the Schrödinger equation using these parameters follows, and hence $\eta_{\ell j}(E)$ and $T_{\ell j}(E)$ are obtained. This method is particularly suitable in situations where the elastic scattering is measured together with the inelastic scattering cross section, e.g. where the scattered neutrons are detected by time-of-flight.

For methods and situations like the present where no elastic data are taken and a large computer is not readily available a useful alternative is possible however. This is to use the transmission coefficients tabulated by Auerbach and Perey (Au62). These coefficients have been determined by making "global fits" to the elastic data. Two fits have been made for each mass number considered; these fits are based on the

potential forms of Bjorklund and Fernbach (Bj58) and Perey and Buck (Pe62) respectively. The transmission data quoted (Au62) from calculations based on fits to these two potential forms are plotted as points in Figures 4.2 and 4.3 respectively (for the mass number 128, in the energy range 100 to 800 keV).

4.3 Analytical Fitting of Transmission Coefficient Data

Analytical fits were made to the transmission coefficient data shown in Figures 4.2 and 4.3. This was done in order to facilitate calculation of inelastic scattering cross sections by means of the University of Cape Town ICT 1301 computer. The immediate purposes of this fitting were twofold:

1) to allow rapid interpolation to energies between the tabulated values;
2) to extrapolate the transmission coefficient data to energies below 100 keV and 200 keV, the lowest energies for which "Bjorklund-Fernbach" and "Perey-Buck" values respectively, were tabulated. (It was fully realised that this extrapolation procedure carried with it very real inherent dangers of inaccuracy).

A generalized power law was used as the basic analytical form for the fitting, viz.

$$\log (T + a_o) = a_1 \log (E + a_2) + a_3$$

$$\text{or} \quad T = -a_o + \exp. \{a_1 \log (E + a_2) - a_3\} \qquad (4.7)$$

Thus for each ℓ_j combination (for $\ell \leq 2$) a set of values was determined for the parameters a_o to a_3, such that substitution in equation 4.7 reproduced the appropriate tabulated values of $T_{\ell j}$. In the case of the $\ell = o$ coefficients extrapolation to energies below 100 keV was aided by the knowledge the $T_{o,\frac{1}{2}}$ must approach the value $4R^2/\lambda^2$ at low energies. The line corresponding to this limit is shown (dashed) in both Figures 4.2 and 4.3. In the case of the $\ell = 1$ coefficients for the Bjorklund-Fernbach values, two independent fits were made, each giving a different behaviour in the extrapolation (< 100 keV) region. Similarly the Perey-Buck values were fitted using different sets of coefficients (Fig. 4.3). This was done in order to test the sensitivity of the cross section calculation to extrapolation errors (see section 4.5).

Transmission coefficient values calculated from the final analytical fits are shown as lines in Figures 4.2 and 4.3 respectively. The parameters a_o to a_3 used in these calculations are listed in Table IV.1. The optical model parameters on which the tabulated $T_{\ell j}$ values are based are listed in Table IV.2.

Table IV - 1

Parameters for the analytic function fitted to the transmission coefficients.

BJORKLUND and FERNBACH (fig.4.2)

		(a)					(b)				
ℓ	j	Curve	a_o	a_1	a_2	a_3	Curve	a_o	a_1	a_2	a_3
0	1/2	B1	0.20	0.255	0	1.87	B1	0.20	0.255	0	1.87
1	1/2	B2a	0.01	0.836	-10	-6.41	B2b	0.10	0.520	0	-4.24
1	3/2	B3a	0.01	0.862	-10	-6.87	B3b	0.07	0.510	0	-4.55
2	3/2	B4	0.00	2.487	0	-18.59	B4	0.00	2.457	0	-18.59
2	5/2	B5	0.00	2.460	0	-17.40	B5	0.00	2.460	0	-17.40

PEREY and BUCK (fig.4.3)

		(a)					(b)				
ℓ	j	Curve	a_o	a_1	a_2	a_3	Curve	a_o	a_1	a_2	a_3
0	1/2	P1a	0.00	0.340	-10	-2.83	P1b	0.00	0.340	0	-2.53
1	1/2	P2a	0.25	0.395	20	-2.90	P2b	0.25	0.395	0	-2.94
1	3/2	P3a	0.24	0.403	20	-3.10	P3b	0.24	0.403	0	-3.11
2	3/2	P4a	0.00	2.320	0	-17.40	P4b	0.00	2.320	0	-17.40
2	5/2	P5a	0.00	2.260	0	-16.62	P5b	0.00	2.260	0	-16.620

Table IV - 2.

OPTICAL MODEL PARAMETERS

Optical Potential	Real V_o(MeV)	Imaginary W_o(MeV)	Spin Orbit V_{so}(MeV)	Radius parameter r_o(f)	Wood-Saxon parameter a(f)	b(f)	Non local-ity β(f)
Local Bjorklund-Fernbach	50.0	7.0	9.5	1.25	0.65	0.98	-
NonLocal Perey-Buck	70.0	7.0	7.2	1.25	0.65	0.65	1.00

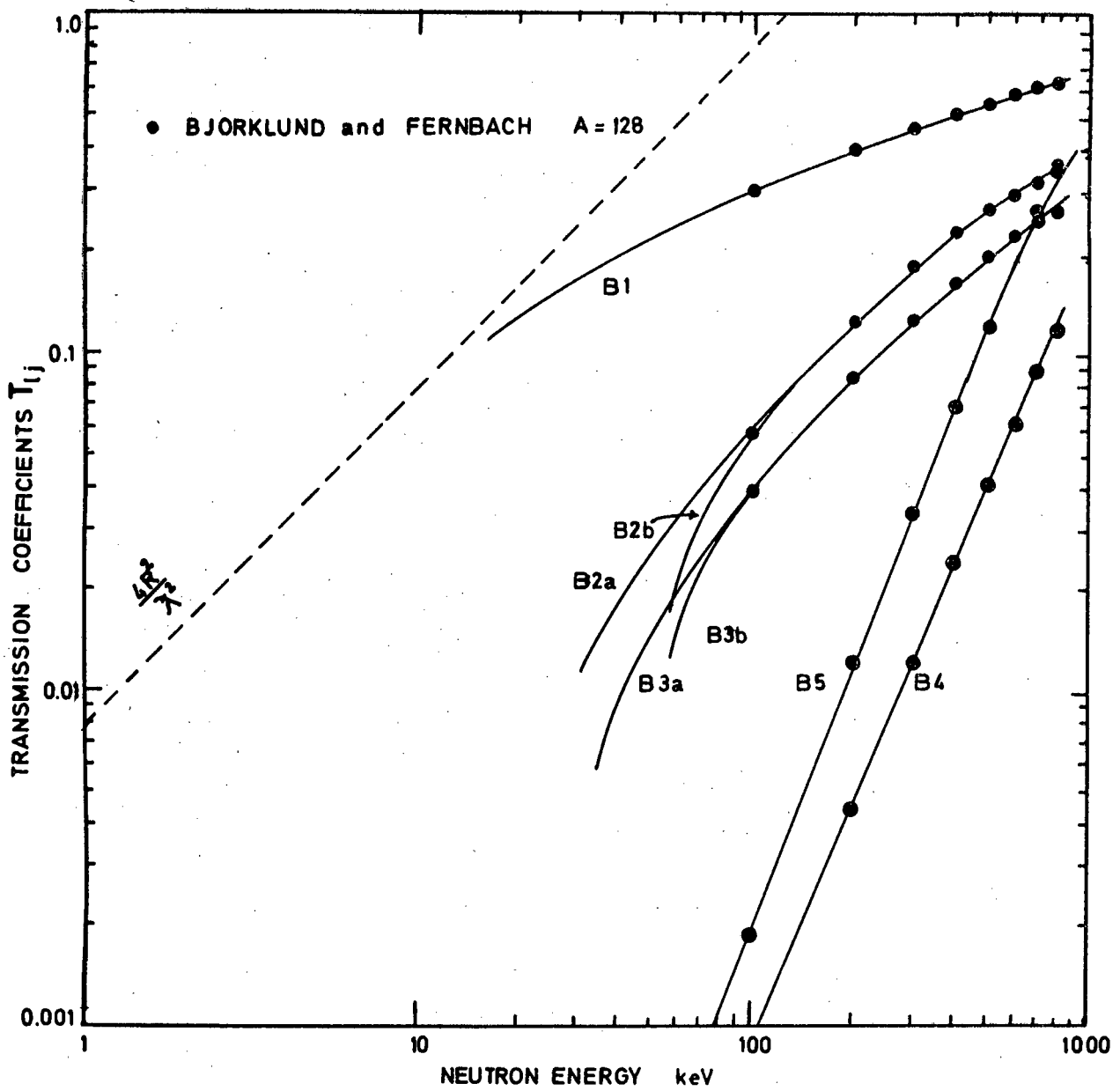

Fig. 4.2 Analytical fits to Bjorklund–Fernbach neutron transmission coefficients. The B–F tabulations extend to 100 keV. The extrapolated curve below 100 keV are based on values from Program 1 with parameters from Table IV. 2

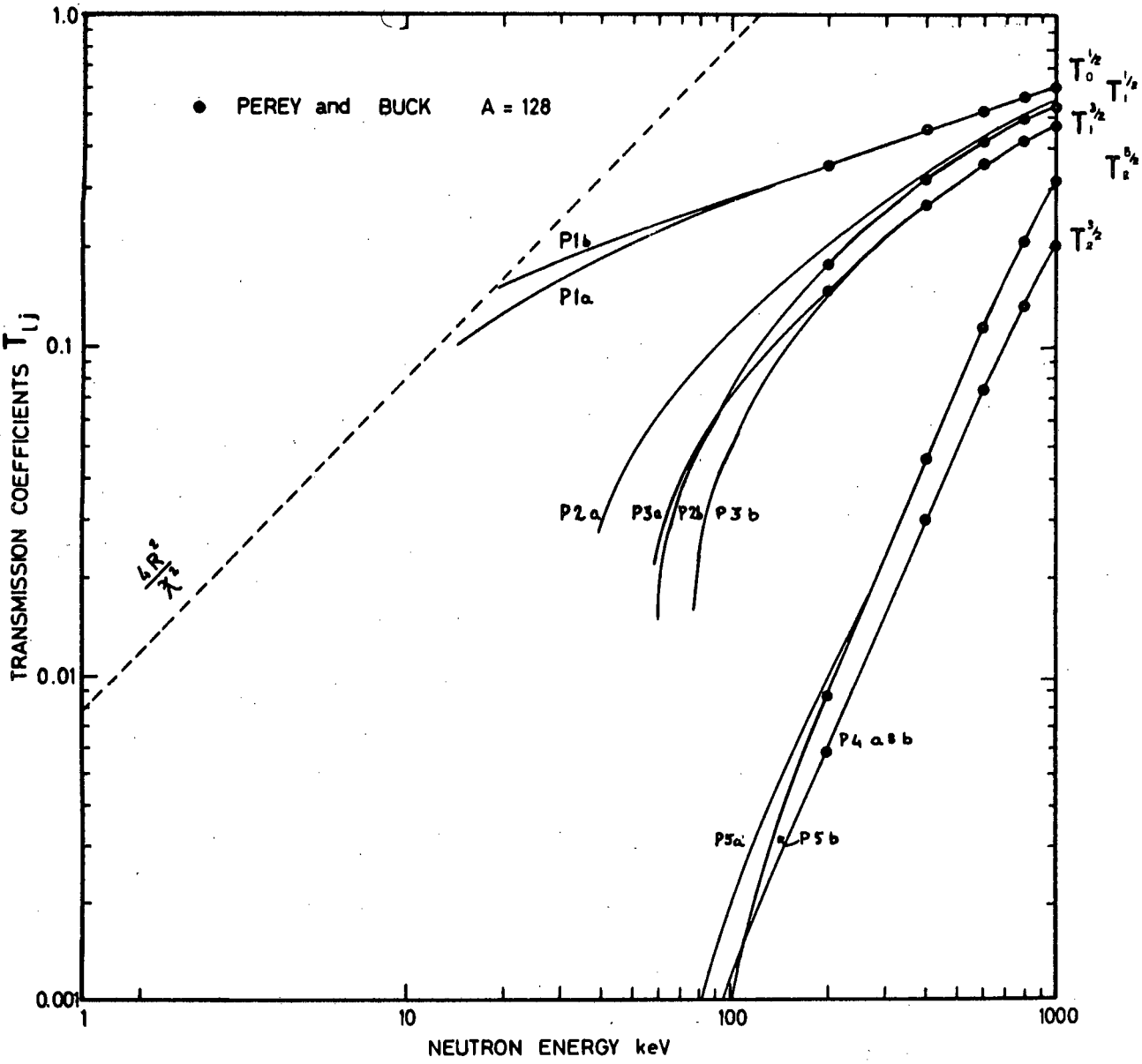

Fig. 4.3 Analytical fits to Perey-Buck neutron transmission coefficients. The P-B tabulations extend to 200 keV. The extrapolated curves below 200 keV are based on values using Program II with parameters from Table IV-2.

4.4 Computer Programs

Two computer programs were written for the I.C.T. 1301 computer. These programs were used respectively:

I) for calculation of $\sigma(E,E')$ as described in equation 4.1;

II) for checking the analytical fits (section 4.3) to the tabulated values of the transmission coefficients.

Listings of the two programs are given in appendix B and C respectively.

4.5 Calculations of $\sigma(E,E')$ for the 59 keV level

In order to illustrate and thereby gain a better understanding of the H-F theory a number of calculations have been made of the cross section for inelastic neutron scattering to the 59 keV level of ^{127}I. The calculations were made with the aid of computer program I (above) and for different values of: (a) the transmission coefficients $T_{\ell j}$ and; (b) the spins and parities of the ground 59 keV and 203 keV states of ^{127}I. The calculations were carried out at 20 keV intervals in the neutron energy range 60 to 400 keV, and took about half a minute of I.C.T. 1301 computer time per energy interval.

Figures 4.4, 4.5 and 4.6 show the results of the calculations and illustrate the dependence of $\sigma(E,E')$ on level spins, level parities and transmission coefficients respectively.

4.5.1 Dependence on Level Spins

Figure 4.4. shows the inelastic cross sections calculated using the "a"-fit to the Bjorklund-Fernbach transmission coefficients (Table IV.1) and assuming even parity for the ground, 59 keV 203 and 375 keV states. The calculation was performed for various arbitrarily chosen spin assignments, the values chosen for the respective states being indicated in units of $\frac{\hbar}{2}$ on the right hand side of the appropriate curve. (e.g. for curve A (5,7,3) indicates that spins of $\frac{5}{2}$, $\frac{7}{2}$ and $\frac{3}{2}$ were assumed for the ground 59 and 203 keV states respectively.) The value for 375 keV state $\frac{1}{2}^+$ was not varied, and is thus not indicated in the notation above. It is clearly seen in Fig. 4.4 that the theoretical predictions for the excitation function are very sensitive to spin change between the 59 keV and ground state. For spin changes of 0, 1 and 2 the value for the cross section at 200 keV is 100% (1045 millibarns), 77% and 41% respectively. Other systematics can easily be deduced from the figure, (4.4).

4.5.2 Dependence on parity

Figure 4.5 shows inelastic scattering cross sections calculated using the Bjorklund-Fernbach "a" parameters (Table IV-1) using different parity values for the ^{127}I levels. The spin values used were $\frac{5}{2}$ $\frac{7}{2}$ $\frac{3}{2}$ and $\frac{1}{2}$ for the ground and first

three excited states respectively, i.e. as for curve A Fig. 4.4. For no parity change between 59 keV and ground state the cross section is at first greater than when there is a parity change (i.e. over the energy range 80 to 160 keV) but becomes smaller at energies greater than approximately 230 keV. The differences are of the order of 6%, or in other words the dependence on parity assignments is small.

4.5.3 Dependence on Transmission Coefficients

Fig. 4.6 shows cross sections calculated using different analytic fits to the transmission coefficient data, namely that a and b fits to the Bjorklund-Fernbach data, and the a and b fits to the Perey-Buck data. (Table III-1). These calculations were made using the same spin assignments as in section 4.5.2 and even parity for all levels. The Perey and Buck excitation function gives values approximately 20% greater than the Bjorklund-Fernbach values. The dip at about 100 keV in the curves B and D arises from the sharp drop in $T_1^{\frac{1}{2}}$ and $T_1^{3/2}$ transmission coefficients at $\sim$ 70 keV (Figs. 4.2 and 4.3). This drop arises from the completely arbitrary method adopted in extrapolating the transmission coefficients to energies of less than 100 keV. The extrapolation based on the "a" fit to the Bjorklund-Fernbach data (Figure 4.2) is probably more realistic and has therefore been preferred to the "b" fit for most

calculations. However this comparison of the "a" and "b" fits serves to illustrate the sensitivity of the calculations to the fitting and extrapolation. Clearly any cross sections calculated for the ^{127}I 59 keV level for neutron energies less than 150 keV must be treated with extra caution.

In the following chapter the significance of these curves in relation to the experimental data obtained, is discussed.

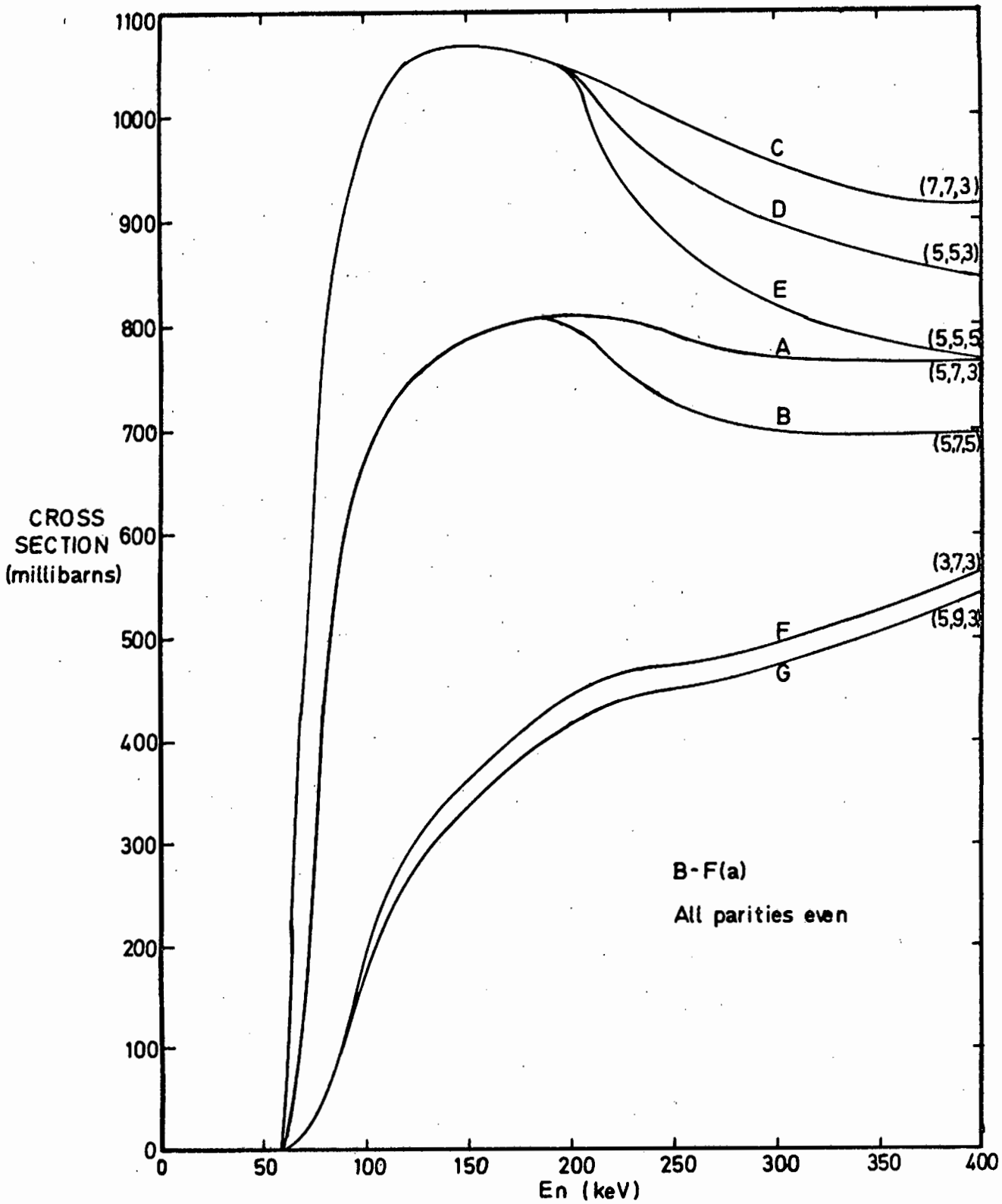

Fig. 44 Hauser-Feshbach excitation functions showing spin dependence

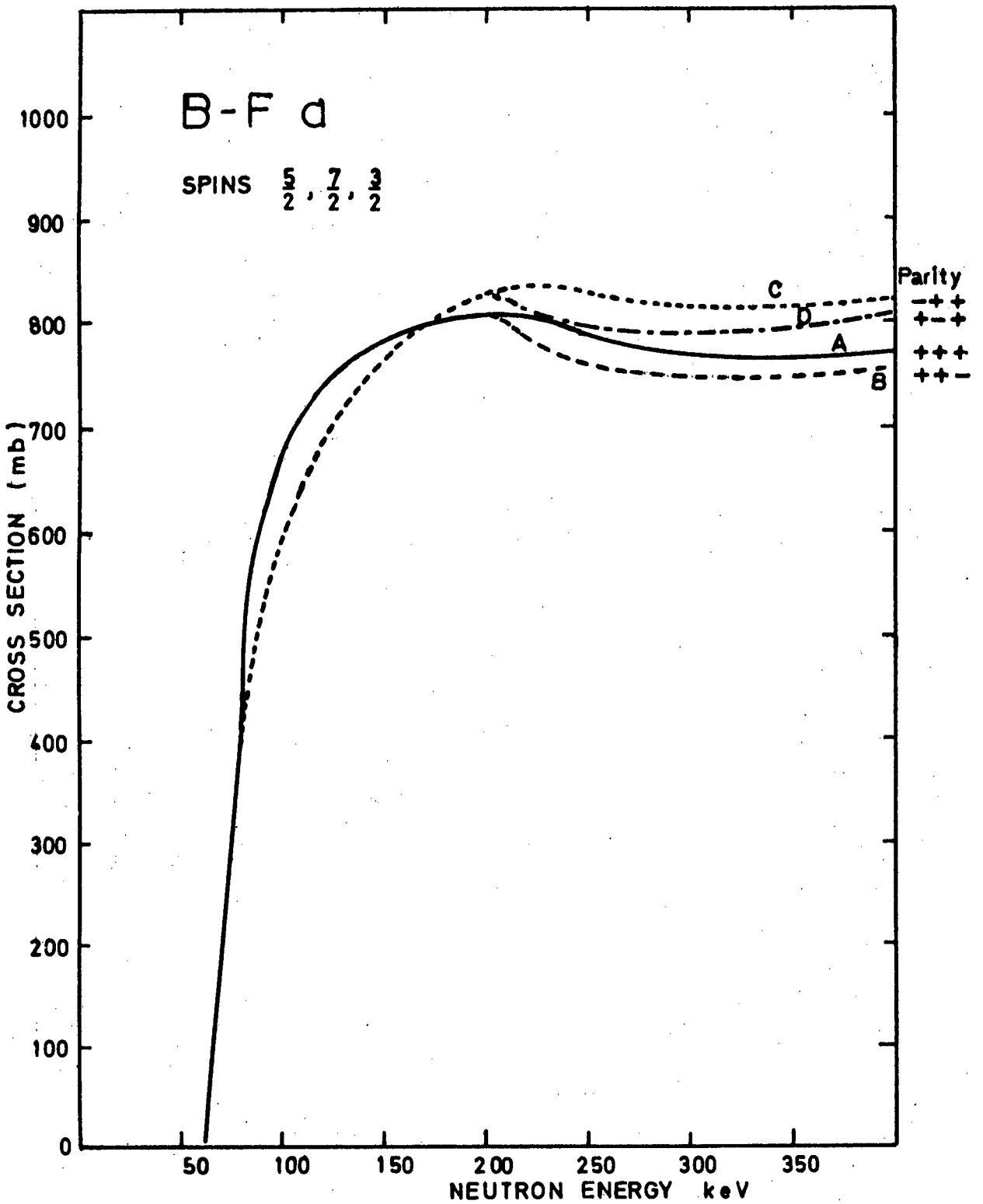

FIG 4.5 Hauser-Feshbach excitation-functions, parity dependence.

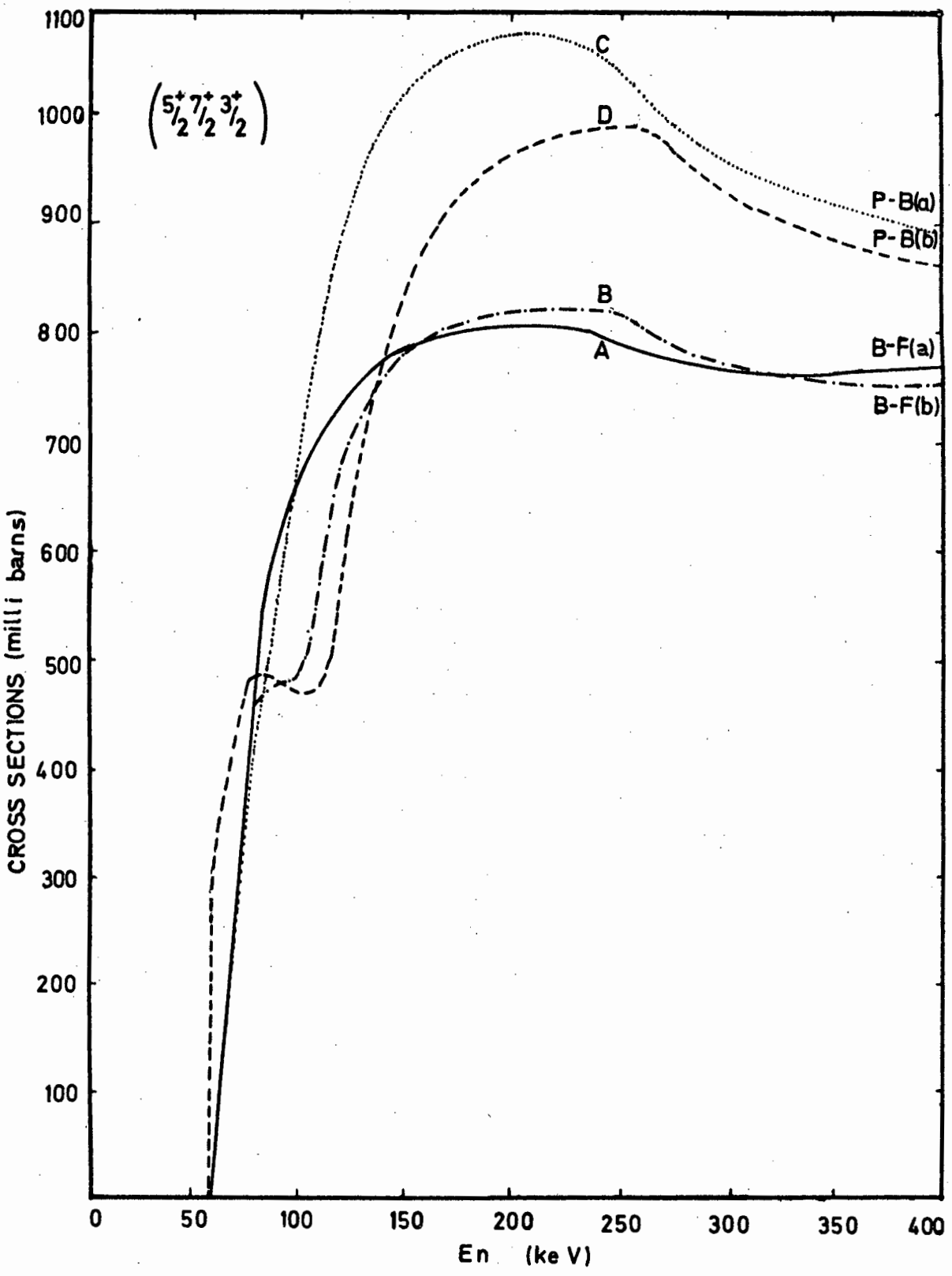

Fig 4.6 Hauser-Feshbach Excitation Function for different transmission coefficients

5. Discussion

5.1 Comparison between Hauser Feshbach theory and experiment

In this section we compare cross section data obtained from the experiment with the theoretical cross section calculated (Chapter 4) using Bjorklund-Feshbach transmission coefficients and the recommended values of spin and parity for ^{127}I (Wa61). Thus in Fig. 5.1 we show the experimental data and the theoretical excitation function where the latter has been reduced by a factor k, (0.9), to fit the experimental data in the 150 to 200 keV region. The first point to note is the agreement between data and theory in this energy region, which is evidenced by the factor k being of the order of unity.

To fit the data of Guernsey and Wattenburg (Gu56) or van Loef and Lind (Va56), using the same transmission coefficients would require either that $k \sim 0.16$ or that the spins of the ground and 59 keV states differed by 3 or more units (see section 4.5.1). Such a spin difference would mean that the lifetime for the 59 keV state should be of the order of seconds or more, in contradiction to experimentally measured values (Jh64,Ge65) of $\lesssim$ 3nS (which, incidentally, are confirmed, to $\lesssim$ 20 nS, by the fact that "neutron peaks" could be observed in the present time-of-flight technique). We conclude therefore that present σ_n, data permit a more consistent interpretation than do the data of Guernsey and Wattenburg (Gu56) or van Loef and Lind (Va56).

To accept the latter data and still explain the short lifetime either the Bjorkland and Fernbach transmission coefficients or the Hauser-Feshbach model must be modified considerably.

It should also be noted that use of the Perey and Buck transmission coefficients would increase the theoretical cross section even further (see section 4.5.3)

Turning to comparison (Fig. 5.1) of experimental and theoretical cross sections above 200 keV we note an increase in the experimental values above the theoretical cross section for inelastic scattering to the 59 keV level (curve a). This rise can be attributed to inelastic scattering to the 203 keV state in ^{127}I, followed by decay through the 59 keV level. The theoretical excitation function for the 203 keV level is shown by curve b. If a certain fraction of this is added to curve a, a curve c, lying closer to the data points above 200 keV is obtained. This fraction, $\sim$0.66 , would correspond to the branching probability for decay of the 203 keV state through the 59 keV state. Using this branching probability and the internal conversion coefficient 0.43 (Kn56,Wa61) for the 144 transition between 203 keV level and 59 keV level, together with the observed cross section data(Fig. 3.10) we expect a peak at 203 keV in the sodium iodide pulse height spectrum for inelastic scattering to the 203 keV level. However the fact that this peak was not observed in section 2.2.1 casts doubt on the values of branching probability and internal conversion coefficient.

The general validity of the Hauser-Feshbach theory has

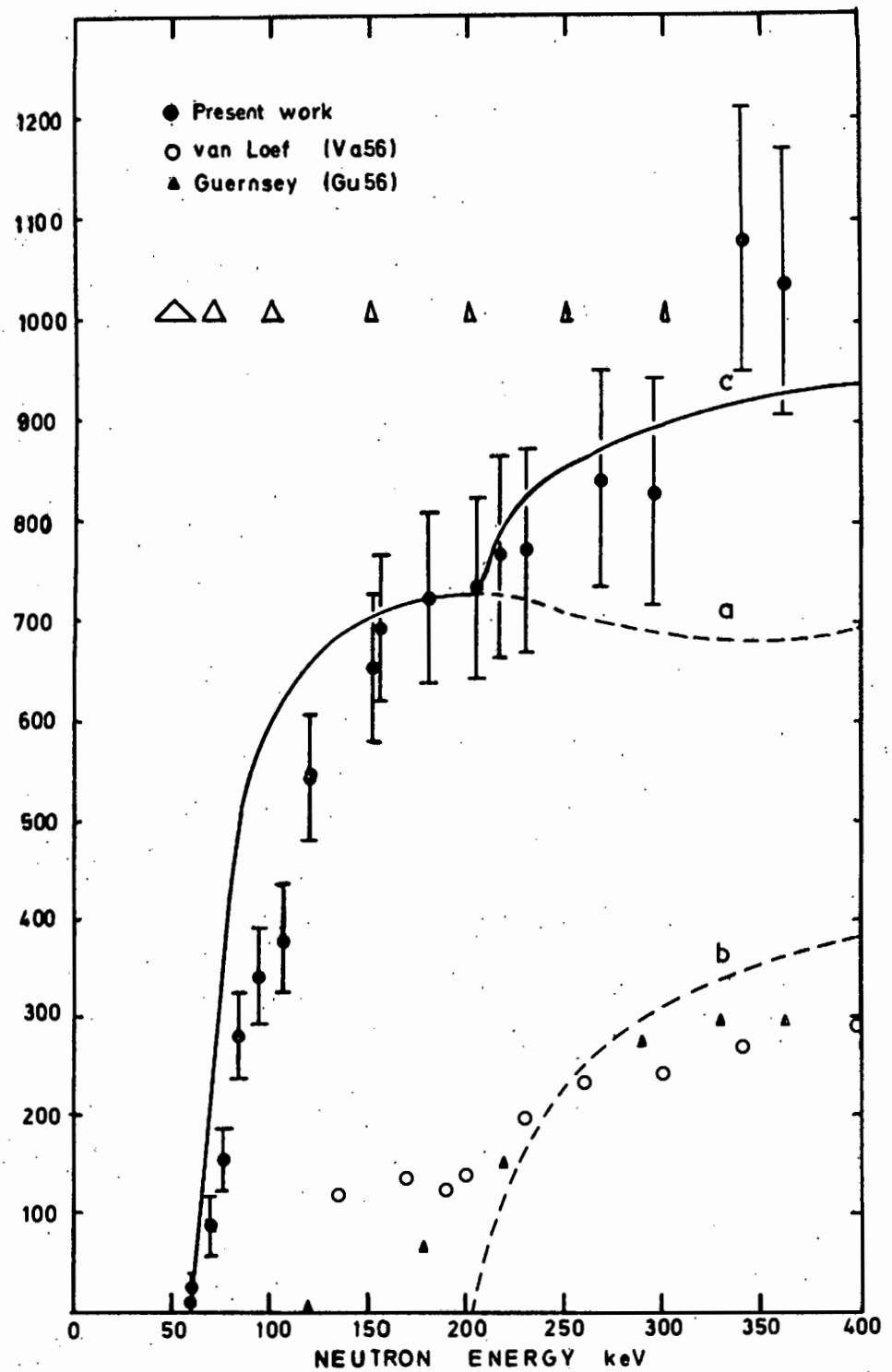

FIG 5.1 Comparison between theory and data. Curve a is HF excitation function x 0.9 for 59 keV level. Curve b is HF excitation function for 203 kev level. Curve C is obtained by adding 0.66 x b to a.

often been questioned (e.g. Mo61,63). Discrepancies between HF theory and experiment are greatest near threshold (Da63b) i.e. the region studied in this investigation. It is therefore in principle possible to check the validity of the HF prediction against the data obtained. Day (Da63b) however has pointed out that agreement or lack of agreement between theory and experiment is probably not significant unless one has the proper optical model parameters that are appropriate to the nucleus being studied. The HF curves obtained in the present work are based on transmission coefficients (Au62) dependent on global fits of optical model parameters and not on parameters specifically calculated from elastic scattering data for the ^{127}I nucleus. Furthermore a basic assumption of the HF theory is that compound nucleus formation always occurs, whereas Szteinsznaider (Sz58,Wa61) proposes that there is a significant contribution from direct interaction for inelastic scattering to the 59 keV state of ^{127}I. Because of the above, no valid conclusions can be drawn from data obtained here, about the HF theory itself. Further comparison between theory and experiment is considered to fall outside the scope of this thesis.

5.2 Conclusions

The results of these investigations may be summarized as follows:

The loaded scintillator method proved successful for the determination of the cross section for neutron inelastic scattering excitation of the 59 keV level of ^{127}I. This experiment has yielded new ^{127}I cross section data for energies near threshold. Similar measurements appear to be possible using cesium iodide crystals.

The method has been shown to be feasible, in principle, for liquid scintillators; notably those loaded with Bismuth and Praseodymium. On the other hand, much work would need to be done to develop gel scintillators for this method. The present investigations do not really confirm the feasibility of the gel technique. Application of pulse shape discrimination methods should prove most useful for loaded liquid scintillators and perhaps also for gels.

The inelastic scattering data obtained for ^{127}I do not agree with data published by Guernsey and Wattenburg (Gu56) or van Loef and Lind (Va56). The most likely reason for this discrepancy appears to be the different methods used for neutron flux determination. The present data are consistent with values calculated using the Hauser-Feshbach model of Auerbach and Moore (Au64), using the transmission coefficients given by Auerbach and Perey (Au62). These transmission

coefficients are based on optical model fits to elastic scattering data using the potential forms of either Bjorklund and Fernbach (Bj58) or Perey and Buck (Pe62).

REFERENCES

An60 Anderson et al. "Instruments and Measurements",(Proc. 5th Int. Instr. and Measure. Conf. Stockholm 1960), vol. 2. p.616, Academic Press.

Au62 Auerbach, E.H. and Perey, F.G.L. Tabulated Neutron Transmission Coefficients BNL 765(T-286) 1962.

Au64 Auerbach, E.H. and Moore, S.O. Phys. Rev. 135,B895,1964

Av66 Avigone, F.T. et al. Nuclear Physics, 80, 314, 1966.

Be65a Bemis, C.E. and Fransson, K. Physics Letters, 19, 567, 1965.

Be65b Bell, P.R. and Neiler, J.H. "Alpha-beta-gamma ray Spectroscopy", p.242, ed. Siegbahn, K. (North Holland)1965.

Be65c As Be65b, p.287

Bj58 Bjorklund, F. and Fernbach, S. Phys. Rev., 109, 1296,1958.

Bl52 Blatt, J.M. and Biedenham, L.C. Review Modern Physics, 24, 258, 1952.

Br59 Brooks, F.D. Nuclear Instruments and Methods, 4, 151,1959.

Ci66 Cindro, N. Rev. Mod. Phys. 38, 391, 1966 (Survey of Fast-Neutron Reactions)

Br64 Brooks, F.D. and Jolly, J.E. Harwell Report EANDC(UK) 42L, 1964 and Private Communication.

Cr61 Cranberg, L. et al. Nuclear Instruments and Methods, 12, 335, 1961.

Cr63a Cranberg, L. "Progress in Fast Neutron Physics", p.89, ed. Phillips, G.C. et al. University Chicago Press, 1963.

Cr63b Cranberg, L. et al. Bull.Am. Phys. Soc. 8, 82, 1963.

Da63a Day, R.B. "Progress in Fast Neutron Physics", p.118, ed. Phillips, G.C. et al. University Chicago Press, 1963.

Da63b Day, R.B. "Progress in Fast Neutron Physics", p.139, ed.Phillips, G.C. et al. University Chicago Press, 1963.

Fe54 Feshbach, H, Parker, C.E. and Weisskopft, V.F., Phys. Rev. 96, 448, 1954.

Fi61 Firk, F.W.K., Gunther, R.J. and Slaughter, G.C., Nuclear Instruments and Methods, 13, 313, 1961.

Ge65 Geiger, J.S. et al., Nuclear Physics, 68, 352, 1965.

Gi59 Gibbons, J.H. and Newson, H.W. "Fast Neutron Physics", Pt. I, ed. Marion, J.B. and Fauter, J.L., Interscience pub., 1959.

Go66 Goldberg, M.D., Neutron Cross Sections, BNL 325, 2nd edition, Sup. No.2, 1966.

Gu56 Guernsey, J.B. and Wattenburg, A., Phys. Rev. 101, 1516, 1956.

Ha47 Hanson, A.O. and McKibben, J.L., Phys. Rev. 72, 673, 1947.

Ha52 Hauser, W. and Feshbach, H., Phys. Rev. 87, 366, 1952.

He60 Helf, S., Anal. Chem., 32, 238, 1960.

Hu58 Hughes, D.J., Neutron Cross Section, BNL 325, 1958.

Jh64 Jha, A. and Leonard, R., Phys. Rev. 136, B1585, 1964.

Kl59 Kloepper, R.M., Day, R.B. and Lind, D.A., Phys.Rev.114, 240,1959.

Kn56 Knight, J.D. et al., Phys. Rev. 102, 1592, 1956.

Ma52 Margolis, B., Phys. Rev. 88, 327, 1952.

Mo61 Moldauer, P.A., Phys. Rev. 123, 968, 1961.

Mo63 Moldauer, P.A., Phys. Rev. 129, 754, 1963.

Mo61 Moore, J.G. and Orton, K.F., Selected Topics in Radiation Dosimetry 227 IAEA (1961).

Ot59 Ott, D.G. et al., Nucleonics, 17, 9, 109, 1959.

Pe62 Perey, F. and Buck, B., Nuclear Phys. 32, 353, 1962.

Sa56 Satchler, G.R., Phys. Rev. 104, 1198, 1956; errata Phys. Rev. 111, 1747, 1956.

Se54 Segel, A.et al., Review Sci. Instr. 25, 140, 1954.

Si65 Sliv, L.A. and Band, I.M., "Alpha-beta-gamma ray Spectroscopy", vol. II, p.1639, ed. Siegbahn, K. (North Holland) 1965.

Sw54 Swank and Buck, Review Sci. Instr. 26, 15, 1954.

Sz58 Szteinznaider, D. et al., J. Phys. Radium, 19, 54, 1958.

Va56 van Loef, J.J. and Lind, D.A., Phys. Rev. 101, 103, 1956.

Wa61 Way, K., US.AEC-NAS-NRC-Nuclear Data Sheets, 1961.

APPENDIX A

Correction, ϕ, for self screening and multiple scattering.

In order to take approximate account of these effects we rewrite equations 3.1, for the number N_1, of (n,α) events per second in the lithium glass as follows:-

$$N_1 = \alpha_1 N_o (1-T_1) \frac{a_1}{A_1} \{1+c_1+c_1^2+c_1^3+ \ldots\} \qquad (A.1)$$

where $a_1 = n_1 \sigma_\alpha$

$A_1 = \Sigma n \sigma_t$, i.e. the sum of the product (atoms/cm^2) $\times$ total cross section, for all nuclides in the glass scintillator.

T_1 is the transmission (without interaction) of incident neutrons by the glass. (T_1 = exp. ($-A_1$)) and

$$c_1 = (1 - \frac{a_1}{A_1}) (1-T_1') \ldots \qquad (A.2)$$

T_1' denotes the average probability of escape (without further interaction) for a neutron scattered within the glass scintillator.

In equation A.1 the first term corresponds to (n,α) events initiated directly by the incident neutron. The second term corresponds to (n,α) events caused by neutrons which have previously suffered one scattering, the third term corresponds to two previous scatterings, and so on. Implicit in equation A.1 are two assumptions, namely:

(i) The macroscopic total cross section, A_1, may be considered to consist of a (n,α) component, a_1, and an elastic scattering component, $(A_1 - a_1)$.

(ii) The values of a_1, A_1 and T_1' are effectively the same in all the significant terms of equation A.1. This implies that the energy loss (in the laboratory system) in elastic scattering is insignificant insofar as it determines these values.

Neither of these assumptions will be rigorously valid for the lithium-glass used in the present experiment. However inspection suggests that the resulting error in σ_n, will be less than about 10%.

Noting that c_1 will always be less than unity we observe that the series in equation A.1 converges to the value, $\left[1-c_1\right]^{-1}$. Thus the equation reduces to equation 3.1 as follows:-

$$N_1 = \frac{\alpha_1 N_o (1-T_1) a_1}{A(1 - c_1)} = \alpha_1 N_o \phi_1 n_1 \sigma_\alpha$$

where $\phi_1 = \dfrac{(1-T_1)}{A_1(1-c_1)}$ (A.3)

Clearly ϕ_1 tends to unity as the scintillator approaches the "thin" limit (i.e. A_1 small), since $(1-T_1)$ will then tend to the value A_1 while c_1 will tend to zero since the escape probability T_1' will tend to unity.

In the case of the sodium iodide crystal an expression analogous to equation A.3 can be derived for the correction

factor ϕ_2:-

$$\phi_2 = \frac{(1-T_2)}{A_2(1-c_2)} \qquad (A.4)$$

where T_2 , A_2 and c_2 are analogous to T_1, A_1 and c_1 respectively, and $a_2 = n_2\sigma_{n'}$.

It will readily be seen that ϕ_1 and ϕ_2 and hence the total correction factor ϕ (equation 3.5), can be calculated from cross section data for the nuclides contained in the two scintillators. The escape probabilities T_1' and T_2' respectively can be calculated from the neutron transmissions T1 and T_2 respectively using the relationship (Figure A-1) calculated by Brooks and Jolly (Br64). The transmissions T_1 and T_2, can be calculated directly from cross section data (Hu58) as also can the other terms in equations A.2 and A.3.

Calculation of ϕ_1

In calculating ϕ_1 we have calculated component factors ϕ_1' , the self-screening factor, and ϕ_1'' the multiple scattering factor, defined as follows:-

$$\phi_1' = \frac{(1-T_1)}{A_1} \qquad (A.5)$$

$$\phi_1'' = \left[1 - c_1\right] \qquad (A.6)$$

factor ϕ_2:-

$$\phi_2 = \frac{(1-T_2)}{A_2(1-c_2)} \qquad (A.4)$$

where T_2 , A_2 and c_2 are analogous to T_1, A_1 and c_1 respectively, and $a_2 = n_2\sigma_{n'}$.

It will readily be seen that ϕ_1 and ϕ_2 and hence the total correction factor ϕ (equation 3.5), can be calculated from cross section data for the nuclides contained in the two scintillators. The escape probabilities T_1' and T_2' respectively can be calculated from the neutron transmissions T_1 and T_2 respectively using the relationship (Figure A-1) calculated by Brooks and Jolly (Br64). The transmissions T_1 and T_2, can be calculated directly from cross section data (Hu58) as also can the other terms in equations A.2 and A.3.

Calculation of ϕ_1

In calculating ϕ_1 we have calculated component factors ϕ_1' , the self-screening factor, and ϕ_1'' the multiple scattering factor, defined as follows:-

$$\phi' = \frac{(1-T_1)}{A_1} \qquad (A.5)$$

$$\phi'' = \left[1 - c_1\right] \qquad (A.6)$$

Thus $\phi_1 = \phi_1'/\phi_1''$ (A.7)

Data supplied by the makers of the lithium glass (Nuclear Enterprises (G.B.) Ltd) and data given by Firk et al. (Fi61) have been used to estimate n-values for the different components of the glass. These values are shown in Table A.I.

The n-values given in Table A.I have been combined with appropriate total cross-section data $\sigma_t(E)$, (Hu58) and summed to determine A_1 as function of neutron energy, E. The components and the final result of this calculation are shown in Figure A.2. The transmission T_1 and ϕ_1' were then calculated as a function of energy from A_1. The self-screening correction $\phi_1'(E)$ is shown in both figures A.2 and A.3.

Using the relation (Br64) between T_1' and T_1 (Figure A.1) T_1' was calculated as function of T_1. Then, using published values for $\sigma_{n\alpha}$ (Hu58) to calculate a_1, and hence c_1 (eqn.A.2), ϕ_1'' (eqn. A.6) and finally ϕ_1 were calculated as a function of energy. The results of the final steps of the calculation are all shown in Figure A.3, i.e. $\phi_1'(E)$, $\phi_1''(E)$ and $\phi_1(E)$.

Calculation of ϕ_2

The calculation of the correction factor, ϕ_2, for the sodium iodide crystal should strictly speaking follow the same lines as the calculation of ϕ_1 for the lithium-glass. However in the case of the crystal the calculation was greatly simplified by

the fact that the crystal satisfied (approximately) the "thin" condition over the 60 to 400 keV neutron energy range. The n-value for ^{127}I (and hence also for ^{23}Na) in the crystal was estimated to be 2.36×10^{-3} atoms/barn. These data led to the following values: $\phi_2' = 1.00 \pm 0.01$, $\phi_2'' = 0.96 \pm 0.01$ and hence $\phi_2 = 1.04 \pm 0.01$ over the whole energy range 60 to 400 keV.

Finally therefore equation 3.5 was amended to $\phi(E) = 0.96 \times \phi_1(E)$ and the correction factor $\phi(E)$ was calculated from the values of $\phi_1(E)$ shown in figure A.3.

Table A I

NE 905 Li glass n values

Nuclide	% Wt	$n = \frac{N\rho x}{A}$ barns/atom 10^{-2}
^{6}Li	7.3	2.31
^{27}Al	4.2	2.96
^{140}Ce	3.0	0.0407
^{28}Si	33.4	2.27
^{16}O	52.1	6.19

Size 1.5" diam. $\times \frac{1}{2}$", Density $\rho = 2.48$ gm/cm^3.

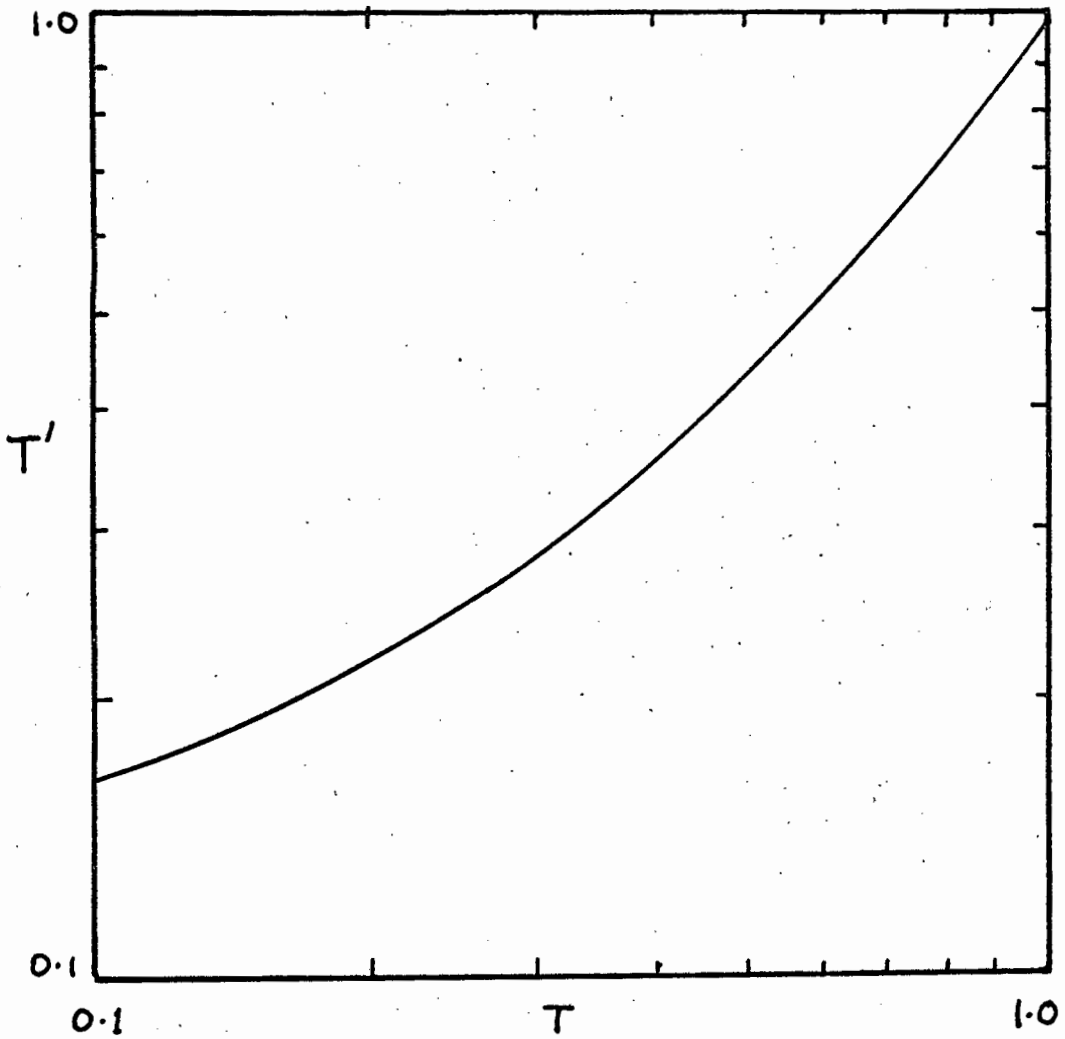

FIG A 1 Escape probability T' as a function of neutron transmission T (Br 64) for "infinite slab" geometry.

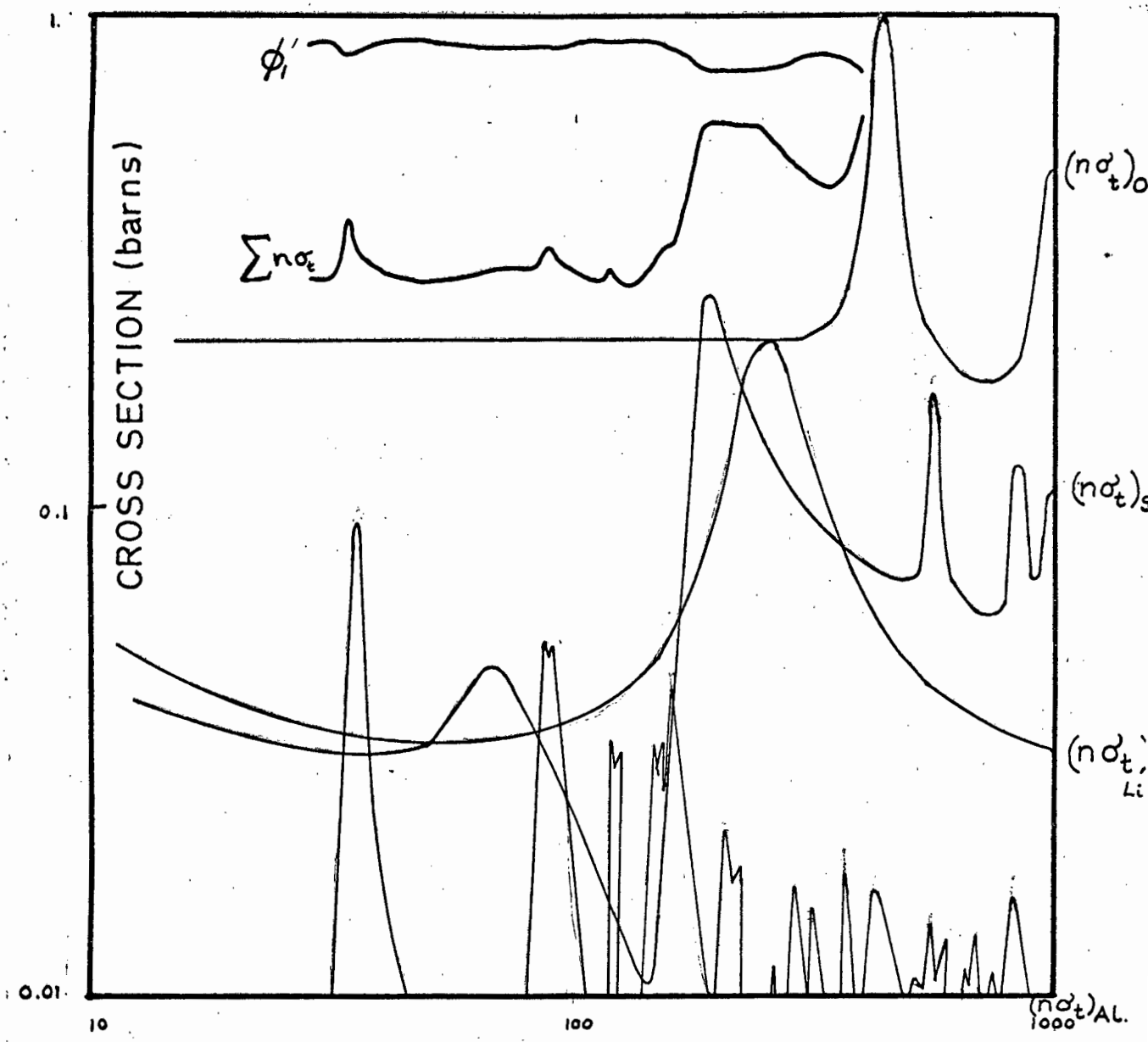

FIG A 2 Determination of A_1 from $n\sigma_t$ values of components of lithium glass detector.

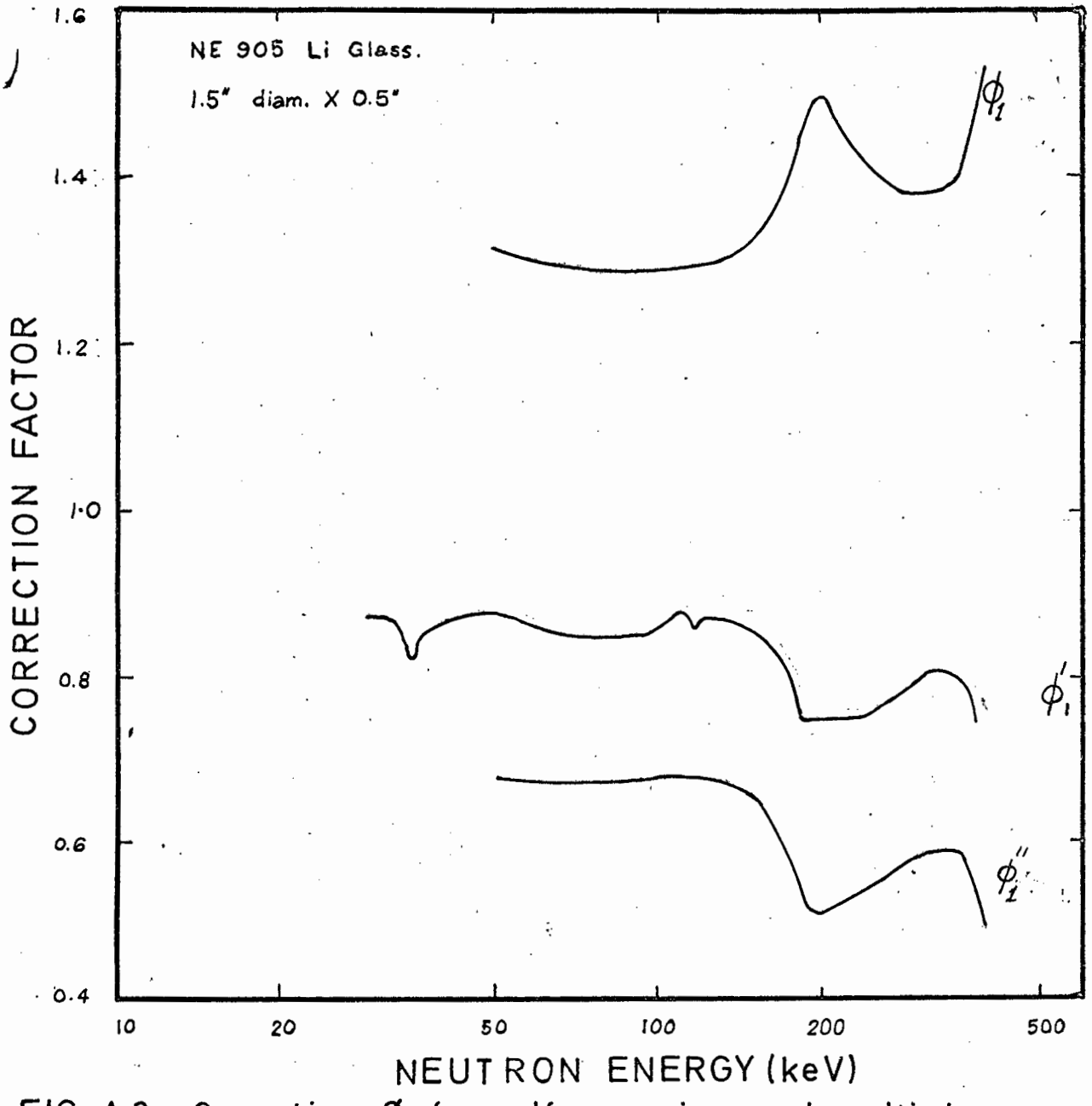

FIG A 3 Correction, Ø, for self screening and multiple scattering

APPENDIX B

PROGRAM I

MAC LISTING OF PROGRAM TO CALCULATE

HAUSER-FESHBACH EXCITATION FUNCTON.

The program is written in Manchester Auto Code for the ICT 1301 computer of the University of Cape Town.

SYMBOLS	=	+	→	/	-	/	>	.	,	≥	(	)	,	'	ϕ	π
MAC LISTING	&	∔	@	£	-	/	½	.	∉	%	(	)	£	+	ϕ	T

```
                CHAPTER1
P03 1 01        J=19
P03 1 02        J=17
P03 1 03        E=2
P03 1 04        1.0)NEWLINE3
P03 1 05        PRINT+          PARAMETERS USED TO GENERATE T VALUES+
P03 1 06        NEWLINE2
P03 1 07        L&O(1)4
P03 1 08        SPACE10
P03 1 09        J&O(1)3
P03 1 10        K&4|+J
P03 1 11        PRINT(AK)505
P03 1 12        REPEAT
P03 1 13        NEWLINE
P03 1 14        REPEAT
P03             NEWLINE
P03             PRINT+          ENERGIES SPINS AND PARITIES OF TARGET
                                    NUCLEUS LEVELS
P03 1 16        NEWLINE
P03 1 17        L&O(1)P
P03 1 18        Q&3|
P03 1 19        SPACE10
P03 1 20        PRINT(BQ)1002
P03 1 21        Q&Q+1
P03 1 22        PRINT(BQ)1001
P03 1 23        Q&Q+1
P03 1 24        PRINT(BQ)200
P03 1 25        NEWLINE
P03 1 26        REPEAT
P03 1 27        NEWLINE2
P03 1 28        PRINT+          ENERGY RANGE+
P03 1 29        PRINT(E0)1002
P03 1 30        PRINT+TO+
P03 1 31        PRINT(E2)602
P03 1 32        PRINT+KEV IN+
P03 1 33        PRINT(E1)602
P03 1 34        PRINT+KEV STEPS+
P03 1 35        NEWLINE3
P03 1 36        PRINT+          ENERGY KEV      CROSS SECTION MILLIBARNS+
P03 1 37        ACROSS10/2
P03 1 38        CLOSE
                CHAPTER2
P03 2 01        VARIABLES1
P03 2 02        1.0)E&E0
P03 2 03        11)U&0
P03 2 04        R&O(1)4
P03 2 05        S&4R
P03 2 06        DOWN10/5
P03 2 07        Q&C
P03 2 08        ACROSS10/3
```

```
P03 2 09  12)U&U+DX
P03 2 10  REPEAT
P03 2 11  13)F&1+2B1
P03 2 12  F&EF
P03 2 13  F&325500/F
P03 2 14  Y&UF
P03 2 15  NEWLINE
P03 2 16  SPACE10
P03 2 17  PRINT(E)7Ø1
P03 2 18  SPACE13
P03 2 19  PRINT(Y)6Ø2
P03 2 20  E&E+E1
P03 2 21  JUMP11ØE2%E
P03 2 22  ACROSS10/0
P03 2 23  CLOSE
          CHAPTER3
P03 3 01  VARIABLES1
P03 3 02  10)V&0
P03 3 03  N+&0.5R+0.5001
P03 3 04  L&ØINTPT(W+)
P03 3 05  F+&ØPARITY(L)
P03 3 06  F+&F+B2
P03 3 07  V+&R*L+0.5
P03 3 08  A&V+*B1
P03 3 09  A&ØMOD(A)
P03 3 10  B&V+*B1
P03 3 11  13)W&0
P03 3 12  Q&1
P03 3 121 T&3
P03 3 13  E+&E*B3
P03 3 14  JUMP11ØE+½0.0
P03 3 141 ACROSS13/2
P03 3 15  11)DOWN10/4
P03 3 16  G&W
P03 3 17  Q&0(1)P
P03 3 18  JUMP12ØQ&1
P03 3 19  T&3Q
P03 3 20  E+&E*BT
P03 3 21  JUMP12Ø0.0%E+
P03 3 22  DOWN10/4
P03 3 23  12)REPEAT
P03 3 24  Z&2A+1
P03 3 25  V&V+ZG/W
P03 3 26  A&A+1
P03 3 27  JUMP13ØB%A
P03 3 28  X&V
P03 3 29  ACROSS12/2
P03 3 30  CLOSE
```

```
                CHAPTER4
P03 4 01        VARIABLES1
P03 4 02        10)X+&A-B(T+1)
P03 4 03        X+&ØMOD(X+)
P03 4 04        X+&X+-0.4999
P03 4 05        L&ØINTPT(X+)
P03 4 06        JUMP11Ø4%L
P03 4 07        UP
P03 4 08        11)Y+&1.5001↑A↑B(T+1)
P03 4 09        M&ØINTPT(Y+)
P03 4 10        JUMP12Ø4%M
P03 4 11        M&4
P03 4 12        12)N&L(1)M
P03 4 13        A+&0.5N+0.5001
P03 4 14        3&ØINTPT(A+)
P03 4 15        G+&ØPARITY(S)
P03 4 16        G+&G+F+B(T+2)
P03 4 17        JUMP13Ø0.0½G+
P03 4 18        3&4N
P03 4 19        DOWN11/5
P03 4 20        N&N+C
P03 4 21        13)REPEAT
P03 4 22        UP
P03 4 23        CLOSE
                CHAPTER5
P03 5 01        VARIABLES1
P03 5 02        10)C&E+A(S+2)
P03 5 03        JUMP12
P03 5 04        11)C&E++A(S+2)
                12)JUMP13Ø0.1½C
                Q&ØLOG(C)
P03 5 06        Q&A(S+3)+CA(S+1)
P03 5 07        Q&ØEXP(C)
P03 5 08        Q&C=AS
P03 5 09        JUMP13Ø0.0½C
P03 5 10        UP
P03 5 11        13)C&0.0
P03 5 12        UP
P03 5 13        CLOSE
                CHAPTERØ
P03 0 01        VARIABLES1
P03 0 02        10)NEWLINE4
P03 0 03        READ(Z+)
P03 0 04        PRINT+          HAUSER  FESHBACH  CALCULATION NUMBER+
P03 0 05        PRINT(Z+)8Ø2
P03 0 06        NEWLINE
```

```
P03 0 07   I&0(1)19
P03 0 08   READ(A I)
P03 0 09   REPEAT
P03 0 10   READ(P)
P03 0 11   Q&3P+2
P03 0 12   I&0(1)Q
P03 0 13   READ(B I)
P03 0 14   REPEAT
P03 0 15   12J I&0(1)2
P03 0 16   READ(E I)
P03 0 17   REPEAT
P03 0 18   ACROSS10/1
P03 0 19   CLOSE
```

APPENDIX C

PROGRAM II

MAC LISTING OF PROGRAM TO CALCULATE ANALYTIC FUNCTION FITTED TO TRANSMISSION COEFFICIENTS OF BJORKLUND AND FERNBACH, AND PEREY AND BUCK.

```
P0300 01   CHAPTER0
P0300 02   A@19
P0300 03   NEWLINE2
P0300 04   PRINT+              PARAMETERS USED TO GENERATE
P0300 05   NEWLINE2                                  T VALUES
P0300 06   I&0(1)19
P0300 07   READ(A1)
P0300 08   REPEAT
P0300 09   I&0(1)4
P0300 10   SPACE10
P0300 11   J&0(1)3
P0300 12   K&4I+J
P0300 13   PRINT(AK)505
P0300 14   REPEAT
P0300 15   NEWLINE2
P0300 16   REPEAT
P0300 17   P&20
P0300 18   R&20
P0300 19   T&800
P0300 20   PRINT+                ENERGY RANGE+
P0300 21   PRINT(P)1002
P0300 22   PRINT+TO+
P0300 23   PRINT(T)602
P0300 24   PRINT+ KEV       IN+
P0300 25   PRINT(R)602
P0300 26   PRINT+KEV STEPS+
P0300 27   NEWLINE3
P0300 28   PRINT+                                    TRANSMISSION
P0300 29   NEWLINE3                                  COEFFICIENTS
P0300 30   PRINT+          ENERGY KEV+
P0300 31   I&0(1)4
P0300 32   PRINT+                 T+
P0300 33   PRINT(I)100
P0300 34   SPACE
P0300 35   REPEAT
P0300 36   NEWLINE
P0300 37   Q&P(R)T
P0300 38   SPACE2
P0300 39   PRINT(Q)1002
P0300 40   N&0(1)4
P0300 41   S&4N
P0300 42   C&Q+A(S+2)
P0300 43   C&@LOG(C)
P0300 44   C&A(S+3)+CA(S+1)
P0300 45   C&@EXP(C)
P0300 46   C&C-AS
P0300 47   SPACE6
P0300 48   PRINT(C)205
P0300 49   REPEAT
P0300 50   NEWLINE
P0300 51   REPEAT
P0300 52   HOOT
P0300 53   END
P0300 54   CLOSE
```